Comparative Analysis of Serrated Trailing Edge Designs on Idealized Aircraft Engine Fan Blades for Noise Reduction

Derek H. Geiger

Thesis submitted to the Faculty of the Virginia Polytechnic Institute and State University in partial fulfillment of the requirements for the degree of

Masters of Science

in

Aerospace Engineering

William J. Devenport, Chair

Wing Ng

Roger L. Simpson

December 2004
Blacksburg, Virginia

Keywords: Aircraft Engine, Fan, Noise, Tip Leakage Vortex, Serrated Trailing Edge, Blade-Wake Interaction, Turbulence Interaction, Hot-Wire

Comparative Analysis of Serrated Trailing Edge Designs on Idealized Aircraft Engine Fan Blades for Noise Reduction

Derek Geiger

(ABSTRACT)

The effects of serrated trailing edge designs, designed for noise reduction, on the flow-field downstream of an idealized aircraft engine fan blade row were investigated in detail. The measurements were performed in the Virginia Tech low speed linear cascade tunnel on one set of baseline GE-Rotor-B blades and four sets of GE-Rotor-B blades with serrated trailing edges. The four serrated blade sets consisted of two different serration sizes (1.27 cm and 2.54 cm) and for each different serration size a second set of blades with added trailing edge camber. The cascade row consisted of 8 GE-Rotor-B blades and 7-passages with adjustable tip gap settings. It had an inlet angle of 65.1º, stagger angle of 56.9º and a turning angle of 11.8º. The tunnel was operated with a tip gap setting of 1.65% chord, with a Reynolds number based on the chord of 390,000.

Blade loading measurements performed on each set of blades showed that it was slightly dependent on the serration shape. As the serration size was increased the blade loading decreased, but adding droop increased the blade loading.

The Pitot-static cross-sections showed that flow-fields near the upper and lower endwalls cascade tunnel were similar with the baseline or the serrated blade downstream of the blade row. In the wake region, the individual trailing edge serrations tips and valleys could be seen. As the wake convected downstream, the individual tips and valleys became less visible and the wake was more uniform in profile. The tip leakage vortex was only minimally affected by the trailing edge serrations. This conclusion was further reinforced by the three-component hot-wire cross-sectional measurements that were performed from the lower endwall to the mid-span of the blade. These showed that the mean streamwise velocity, turbulence kinetic energy and turbulence kinetic energy production in the tip leakage region were nearly the same for all four serrated blades as

well as the baseline. The vorticity in this region was a more dependent on the serration shape and as a result increased with serration size compared to the baseline.

Mid-span measurements performed with the three-component hot-wire showed the spreading rate of the wake and the decay rate of the wake centerline velocity deficit increased with serration size compared to the baseline case. Drooping of the trailing edge only minimally improved the spreading and decay rates. This improvement in these rates was predicted to reduce the tonal noise at the leading edge of the downstream stator vane because the periodic fluctuation associated with the sweeping of the rotor blade wakes across it, was due to the pitchwise variation in the mean streamwise velocity. The wakes were further compared to the mean velocity and turbulence profiles of plane wakes, which the baseline and the smallest serration size agreed the best. As the serration size was increased and drooping was added, the wakes became less like plane wakes. Spectral plots at the wake centerline in all three velocity directions showed some evidence of coherent motion in the wake as a result of vortex shedding.

ACKNOWLEDGEMENTS

First and furthermost I would like to thank my loving parents, Arno and Lily Geiger, who have encouraged me from the beginning to pursue my dreams and who have supported me every step along the way. Without them I would never have been able to achieve what I have, and I hope to make them proud of their son. Also, I would like to thank my brother Andrew Geiger, who as an older brother was someone I always looked up to and who I learned many things from growing up.

Next, I would like to thank my advisor and mentor, Dr. William Devenport, who has helped me throughout my research. Without his help, his guidance and his understanding it would have never been possible to put together this thesis. I have learned many new things being in the presence of such brilliant and diligent man.

Also, I would like to thank my committee members Dr. Wing Ng and Dr. Roger Simpson for their insight and suggestions which helped improve my understanding.

I would like to thank NASA-Glenn, in particular Brian Fite and Edmane Envia, who have made this research possible through the support of grant NCC3-1026.

A great many thanks goes out to those in the Aerospace shop, Bruce Stanger, James Lambert, and Steve Edwards, who have helped to answer my many design questions, and who have built the important components necessary to complete my research. Also, I would like to thank Gregg Dudding at Techsburg for putting in a great effort into manufacturing of the blades.

I would also like to thank my colleagues and friends in the lab, Aurelien Borgoltz, Elizabeth Craig, Nanyaporn Intaratep, Dustin Grissom, JV Larssen, Ruolong Ma, Patrick Mish, Chittiappa Muthanna, Ben Smith, Nick Spitz and Josh Staubs, who have not only helped me a great deal with my research, but have made the long arduous journey a lot more enjoyable.

A special thanks goes to my loving lady, Atsuko Yokobori, who has understood the demands on my time and the stress of my research. Throughout the entire time she has given me encouragement and has stood by my side through both the good times and bad times.

TABLE OF CONTENTS

NOMENCLATURE

Roman

b_s	Serration spanwise height
c	Total chord length of blade
c_a	Axial chord length of blade
C_p	Coefficient of static pressure
$C_{p,b}$	Coefficient of back pressure
$C_{p,s}$	Coefficient of pressure on the surface of the blades.
$C_{p,o}$	Coefficient of total pressure
d_s	Serration chord-wise depth or length
f	Spectral frequency
$G_{uu,}\ G_{vv},\ G_{ww}$	Spectral functions in the three velocity directions
k	Turbulence kinetic energy
$k_1,\ k_2$	Wygnanski mean velocity curve fit constants
l	Wake width
L_w	Wake half-width
$L_{w,p}$	Wake half-width measured in the pitchwise direction
p	Instantaneous pressure, fluctuating pressure
P	Local static pressure in the tunnel
P_b	Back pressure in the tunnel
P_k	Turbulence kinetic energy production
P_∞	Freestream pressure
P_o	Total local pressure in the tunnel
$P_{o,\infty}$	Total freestream pressure
$\overline{u'^2}$, $\overline{v'^2}$, $\overline{w'^2}$	Time averaged normal stress components
$\overline{u'v'}$, $\overline{u'w'}$, $\overline{v'w'}$	Time averaged shear stress components
$U,\ V,\ W$	Time averaged mean velocity components in the wake direction

U_e	Edge velocity of the wake
U_w	Centerline velocity deficit
U_∞	Freestream velocity
x, y, z	Cascade row aligned coordinate system; trailing edge
x_1, *y, z*	Cascade row aligned coordinate system; leading edge
X, Y, Z	Blade wake aligned coordinate system

Greek

Γ	Circulation
Ω_x	Mean streamwise vorticity
θ	Momentum thickness
θ_x, θ_y, θ_z	Euler angles in the three cascade coordinate system directions
Ψ_1, Ψ_2	Wygnanski momentum thickness curve fit constants

LIST OF TABLES

LIST OF FIGURES

CHAPTER ONE

1. Introduction

1.1 Overview of Aircraft Engine Noise Emissions

Every year the international and domestic restrictions on noise emissions from aircraft engines become stricter. In the near future (2007-2010), the cumulative noise levels will have to be reduced by 15 dB over the current International Civil Aviation Organization (ICAO) Stage 3 noise levels., while in the long term cumulative noise reductions of 75 dB by 2025 are predicted to be required for the United States (ATE-Vision) over the current ICAO Stage 3 levels (Krammer *et al.* (2003)). Also, more airports are implementing landing restriction mainly due to the pressure from local governments because of noise generated by the increased air traffic affecting the population living in the vicinity of airports. Over the last 20 years air traffic has more than doubled, and ICAO forecasts passenger and cargo traffic will grow at a steady rate of 4.5% and 6.0% annually, respectively, over the period of 1999 to 2010. The stricter noise emissions restrictions are forcing manufacturers to find new ways of reducing the sources of noise in their engines.

To meet these goals, the individual components of the engine, for example, fan blades, compressors, turbines and exhaust nozzles, need to be investigated in detail to determine methods of how to improve them acoustically as well as aerodynamically. Acoustically improving engine components is a very complex process that can not be achieved without analyzing the fluid dynamic problem. To acoustically improve these components, a full experimental study into the fundamental fluid dynamics needs to be performed.

Long term and short term aircraft engine technology programs have been started in the United States and Europe to develop new noise reduction techniques. In the United States, under the Advanced Subsonic Technology Program (AST), Pratt & Whitney designed and built the scale model fan technology demonstrator Advanced Ducted Propulsor (ADP) to demonstrate the feasibility of obtaining the AST noise reduction goal of 6 EPNdB (Effective Perceived Noise dB), (Envia (2001)). In Europe, projects with similar goals have been started, for example, the Reduction of Engine Source Noise through Understanding and Novel Design (RESOUND) which also has a goal of an overall aircraft noise reduction of 6 dB (Juve (1999)). Other European project are currently running with goals of 6 dB reduction in overall engine noise by 2008 as well as long term projects which are looking into reducing the noise levels by 15 dB over current turbofan engines.

1.2 Fan Noise and Noise Reduction Techniques

Of all of the components in an aircraft engine, the fan of modern commercial aircraft engines, especially those of high bypass ratio turbofans, is one of the major sources of noise. With engine bypass ratios (BPR) expected to increase in the future, going above BRP of 10:1 found for example in the prototype PW8000 engine and the 14:1 BPR found in the ADP, fan noise reduction will become even more important. From previous noise studies, the fan dominated the engine total flyover noise signature during take-off and approach while utilizing acoustic liners

Work has been done on new noise reduction methods for the fan. In the AST program, for example, sweep and lean of the outlet guide vane, active noise control and fan wake management have been investigated, while short term programs have investigated more conventional methods, for example, geared turbo fans. These methods have shown promise. Sweeping and leaning the outlet guide vane have shown noise reductions of 5 dB for the inlet quadrant and 10 dB for the exhaust quadrant for all angles (Envia (2001)). In terms of perceived noise, the sweeping and leaning had a 3 EPNdB noise reduction over the entire range of tip fan speeds. The second method that was researched in detail was active noise control, which is a technique of using actuators

embedded on the surface of the engine casing or in the stator vanes to create an acoustic field that is of equal amplitude but of an opposite phase of the acoustic field to be cancelled. This method has shown some good noise reduction results with about an average of 18 dB reduction over a range of fan speeds (Envia (2001)).

In a more conventional approach, the reduction of the fan tip speed has been investigated in more detail to reduce the fan noise. This research stemmed from the investigation of larger turbo fans, with BPRs above 10:1, to increase engine efficiency while reducing fuel consumption and costs. With larger fans the efficiency of the engine is increased, but the noise levels due to the fan are also increased. Therefore, by reducing the fan tip speed, by decoupling the fan from the turbine with a gearbox, the noise levels can be decreased quite substantially. Noise levels produced by the fan are estimated to be proportional to the velocity of the fan tip speed to the 5^{th} power (Elliot (2001)).

Another approach being looked into more detail more recently is wake management of the fan blade. One approach to wake management is the injection of mass at the trailing edge of the blade to 'fill in' the wake deficit, thereby creating a uniform inflow to the downstream stator. This method is usually referred to trailing edge blowing. It has been studied recently and has shown signs of being able to reduce the noise levels. In a model engine test performed by Sutliff *et al.* (2002) this technology has shown reductions up to 12.4 dB (tone power level).

1.3 Motivation & Purpose: New Wake Management Techniques for Fan Noise Reduction

The research presented in this paper focuses on a specific aspect of the latter technology topic for fan noise reduction discussed in section 1.2 known as wake management. As mentioned above, wake management is the philosophy of altering the wakes shed by an upstream blade row to allow a more uniform flow to enter the downstream blade row. The idea of wake management stems from the problem found in aircraft engines. In aircraft engines the axial spacing between the upstream fan and the downstream stator vanes are usually no more than few axial chords due to the limitations set on engine length and weight. Since the distance between fan and stator vanes are

small, the velocity deficit in the viscous wake shed by the fan blade impinges on the downstream stator which is a prime cause of the rotor-stator interaction noise. Therefore, it is hypothesized that wake management performed on the fan blade will reduce this wake deficit prior to entering the stator row.

Prior studies of wake management techniques have been performed experimentally to determine its effectiveness. Usually, these studies of wake management were limited to trailing edge blowing. This study of wake management will look at entirely different approach by testing and analyzing the effects of serrated trailing edges on the wakes of fan blades. In order to fully understand the effectiveness of the trailing edge treatments on tonal noise downstream of a fan blade row created by the rotor-stator interaction, it is necessary to understand the fundamental fluid dynamic phenomena that are occurring and controlling these sources of noise.

1.4 Review of Wake Management Research

Experimental studies into the effect of wake management, more specifically trailing edge blowing and serrated trailing edges, have been performed on flat plate airfoils, model aircraft engines and wind turbines. In the following sections a review of past research performed on wake management schemes will be presented.

1.4.1 Fundamental Experimental Studies of Momentumless Wakes

Some of the most fundamental research with momentumless plane wakes was performed by Cimbala and Park (1990), who studied pure wake, weak wake, momentumless wake and weak jet effects. They performed their measurements on an airfoil-shaped flat plate which had a rounded leading edge and a blunt trailing edge. The airfoil shape had an aspect ratio of 51 and a chord length of 89 mm. At the exit of the trailing edge, a slit covering 80% of the span allowed for air jet-injection. The measurements on the airfoil were performed in a 0.3 by 0.97 m cross-section test section with free-stream velocity of 4.2 m/s. Flow visualization, single hot-wire and dual-sensor hot-wire measurements were performed for all four wake types. In the near flow, the

authors observed that the pure wake and the weak wake had Kármán-type vortex structures and a definite wake structure, while the momentumless wake and jet wake had wake-like structures near the edges, but was highly disorganized in the wake center. Far downstream, they observed the pure and weak wake spread with wake scales that doubled in size. On the other hand, the weak jet showed a slow growth rate but still had wake eddy scales that doubled in size and for the momentumless wake, only small eddy fluctuations were present indicating that it all but decayed. The mean velocity measurements, showed a rapid decay of the centerline velocity deficit ($U_d \sim x^{-0.92}$), were self-similar and had a slow spreading rate ($l \sim x^{0.30}$, where l is wake width) for the momentumless wake while the pure wake was also self-similar but had a larger spreading rate ($l \sim x^{0.50}$) and much slower velocity decay ($U_d \sim x^{-0.50}$). Spectra revealed Kármán vortex shedding for the pure wake but none for the momentumless wakes. For the momentumless wakes, quasi-periodic vertical motion created by large turbulence structures near the boundaries was present. The decay rates for the axial and traverse intensities had the same decay rate which was proportional to $x^{-0.81}$ which was shown to be much faster than a plane wake ($\sim x^{-0.50}$). The shear stress term $\overline{u'v'}_{\max}$ decayed faster and was proportional to $x^{-1.84}$, equivalent to the square of the decay rate of the wake deficit. Far downstream the wake was claimed to be isotropic and similar to grid turbulence. A final observation was the production and dissipation did not balance for the momentumless wakes which differs from elementary free-shear flows.

Park and Cimbala (1991) expanded the above study to investigate momentumless wakes created by asymmetric and dual jets. The setup was identical to their study above except the airfoil had two 1.6 mm slots at the trailing edge instead of one. The flow visualization revealed a sinusoidal wake structure in the center in the near wake region, and as it progressed downstream the local wake and jet structure was still apparent but disorganized in the center. The dual jet had flapping effect in the wake caused by the upper and lower jets merging. It was hypothesized by the author that the Kármán vortex shedding interacted with the jets enhancing the flapping effects. The mean velocity profile for the asymmetric wake looked like a patched jet-like, wake-like structure. Even though it was momentumless, it maintained both structures locally in the mean velocity profile indicating that the profile was highly dependent on the initial conditions. The dual

jet had similar mean velocity profile as central jet, and a strong interaction between the jets was present, even though the flow field was highly asymmetric. Interestingly, they showed the mean velocity deficit decayed much faster for the dual jet with a decay rate of ($U_d \sim x^{-2.02}$), compared to the asymmetric jet ($U_d \sim x^{-1.24}$) and central jet. Spreading rate was also quicker for the dual jet ($l \sim x^{0.41}$) compared to asymmetric jet ($l \sim x^{0.36}$) and the central jet ($l \sim x^{0.33}$). It was observed that turbulence intensities of the dual jet were anisotropic in the early stages but became Gaussian like downstream and similar to the central jet. Reynolds stress profiles for the dual-jet are different than the single-jet due to the flapping of the two jets. For all the cases, the normalized turbulence intensity showed universality for the 2-D momentumless wakes as well as being symmetric. The decay rate of the axial turbulence intensity also showed universality, with a decay rate proportional to $x^{-0.81}$. They concluded that the mean velocity and turbulence intensities were dependent on the initial conditions even in the far field.

Experimental studies were also performed by Takami and Maekawa (1996) to investigate the turbulence structures of two-dimensional momentumless wakes. The experiment was also performed on an airfoil-like flat plate with a rounded leading edge and a blunt trailing edge. The experiment investigated the structures of a pure wake, a weak wake, a momentumless wake and a weak jet. Similar to Cimbala & Park (1990), flow visualization and hot-wire measurements were performed to determine wake structures. The conclusions of this experiment matched those in Cimbala & Park (1990), especially the similarity in the turbulent intensities, the rapid decay of downstream turbulence properties and the similarity with isotropic turbulence.

Cherepanov and Babenko (1998) performed an experimental and numerical study of the momentumless wake downstream of a wing profile. This study compared the results from the experiment with other known momentumless studies performed on airfoil shapes, namely performed by Ukhanova and Frankfurt (1984), Cimbala and Park (1990) and Zdanov and Ecelmann (1990, 1991). The author also compared his second order Reynolds stress turbulence model to the data. The experiment was performed in a wind tunnel with a test section that was 82 mm by 82 mm by 4600 mm long, on symmetric airfoil that had a smooth trailing edge with a span of 0.074 m and a chord of 0.1 m. From the experiment, the author observed non-universality in the wake region

when the results of all the momentumless studies were compared. On the other hand, the jet region showed universality. Another observation was the mean velocity deficit decayed faster than the turbulence properties. The turbulence kinetic energy decayed with a rate proportional to $x^{-1.6}$ and the dissipation with a rate of $x^{-2.45}$. The growth rates of the wake were determined to be between $x^{0.18}$ and $x^{0.20}$. The author most importantly wanted to show the non-universality in the some the wake characteristics which were thought to have existed.

1.4.2 Trailing Blowing Experiments Performed on Model Engines

There have been a few studies investigating the use of trailing edge blowing on model aircraft engines. One such study was performed Brookfield and Waitz (2001), who used trailing edge blowing to reduce the rotor-stator interaction noise by filling in the wake, hence, reducing the tonal noise, and decreasing the wake turbulence which is a source of broadband noise. The study addressed the challenge of applying trailing edge blowing on the representative next generation fan stage, taking into account the three-dimensional character of the geometry and acoustic mode structure. The study was performed on a model fan with a 16 bladed fan stage, 40 stator blades, a hub-to-tip ratio of 0.5, a 1.7 chord length separation between the blade rows, a pressure ratio of 1.2, a tip Mach number of 0.8 and an inlet Mach number of 0.45. The mass flow for the trailing edge was provided through an external plenum. Flow field measurements were performed with a probe utilizing four flush mounted Kulite pressure transducers. Duct microphone pairs were placed $1/16^{th}$ apart along the circumference of, one axial chord downstream of the blade row. Pressure measurements were performed on the surface of the stator blades. They noticed some slight performance variation between the baseline blades and the trailing edge blowing blades due to the small change in the untwist characteristics and exterior shape. Tip weighted and midspan weighted injection showed same results, which was the filling of the wake and some reduction of the turbulence intensities. All of the flow properties varied with the blade span. The wake relative Mach number, BPF, and 2xBPF harmonic amplitudes at 1.5 chords downstream of the blade row with trailing edge blowing were near or below those at 0.1 chords downstream for the baseline. The

stator unsteady loading also improved, resulting in a 10dB reduction at BFP with tip weighted injection.

Sutliff *et al*. (2002) investigated the use of trailing edge blowing to reduce the rotor-stator noise levels and to validate turbulence models, CFD tools, and acoustic models used to predict the flow field created with this system. The experiment was performed on NASA's 48 inch Active Noise Control Fan (ANCF) located in the Aero-Acoustic Propulsion Laboratory (AAPL). The ANCF is a ducted fan with a tip speed of 425 ft/sec with a blade passing frequency (BPF) of 500 Hz. They used a 16-bladed rotor and a 14-bladed stator row to investigate their trailing edge blowing concept, which resulted in 1BPF, 2BPF and two modes at 3BPF. The rotor blades equipped with blowing were specially made with internal passages to allow for mass flow to be provided via four 4 in diameter hoses from an external plenum to the trailing edge of the blades. They tested three different cases: (1) non-blowing (trailing edge fixed with inserts), (2) self-blowing where blowing is induced by pressure differences between the trailing edge of the blade and the ambient, i.e. plenum (0.6% mass through flow), (3) optimum blowing using approximately 2% measurements mass through flow. Measurements were performed on all three cases with two-component hot wires (axial and tangential) one axial chord downstream of the rotor blades at 15 to 25 radial locations. They also performed unsteady stator vane surface pressure measurements using three stator blades equipped with 30 microphones each, rotating downstream rake measurements to map the ducted modes, and farfield acoustic measurements using 28 microphones for the baseline and optimum blowing cases. The hotwire measurements showed the overall reduction of the wake deficit on the inner span for all three cases while maintaining the turning angle of the blades. Over other half of the blade (50% to the tip) self-blowing increased the wake velocity deficit while the optimum blowing case over-filled the wake which was most likely due to the fact that the blades were tip heavy in blowing. At 20% chord line of the stator blades, surface pressure fluctuation level decreased with optimum blowing, especially near the tip on both the suction and pressure sides. Duct measurements showed tonal noise reductions for majority of the tones at the inlet and exhaust. For 1BPF, measurements showed a tone noise reduction of 11.5 dB and tonal noise increase of 0.1 dB at the inlet and exhaust respectively, at 2BPF showed tone noise reductions of 7.2 dB

(inlet) and 11.4 dB (exhaust) were observed while at 3BPF the measurements showed tonal noise reductions of 11.8 dB (inlet) and 19.4 dB (exhaust). These reductions were validated with farfield measurements. Noise level reductions of 5.4 dB at 1BPF 10.6 dB at 2BPF and 12.4 dB at 3BPF were measured. Finally, all codes used to evaluate the design of the system were shown to agree with the experimental results.

A smaller study performed by Leitch *et al*. (2000) investigated the use of trailing edge blowing for stator-rotor noise reduction. The experiment was performed on four inlet guide vanes (IGV) located 0.75 chord lengths upstream of a 1/14 scale model of a turbo fan simulator. The IGVs had zero turning angle and six blowing holes at the trailing edge of the blade. The turbo fan simulator was composed of 18 fan blades and 26 outlet guide vanes. Measurements were performed at fan speeds 30,000 rpm, 50,000 rpm and 70,000 rpm in Virginia Tech's Anechoic Chamber (13.1 ft x 8.9 ft x 6.6 ft) which is anechoic above 200 Hz. Steady state static and total measurements were performed to completely map the fan face and downstream wakes from the stators using a 0.0625: diameter Pitot-static probe. Microphone measurements at 12 points along a circular arc from 0 to 110º from the fan axis were performed using Brüel and Kjäer Model 4136 condenser microphones upstream of the inlet face. The pressure measurements showed the IGV wakes were filled using less than 1% of the mass through flow. The wake filling also reduced the tonal sound pressure level as well as its first harmonic, but had little effect on the broadband noise. For the fan speed of 30,000 rpm, the greatest noise reduction was at 80º with 8.9 dB tone SPL, while 30º to 90º had a 6.8 dB tone SPL reduction. At 0º there was an increased in the tonal noise level. The overall sound pressure level was reduced, on average by 1 dB while between 50º to 90º it was 2dB. For 50,000 rpm an average of 2.6 dB blade-passing tone reduction between 0 to 110º was achieved, with a maximum reduction of 5.5 dB At 70,000 rpm, an average blade-passing tone reduction of 1.2 dB was achieved, with a maximum reduction of 2.6 dB. The SPL reduction was less than 1 dB. It is hypothesized that the noise reduction was less for the higher fan speeds because not enough mass flow was provided and the higher tip speeds also resulted in buzz-saw noise which trailing edge blowing was not effective in reducing.

Rao *et al*. (2001) used the same trailing edge system as Leitch *et al*., except he integrated into the system an active wake control system. The active control system was

designed to adjust the required amount of blowing air as a function of the fan speed, therefore, providing the optimum amount of mass flow to fill in the wake. The same apparatus, instrumentation and methods were used as were used by Leitch *et al.*, except for the added active control system. Flow was controlled to each by using MEM based microvalves. The active control system was preliminary tested to show that it feasibly can fill the wakes. The filling of the wakes provided a relatively uniform flow field. Noise reductions were noticed over the entire range of speeds. At 30,000 rpm there was an 8.2 dB BPF tone noise reduction at 20º and 6 to 3 dB reduction over the first four harmonics. At 40,000 rpm, the BPF tone noise reduction was 7.3 dB at 20º, and the SPL remained the same between 60º to 110º. Sound power level reduction at both fan speeds, with a 4.4 dB reduction at 20,000 rpm and a 2.9 dB reduction at 40,000 rpm. Multiple noise sources were presented because of the stator-rotor interaction and the rotor-exit guide vane interaction; therefore, it was not possible to truly determine the overall noise reduction in the engine.

Wo *et al*. (2002) investigated the response on the downstream blade due to trailing edge blowing, with the primary interest on the traverse gust. The experiment was performed in a low-speed, large scale 1 to 3 stage compressor rig. The axial spacing of the rig was variable from 10% to 60% of the blade chord length. The compressor rig used 60 inlet guide vanes, 58 rotor blades and 60 stator blades, all with 6 cm chord. The IGV was located 1.75 chord lengths upstream to allow the wake to dissipate and rotor-stator spacing was 30% chord. The air for the trailing edge blowing was provided externally though the internal section of the blades. Surface pressure measurements were performed with Kulite pressure transducers. Variable mass flow injections were used to accommodate the various conditions was run at, ranging from 1.3% to 3.7% of the mass through-flow. Results show the near-wake development was highly dependent on the blade loading. The velocity deficit was reduced at near-design but not at a high blade loadings. Further downstream clear reductions were seen. The traverse gust factor decreased with the wake momentum defect factor. Finally, they showed a near linear decrease of the stator unsteady force with the increase in the blowing momentum.

1.4.3. Studies of Serrated Trailing Edges

Serrated trailing edges have been proposed previously as a means to attenuate trailing edge noise. Howe (1991) developed a trailing edge noise prediction model for serrated trailing edge designs. The estimation that he developed modeled the effect of the geometry of the serrations on noise reduction. His model was based on the theory that noise is created only in the vicinity of the regions where the turbulent eddy wave number is normal to the edge. Another important approximation was the turbulence on the upper and lower surfaces did not interact at changing the turbulence characteristics at the trailing edge and did so only downstream of the edge exceeding the boundary layer thickness. Therefore, he adopted the diffraction problem where the near field turbulence are scattered by the impedance discontinuity at the edge and wrote the acoustic radiation in terms of the diffraction of the blocked pressure at the trailing edge. Using this method he showed his model predicted reductions in the radiated sound as long as the serration angle does not exceed 45º, i.e. a function of the serration geometry, and the serration sizes should be on the order of the boundary layer thickness.

It seems most of the application work of serrated trailing edges has been performed on wind turbine blades to reduce the trailing edge noise. A short summary of serrated trailing edge work performed in Europe was composed by Guidati *et al*. (2000). In summary all of the experimental and application work has shown total noise reductions up to 4-6 dB. They also show that the low frequency noise levels decreased, but the high frequency noise increased. The benefit of serrated trailing edges for reducing stator rotor interaction noise has not previously been studied.

1.5. Objectives and Approach of Comparative Study of Serrated Trailing Edges

The goal of the current research is to obtain a detailed fundamental understanding of the effects of various trailing edge serration configurations on the downstream wake of an idealized fan blade row in order determine their effectiveness as trailing edge treatments for tonal noise reductions in aircraft engines. It is predicted by controlling the downstream rotor blade wake the tonal noise can be reduced at the leading edge of the

downstream stator vane. The rationale here is that a point on the leading edge of a stationary stator vane will see a periodic fluctuation associated with the sweeping of the rotor blade wakes across it, where the periodic behavior is due to the pitchwise variation in the mean streamwise velocity. From this research, it is also hoped, to obtain benchmark data of the wakes created by the trailing serrations in order to develop and validate computational fluid dynamic (CFD) codes.

The objectives of the current research are:

1. To set up an idealized model of the flow through and downstream of an engine fan.
2. To document in detail the mean flow and turbulence structure of the idealized fan blade wakes
3. To reveal and quantify the effects of the serrated trailing edges on these wakes through mean flow and turbulence measurements
4. To reveal and quantify the tip leakage vortex downstream of the blade row for different serrated trailing edge configurations
5. To understand the fundamental mechanisms controlling the wakes of the different serrated trailing edge configurations for later theoretical modeling
6. To provide benchmark data for the development and validation of turbulence models in CFD codes.

The above objectives were achieved by using a cascade wind tunnel. By using the cascade approach, a large-scale idealized model of the fan rotor wake can be obtained in a stationary reference frame that is more easily measured.

The linear cascade used for the study simplifies the problem to large degree. Firstly, there are no downstream stator vanes allowing the model fan blades to be modified without the need to exactly match the exit turning angle of the blades and the inlet angle of the stator vanes. This allows for various serrated trailing edge configurations to be tested, which may or may not, change the turning the angle of the blades. However, not having a stator downstream of the blade row does not allow for noise measurements of the impinging rotor wake on the stator row. Secondly, the true fundamental characteristics of the wake can be revealed because the rotor blades are not rotating which introduces secondary flow inside the boundary layer on the fan blades

through the rotation-induced centrifugal and Coriolis forces. Since it is a linear cascade and there are no rotating effects due to the motion of the blade row, uncertainties in the study due to the above effects can be eliminated and the fundamental characteristics of the wake can be revealed.

By using the linear cascade approach fundamental studies similar to those performed by Cimbala & Park (1991), Takami & Maekawa (1996) and Cherepanov and Babenko (1998) on momentumless wakes, can be performed on wakes of serrated trailing edges. This also allows these wakes to be compared to those studies to understand the similarities and differences between momentumless wakes and serrated trailing edge wakes. Once the fundamental dynamics controlling these wakes are understood model engine testing can be performed to investigate the rotor-stator interaction in greater detail.

The objectives listed above will be achieved by using the following approach:

1. The use of the linear cascade, with moving end wall, to model the fan rotor wake produced by various serrated trailing edge designs.
2. The use of three-component hot-wire anemometry to perform single point measurements downstream of the blade trailing edge.
3. Measure the blade loading on the modified blades using the surface pressure ports fabricated into the blades.

1.6. Prior and Parallel Studies in the Virginia Tech Low Speed Cascade Wind Tunnel

Numerous studies have been performed in this cascade facility. It was first modified from a turbine cascade configuration in 1996 and through the use of a moving endwall, it has the ability to simulate the rotational effects of a moving rotor blade in the vicinity of a casing. Both stationary and moving endwall configurations have been used in the prior studies.

The first study performed in this facility was performed by Muthanna (1998). In this study the flow field downstream of the cascade row for tip gap settings of 0.83%, 1.65% and 3.3% chord was studied. Measurements were performed at five downstream planes using four-sensor hot-wires. These measurements revealed the structure and the

downstream development of the tip leakage vortex. The vortex region was shown to be a region of high streamwise velocity deficits and turbulence levels. It was shown that the turbulence kinetic energy in the tip leakage vortex appeared to be produced by the streamwise velocity gradients and not the cross-flow velocity gradients. Also, the wakes of the blades were measured which were shown to exhibit characteristics typical of two dimensional plane wakes. From the spectral measurements it was suggested that there may be some vortex shedding from the trailing edge of the blades in the wakes.

The vortex structure of the cascade was further studied and analyzed by Wenger (1999). Two-point turbulence measurements were made in the same flowfield as Muthanna (1998) downstream of the cascade with a tip gap setting of 1.65% chord. The tip leakage vortex was determined not to be affected by the low frequency wandering motions. The eddies in the vortex were inclined by about 30 degrees with respect to the vortex axis which is indicative of anisotropy in the tip leakage vortex.

The cascade tunnel facility was enhanced by Wang (2000) who added a moving wall system to properly simulate the relative motion between the blade tips and the endwall. Measurements were performed with three tip gap settings of 0.83%, 1.65% and 3.3% chord at the three downstream locations with respect to the leading edge line of 1.51, 2.74 and 3.75 axial chords. Both moving wall and non-moving wall measurements were performed. It was determined through this study that the turbulence and mean velocity distributions were flattened and sheared. However, comparing the turbulence kinetic energy (TKE) production of the two flows, Wang found that they both have the same distribution in the vicinity of the highest levels of TKE production. This showed that the basic governing mechanisms controlling the development of the mean flow and turbulence structures are identical.

A study by de la Riva (2001) investigated the effects of the grid turbulence on the flow structure in the blade passage for a 1.65% chord tip gap with a stationary wall. The measurements were compared to the predictions of the two-dimensional flow away from the lower endwall using Rapid Distortion Theory (RDT). The goal of the study was to investigate the capabilities of RDT in predicting the turbulence convection through a highly staggered cascade propulsor configuration. RDT was successful in predicting the

trend of the turbulence evolution in the potential core but did not do well in modeling the turbulence normal to the surface of the blade.

Further studies were performed by Muthanna (2002), who investigated the effects on the behavior of flowfield of grid generated free stream turbulence. Measurements were performed with a stationary wall with at 1.65% chord tip gap setting at two locations upstream of the blade row and at six locations downstream of leading edge line. The free-stream turbulence showed significant effects on the flowfield. There was a 4% increase in the blade loading, a 20% reduction in the vorticity levels, in the tip leakage vortex and a 30% enlargement of the tip leakage vortex.

A more recent study was performed by Ma (2003) who investigated the unsteady behavior of a tip leakage flow downstream of the cascade for a stator-rotor interaction study (figure 1-1). The unsteady behavior was investigated by using triangular shaped generators attached to the moving wall system upstream of the cascade blade row to create a vortical inflow. The results showed that the generators were capable of altering the tip leakage vortex shape, structure and strength even though they produced a vortex that was approximately 80 times weaker than the tip leakage vortex. Since the effects were confined to the tip leakage region of the cascade, the blade loading was not significantly affected by these disturbances.

1.7. Thesis Layout and Structure

This thesis describes in detail the experiments performed on the wake created by the various serrated trailing edge designs and investigates the fundamental controlling parameters of the wake and its development downstream. The thesis is organized into the following chapters:

Chapter 2 gives a detailed description of the apparatus and techniques used to perform this study. These include the Virginia Tech low speed cascade tunnel, the moving wall system, the hot-wire anemometry measurement apparatus, the Pitot-static probes and the baseline blade configuration.

Chapter 3 investigates the measurements and analysis performed on the baseline configuration. Studied in detail were the mean velocity and turbulence structures of the

wake downstream of the blade row, the two- and three-dimensionality of the wake, and the tip leakage vortex. Also, included are comparisons with experimental results from other established plane wake measurements.

Chapter 4 introduces the various serrated trailing edge blade designs. Also, described are the tunnel set-up and the downstream pressure measurements.

Chapter 5 introduces the various serrated trailing edge blade configurations and presents the measurements performed to reveal the mean velocity and turbulence structures of their wakes. Analysis performed on the data is also given, which includes the two- and three-dimensionality of the wake and the tip leakage vortex. The data is compared to the baseline configuration to determine the variation of there types of trailing edge designs on the wake structures.

Chapter 6 is the last chapter and summarizes the results as well as conclusions of the previous chapters.

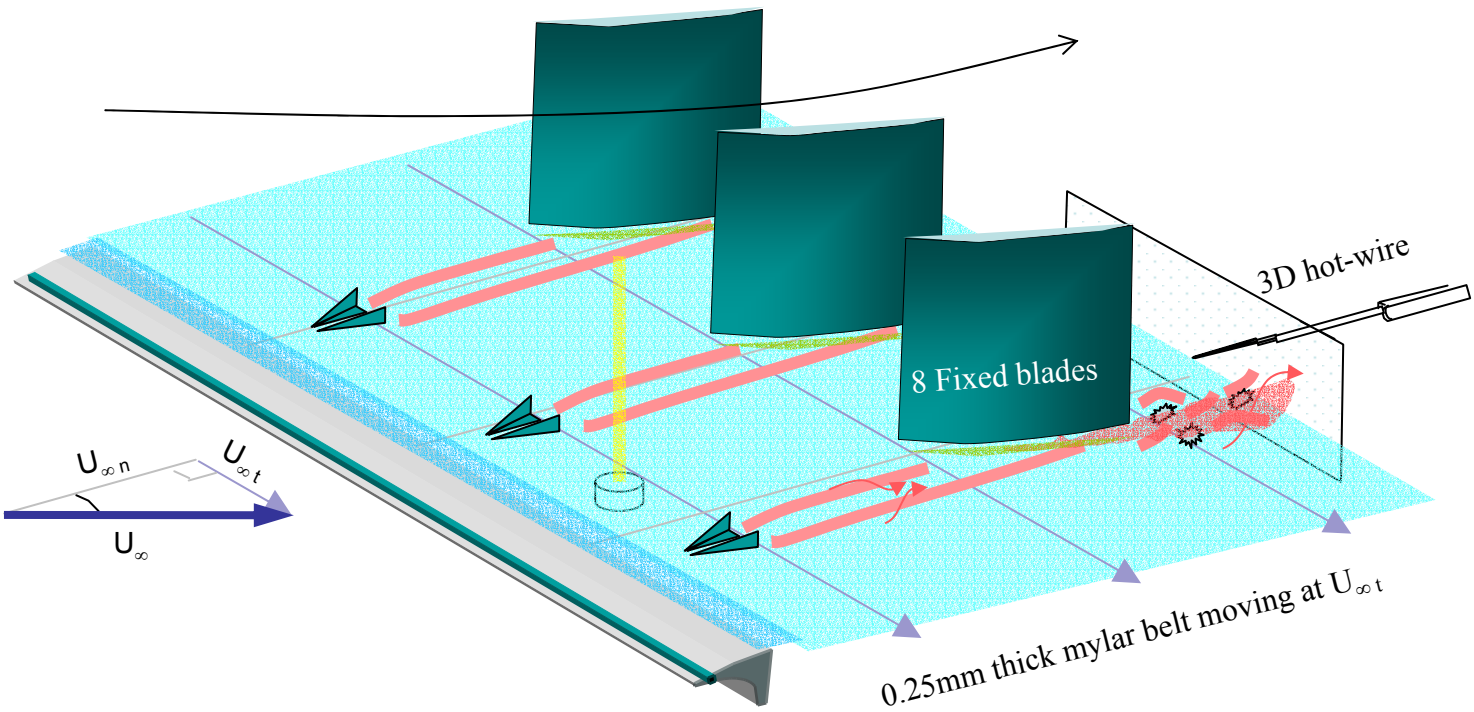

Figure 1-1: Model of the linear cascade tunnel used by Ma (2003).

CHAPTER TWO

2. Apparatus and Instrumentation

To acquire the data necessary to determine the effectiveness of trailing edge treatments, the Virginia Tech Linear Cascade Wind Tunnel was used. A detailed description of this tunnel as well as the measurement system and techniques used to realize the above goal are expanded upon in the sections of this chapter.

2.1 Low Speed Linear Cascade Tunnel

The Virginia Tech low speed linear cascade tunnel is an 8-blade, 7-passage linear cascade tunnel (blade row shown in figure 2-1). It was built in 1996 by Muthana (1998) who studied in detail the tip leakage vortex dominated flow as a function of the different tip gap settings of the compressor cascade. To simulate the effects of the relative motion between the blade tips and the end wall, the tunnel was modified to accommodate a moving wall system Wang (2000). Ma (2003) further modified the tunnel to allow for the attachment of vortex generators to the moving wall system to study the unsteady behavior of the tip leakage vortex downstream of the compressor blade row.

The blades used in this tunnel were originally designed and investigated by Wisler (1977, 1981) at General Electric, for the third stage of a core compressor found on an aircraft engine (blade profile shown in figure 2-2). Even though these blades were designed for a core compressor, the CFD work by Moore *et al.* (1996), Shin *et al.* (1999) and Shin (2001) showed that the blade loading for this configuration at low speed matches qualitatively the blade loading produced by a subsonic aircraft engine fan blade during take-off. Since the goal of this study, as stated in chapter 1, was to investigate the

effects of trailing edge modifications on the structure and development of the wake of a fan blade in an aircraft engine, these blades ideally produce the conditions necessary for an accurate investigation.

2.1.1 Upstream Section

The cascade tunnel can be broken up into two major sections: the upstream section and the test section. The upstream section consists of the fan, the settling screens, the diffuser and the contraction which is shown in figure 2-3.

Flow is supplied to the tunnel through a centrifugal fan which is powered by a 15 horsepower AC motor. The centrifugal fan has a diameter of 1.12m, a total length of 1.42 m and an exit area of 0.521m^2. After passing through the fan, the flow is slowed down through a diffuser before entering the settling chamber. The total length of the diffuser and the settling chamber is 4.26m while the expansion ratio from the exit of the fan to the settling chamber is 1:2.857. Before exiting the settling chamber and entering the contraction, the flow passes through flow conditioning screens to reduce the turbulence levels and swirling. The contraction, with a contraction ratio of .53:1 directs the flow into the inlet of the test section.

2.1.2 Test Section

The test section is composed of four main sections as shown in figure 2-4. The first is the inlet section which contains the boundary layer scoops used to eliminate the endwall boundary layers prior to entering the blade row. The second section houses and supports the blade row in the tunnel. Everything downstream of the blade row is contained in the third section. The final component is the moving wall system.

2.1.2.1 Inlet Section

The inlet section (side views shown in figures 2-5 and 2-6) begins at the exit of the contraction and it is rectangular in cross-section with flow in the potential core flow traveling perpendicular to that cross-section. The width of the inlet section is 0.762 m and the height is 0.3048 m. The walls of this section are not of equal length because of the angling of the downstream blade row. The short side wall up to the boundary layer suction slot is 0.85 m in length while the long side wall is 2.35 m in length. Since the walls are not equal, an exit plane of 1.81 m in length is created that is angled 24.9º with respect to the potential core.

Boundary layer scoops are located at this exit plane, which is located 187.6 mm axially[1] upstream of the blade row leading edge plane. The scoops are located on both the upper and lower end walls with each scoop having a height of 0.0254 m. The scoops are shown in detail in figure 2-7 and remove the boundary layer prior to the blade row. Since the pressure in the tunnel is higher than atmospheric, the pressure difference draws the boundary layer out of the tunnel. The amount of boundary layer that can be removed across the scoop is adjusted manually by moveable covers located outside of the tunnel. a 2.4 mm square boundary layer trip located 7 mm downstream of the leading edge of the lower endwall scoop trips the new endwall boundary layer that flows into the blade tips.

An additional boundary layer bleed section for the lower wall is located on the floor upstream of the boundary layer scoops (see figure 2-8). This consists of a porous section of the lower wall formed from a 762 mm by 63.5 mm perforated stainless steel sheet located 483 mm downstream of the contraction exit. Without this additional bleed the boundary layer suction slot scoop on the lower end wall does not adequately remove the entire boundary layer on long side of the tunnel resulting in a non-uniform inflow.

In the summer of 2003, prior to the present work, the cascade tunnel was taken apart and moved to a new laboratory location To check if the tunnel maintained the same flow conditions at the entrance of the test section, a cross-sectional measurement was performed 305 mm downstream of the entrance to the test section (figure 2-9). Figure 2-10 (a) shows a contour plot of the local velocity, normalized on the free stream velocity, as a function of the height above the lower endwall (y-axis) in centimeters and the

[1] Distances perpendicular and parallel to the blade row leading edge plane as are referred to as ‘axial’ and ‘pitchwise’, by analogy with the turbomachine.

distance across the tunnel with respect to the long side wall (x-axis) in centimeters. Figure 2-10 (b) shows the local turbulence intensity in the flow direction, normalized on the free stream velocity, as a function of the same coordinates. The mean velocity varies by less than 1%U_∞ across the inlet section. The turbulence levels vary from 0.26 to 0.28% for the clean flow part of the tunnel (not in the vicinity of the reference Pitot-static probe or the endwalls). This is very similar to the inflow Muthanna (1998) measured.

Typical freestream velocities, U_∞, in the inlet section were approximately 24.7 m/s. The Reynolds number based on the total chord length, c, of the blade was 390,000.

2.1.2.2 Blade Row

The baseline blade row consists of eight aluminum cantilevered GE Rotor B blades mounted to an aluminum superstructure which is bolted to the steel frame of the tunnel as shown in figure 2-11. The blades have a rounded leading and trailing edge, with a maximum thickness of 11 mm occurring at 60% chord (figure 2-2). The chord length of the blade is 0.254 mm and the span is 0.279 mm. The blade row is 188 mm axially downstream of the leading edges of the boundary layer suction scoops.

To simulate the flow field of an infinite cascade, the tunnel was designed with eight blades and seven passages. The basis for this was from the computations performed by Moore *et al.* (1996) on the cascade blades which showed 5 or more passages was sufficient. Pitchwise periodicity is improved by adding more passages but due to the limitations of the facility housing the tunnel, 7 passages were deemed to be optimal quantity.

The blades fit through close-fitting slots in the 6.35 mm thick Plexiglas upper end wall and are held a fixed distance above the lower end wall by the support superstructure. The support superstructure is constructed of a 76.2 mm by 25.4 mm aluminum box section. Six bolts hold the blades to superstructure, four of which are used to adjust the sweep, pitch and the distance between the lower end-wall and the tip of the blade, which is referred to the tip gap, as shown in figure 2-12. To set the tip gap, the superstructure is first shimmed by using gage blocks, figure 2-13, and then the fine adjustment is performed by the screws in the superstructure. The typical tip gap settings for this tunnel

are 2.1 mm, 4.2 mm, 5.6 mm, and 8.4 mm which is 0.83% 1.65%, 2.2% and 3.3% of the blade chord. For this study, the tip gap setting that was selected was 4.2mm or 1.65% chord.

To seal the opening in the Plexiglas upper end wall where the blades are inserted, blade root covers are used. The blade root covers were designed to maintain a maximum opening of 1 mm and tabs on the covers are used to ensure that the spacing is equal on both the suction and pressure sides of the blades and are shown in figure 2-14. The blade root covers were made from 76.2 mm by 342.9 mm galvanized steel sheets of 0.508 mm thickness. The covers were cut in half to allow them to be easily installed. To hold the covers in place double sided tape was used, and to provide a smooth transition between the upper end wall and the covers steel tape was used around all four edges.

The stagger angle of the blade row is 56.9 degrees, the inlet angle is 65.1, as shown in figure 2-4, and the blade spacing is 236mm. The span of the blade inside the tunnel is approximately 254 mm less the tip gap. On either side of the blade surface, boundary layer trips created from 0.5 mm diameter glass welding beads can be found. They are 6.4 mm wide, run the of span of the blade and are located 25.4 mm downstream of the leading edge as shown in figure 2-15.

On either side of cascade blade row sidewall scoops are located on the walls. The sidewall scoops remove the boundary layer on the walls and are formed by the gap between the blade surface and sidewalls of the tunnel test section as shown in figures 2-16 and 2-17. The openings have the same height as downstream sidewalls of 256 mm with a width of 28.6 mm on the short side and 38.1 mm on the long side. To adjust the size of the openings aluminum angle is used.

2.1.2.3 Downstream Test Section

Tailboards are used to guide the flow downstream of the blade row. These are hinged to the surfaces of blades 1 and 8, and can be adjusted to different angles as shown in figures 2-18 and 2-19. When installed the tailboards fit between the upper and lower end walls, with a small opening between the lower end wall and tailboard to allow room for the moving wall belt to pass under. The end walls were adjusted for a turning angle of

11.8 degrees, this having been determined previously (Ma, 2003) as the turning angle of the cascade. Once the end walls were set to the correct turning angle they were clamped to tunnel with adjustable C-clamps.

The upper end wall of the tunnel downstream of the blade row is constructed of 0.254 mm thick Plexiglas. The Plexiglass is slotted to allow for the insertion of probes at different axial locations. The slots were cut with a spacing of 46 mm in the axial direction and they each have a length of approximately 1.1 m to allow a probe to be traversed across four successive blade passages. Any slots that are not used were sealed with clear plastic tape to prevent the additional leakage of fluid.

At the exit plane of the tunnel, about 1.780 m downstream of the trailing edge of the blade row, two or three screens can be fitted as shown in figure 2-20. These screens are used to raise the pressure in the tunnel to ensure proper operation of the boundary layer scoops and bleed. The pressure upstream of the screens will be referred to as back pressure in this report. The screens were constructed of aluminum frame and screen material with an open ratio of 69.5%. One of the screens always had duct tape attached to it to increase the blockage, thereby increasing the back pressure of the tunnel. To hold the screens in place, clamps were attached across the back plane of the tunnel frame and duct tape was used around the outside edge of the frame to seal them.

To measure the back pressure, three aluminum 0.762 mm diameter pressure ports embedded in the lower end wall 127 mm upstream of the tunnel exit plane were used. The pressure ports are connected together using 1.588 mm diameter Tygon tubing and wye connectors. The average pressure of the three ports was measured by a pressure transducer.

2.1.2.4 Moving Wall System

A moving wall system designed by Wang (2000) and modified again by Ma (2003) can be used to simulate the relative motion between the tip of the fan blades and the casing of the engine in order to investigate the effects of this motion on the tip leakage vortex and wake near the lower end wall. To simulate this motion a Mylar belt

with a thickness of 0.254 mm was used. Within the scope of this experiment the moving endwall system was not used, but it is described as a component of the cascade tunnel.

The Mylar moving wall runs on top of a bed located underneath the blade row as sketched in figure 2-4 and shown in figure 2-5. This end wall is made from rectangular piece of plywood which is 3.2 m by 80 mm. To reduce the friction between the belt and the table as well as improve the belt life, a layer of 1.6 mm thick Teflon sheet was adhered to the surface of the plywood bed. The 0.254 mm belt itself is 686 mm wide and it extends approximately 124 mm axially upstream of the blade load row leading edge, and 423 mm axially downstream of the trailing edge line.

The belt is driven and guided by two large rollers located on either side of the bed and the two rollers are 203mm in diameter and are 762 mm wide as shown in figure 2-21. The belt is draped across the two rollers and forms a continuous loop running across the top of the Teflon bed and around the bottom of the tunnel outside of the test section. The rollers are mounted 3.760 m apart, with the upper surface level with the Teflon bed. When running the moving wall, the Mylar belt drifts axially across the surface of the Teflon bed. To prevent the Mylar belt from drifting too much an operator can add or remove tension from the leading or trailing edge of the Mylar belt by adjusting the pitchwise location and angle of the control roller using two large screws as shown in figure 2-21(b). The roller is mounted on take-up bearings, figure 2-21(c), to allow it to be moved pitchwise. Also, the control roller has a 0.0762mm crown for improved belt traction.

To construct a belt of a continuous loop, a belt joint of 80 to 100 mm wide strip is created when the two ends of the belt are overlapped as shown in figure 2-4. The overlapped ends of the belt are melted together at several hundred points by using a soldering iron. Clear plastic tape is used to seal the edges of the joint in order to prevent the belt joint from splitting opening while running. To reduce the stress in the belt, the belt joint was skewed to 40 to 45 degrees out of the plane perpendicular to the axis of rotation.

The leading edge of the belt is covered to prevent the flow from going under the belt and lifting it up. The belt cover was made from 25.4 mm wide, 0.127 mm thick Mylar strip. It was affixed to top of the lower end wall boundary layer scoop using

double sided tape. To discharge the static electricity produced by the belt passing over the Teflon bed, anti-static brushes are mounted above and below the belt outside of the tunnel. These brushes discharge the static electricity to ground.

The drive roller for the moving wall system is driven by a 15 HP AC synchronous motor, figure 2-21(a), which pulls the belt across the test section and returns it back under the tunnel. The speed of the motor is controlled and monitored by a TOSHIBA Tosvert-130G2+ digital variable frequency controller. This variable frequency controller can maintain the speed of the belt to within 1% of the tunnel flow velocity. Normally, the belt speed is run at the pitchwise component of the free stream velocity in order to ensure that the fluid particle traveling on the surface of the belt would only experience the axial velocity component.

The speed of the belt was measured by using a photodiode detector embedded in the Teflon bed underneath the belt 80.5 mm axially upstream of the leading line directly between blades 4 and 5. The photodiode was used to time the passage and two pairs of 6.35 mm wide black electrical tape strips, spaced 20 mm apart on the belt as shown in figure 2-4. The photodiode detector is illuminated by laser beam is shone down from outside of the tunnel through the Mylar belt. The beam is cut by the passing electrical tape strips. The passing of the strips was timed using a Tektronix 2211 Digital Storage Oscilloscope. Knowing the time and the distance, the speed of the belt was determined.

2.2 Two-Axis Traverse

A two-axis traverse was used to support the probes and position them in the tunnel as shown in figure 2-22(a). Each axis of the traverse was moved by a Compumotor model S-57-83-MO stepper motors with the motors being controlled by Parker PDX13 single-axis package mini-step shown in figure 2-22(b). The programmable traverse's movement had a resolution of 0.025mm per step. To mount the probes a carriage system, which could be moved in both directions, was used. The carriage system allowed the use of different probe holders, permitting it to be used for all measurements. The two-axis traverse was controlled by PC laptop running Agilent VEE.

2.3 Data Acquisition System

The data from the measurements in the cascade tunnel was acquired using an Agilent VXI system. The Agilent VXI system is composed of an Agilent E1432A module, an Agilent E8491A interface and an Agilent E8408A VXI mainframe. The first component, the Agilent E1432A module, is a 16-channel digitizer used to acquire the data. The module is installed into the C-size slot located on the Agilent E8048A VXI mainframe. Each module includes DSP, transducer signal conditioning, alias protection, digitization, and high-speed measurement computation. The mainframe itself can hold up to four modules. Also, installed on the mainframe is the Agilent E8491A interface which links the mainframe to the IEEE 1394 serial bus. The serial bus links the mainframe to a PC. Data can be delivered to a PC a maximum of 51,200 simultaneous samples per second per channel with a 16-bit resolution. The residual DC input of the E1432 module is $\leq \pm$ 1% of the range, ±10 mV. The root mean square of the noise for a 23 kHz span is less than 45 μ Vrms.

A Pentium laptop running the visual programming language Agilent VEE, was used to acquire the data and control the movement of the traverse. The software was programmed to convert the output voltages from all of the different measurement hardware to time-series

2.4 Pressure Measurements

Pressure measurements were made in the cascade tunnel to determine the total, dynamic and static pressures. To measure the total, dynamic and static pressures in the tunnel Pitot-static probes were used, static pressure ports located on the blade were used to measure the pressure distribution on the surface of the blades and pressure taps located in the tunnel lower end wall were used to measure the back pressures.

2.4.1 Pitot-Static Probes

To measure the total, dynamic and static pressures in the cascade tunnel, multiple Pitot-static probes were used. The free stream total, $P_{o,\infty}$, dynamic, $q_{\infty,}$ and static P_{∞} pressures were measured by a Pitot-static located in the upstream section of the test section. A Dwyer Instruments Standard Model 160 Pitot Probe (Model 167-12), with a shaft length of 305 mm and a tip length of 76 mm as shown in figure 2-23(a) was used to measure free stream conditions. This probe was located 0.931 m downstream of the contraction exit (measured to center of the shaft), 149 mm from the long side wall, and 122 mm from the upper end wall. A similar probe was used downstream of the cascade to measure the total, dynamic and static pressures in the downstream test section for tunnel calibrations.

The second type of Pitot-static probe used was a Dwyer Instruments Telescoping Pitot Tube (Model 166T) as shown in 2-23(b). The shaft of the Pitot-static probe can be extended from 30 cm to 103 cm and the Pitot-tube is 7.62 cm long with a diameter 3.175 mm. The static ports are located 2.70 cm from the Pitot port at the tip of probe. This probe was used primarily to measure the total, dynamic and static pressure cross-sections downstream of the baseline and modified trailing edge blades.

The third type of Pitot-static probe used was a larger Dwyer Instruments Model 160 Pitot Probe (Model 160-18) as shown in figure 2-24. The shaft of the Pitot-state probe is 47.63 cm long and the Pitot-tube extends 19.05 cm. The static ports are located 6.35 cm from the Pitot port. Two of these probes were mounted downstream of the cascade at midspan with a pitchwise distance of 46.83 cm (two blade spacings) between them using the aluminum probe holders shown in the figure. The probes were used to measure the static pressures at the mid-height of the tunnel downstream of the blade row for the blade loading study discussed in a later chapter.

2.4.2 Blade Pressure Ports

Located on the surface of the baseline blades are pressure ports used to measure the surface pressure as a function of chord. The pressure ports were made by embedding 1.6 mm diameter copper tubing into the surface of the blade. The copper tubes were fitted into channels cut into the surface of the blade and fixed in place with epoxy. Static holes

of 0.8 mm diameter were then drilled through the epoxy and into the tubes, Pressure ports were embedded on the suction side of blade 4 and the pressure side of blade 5 at 123 mm from the tip.

2.4.3 Pressure Transducers

To record the pressure measured by the Pitot-static probes, the pressure ports of the probes were attached to pressure transducers using clear plastic Tygon tubing. Various sizes of Tygon tubing was used, varying from 1.588 mm inner diameter for the back pressure ports to 6.350 mm inner diameter for the larger Pitot-static probes. Three different pressure transducers were used to for the pressure measurements. All three pressure transducers used were all Setra model 239 electric pressure transducers, each with a varying pressure and voltage range. One of the pressure transducers had a pressure range of ±7.5 inches of water and output of ±2.5 Volts DC, the second transducer had a pressure range of ±15 inches of water and output of ±2.5 Volts DC, and the third transducer had a pressure range of ±2.5 inches of water and output of ±2.5? Volts DC. The voltage output from the transducers was recorded by one of the channels of the Agilent E1432A.

Surface pressure measurements were performed by using two Setra electric pressure transducers and a CTLR2P/S2-S6 Scanivalve Corp scanivalve. The scanivalue has the capability of obtaining pressures from 48 pressure taps by using a built in stepper motor. The built in stepper motor rotates the pressure ports in sequential order for measuring. The stepper motor can be controlled by a 386 PC or manually.

The back pressure in the tunnel was measured by using a handheld Dwyer Series 427 Mark III handheld digital manometer. The digital manometers have a pressure range of 0 to 10 inches of water, with the pressure begin displayed on the handheld's LCD screen.

2.5 Hot-Wire Anemometry

The majority of the mid-section and cross-section measurements performed on the wakes in this study were performed using hot-wire anemometry. Both single and quad-wire measurement schemes were used to obtain a detailed understanding of the flow phenomenon in the wakes created by the baseline and modified trail edge configurations.

2.5.1 Hot-wire Probes

To measure the wakes, two types of probes were used. The first probe used was an Auspex Corporation single-wire probe. The single wire probe has a 0.5 mm long, 2.5 μm diameter tungsten wire supported between two stainless steel prongs. The probe was used to perform initial wake measurements determining the axial velocity and turbulence levels on baseline blade configuration.

A second type of probe was used to perform three-component velocity measurements in the wake. The three-component velocity measurements were performed using a miniature Kovaznay type four-sensor hot-wire probe manufactured by Auspex Corporation (type AVOP-4-100) shown in figure 2-25, which is described in detail by Wittmer *et al*. (1998). The probe is composed of eight 75 μm stainless steel tapered prongs suspending four etched tungsten wires of 5 μm diameter and a length of 1.4 mm each. The wires are suspended some 40 mm upstream of the main part of the probe. The wires are arranged in an X-wire array inclining each wire at a nominal 45 degrees with respect to the axis of the probe. With this configuration, the probe has a measurement volume of approximately 0.5 mm^3.

2.5.2 Hot-wire Anemometry

The four sensor probes were operated by using a Dantec 56C17/56C01 constant temperature anemometer unit (figure 2-26(a)) and the single sensor probe was operated by a Dantec 55M01 constant temperature anemometer unit (four sensor bridges shown in figure 2-26(a)). Both systems used an overheat ratio of 1.7. The quad-wire system was optimized to give a flat frequency response between 15.9 and 22.7 kHz while the single-wire system was optimized to give a flat frequency response to 19 kHz. Four x 10- buck-

and-gain amplifiers equipped with calibrated RC filters were used to buffer the hot-wire signals and limit their frequency response to 50 kHz. The amplifier system is shown in figure 2-26(b).

Velocity calibrations are performed on each of the probes to correlate the wire output voltages to the flow cooling velocities through King's Law. The velocity calibrations are performed in a TSI calibrator jet shown in figure 2-27. Angle calibrations, which are performed only on the four sensor hot-wires, are performed to create a look-up table to relate the three velocity components to the cooling velocities. The angle calibration is performed by pitching and yawing the probe through angles of -60 to 60 and -60 to 50, respectively, in a calibration jet and comparing the pitch and yaw angles with the probe output to obtain the direct relationship between the cooling velocity and the flow angles. The direct angle calibration method is described in full detail by Wittmer *et al.* (1998).

2.6 Tunnel Coordinate System

There are three coordinate systems used to describe the measurement locations. Two of the coordinate systems are blade row aligned, while the third coordinate system is wake aligned. The three coordinate systems are depicted in figure 2-28.

The first blade-row aligned coordinate system (x_1, y, z) has an origin located on the lower endwall half-way between blades 4 and 5 on the leading edge line of the blade row. The $x1$-axis is perpendicular to the leading edge line with the positive x_1 direction being directed downstream. The y-axis is perpendicular to the lower end wall with the positive y being towards the upper end wall. The z-axis is parallel to the leading edge line, and completes a right-handed system.

The second blade-row aligned coordinate system (x, y, z) is the same as the first, except that the origin of the axial coordinate x is at the trailing edge line.

The third wake aligned coordinate system (X,Y,Z) has an origin located at the trailing edge of blade 5. The X -axis is aligned with the flow direction and follows the wake centerline, the Y-axis is parallel to the spanwise y-direction, and the Z-axis is

perpendicular to the plane of the wake to complete the right hand rule. The corresponding velocities are defined as (*U, V, W*).

2.6.1 Mylar Measurement Grid

Since the same measurements at the same locations were to be repeated for the baseline blade and the modified blades sets, the measurement locations were marked out on a 0.254 mm thick Mylar sheet. On the Mylar sheet, the axial coordinate, x_1, the pitchwise coordinate, z, at multiple axial locations, and the assumed wake convection direction were drawn as shown in figure 2-29. To allow the Mylar measurement grid to be replaced in the same location for every measurement, multiple edges and corners of the Mylar grid were referenced on the lower endwall of the test section. A check of the origin location was performed to determine the accuracy of the method which was found to be accurate to within ± 1 mm.

2.7 Tunnel Calibration

Prior to performing any experiments the cascade tunnel needs to be calibrated to ensure that it correctly models an infinite blade row. The cascade tunnel is calibrated when the following conditions are met:

1. The inflow velocity matches the free stream velocity, i.e., there is no acceleration or deceleration across the boundary layer scoops
2. The potential core velocity remains constant across the inlet of the blade row. This also implies there is no pitchwise pressure gradient across the inlet.
3. Pitchwise periodicity, and thus no net pitchwise pressure gradient in and downstream of the cascade.
4. Wakes spacing equal to blade spacing (23.6 cm pitch wise)

The above conditions can be obtained met by adjusting three tunnel parameters; first the sidewall and upper and lower wall boundary layer scoops. By adjusting these, any acceleration or deceleration of the inflow will be corrected. Second, the angle of the

tailboards which adjusts the overall turning angle of the flow and can remove any net the pitchwise pressure gradient downstream of the cascade. Finally, the screen configurations at the tunnel exit, which control the back pressure. Adjusting the backpressure will ultimately change the pressure in the tunnel and the amount of flow being removed by the scoops.

In figure 2-30(a), the upstream pressure and velocity distribution can be found, following completion of the above adjustments. The pitchwise velocity and pressure distributions were measured at x/c_a = -0.65 (measured to the shaft of the Pitot-static probe) and y/c_a = 0.92, near the cascade midspan, where c_a is 139 mm. In figure 2-30(b), the downstream pitchwise pressure and velocity distributions can be found. The downstream distribution was performed at x/c_a = 1.79 and y/c_a = 0.92. The pressure coefficients C_p and $C_{p,o}$ found in the above figures are defined as:

$$C_p = \frac{P - P_\infty}{P_{o\infty} - P_\infty} \tag{2-1}$$

$$C_{po} = \frac{P_o - P_\infty}{P_{o\infty} - P_\infty} \tag{2-2}$$

where P is the local static pressure, P_∞ is the free stream static pressure, $P_{o,\infty}$ is the free stream total pressure, and P_o is the local total pressure. From the definition of stagnation pressure ($C_{p,o}$ = 1) the normalized local velocity can be determined by:

$$\frac{U}{U_\infty} = \sqrt{C_{po} - C_p} \tag{2-3}$$

where U is the local velocity and U_∞ is the free stream velocity.

In figures 2-30(a) and 2-30(b), the horizontal axis is the normalized pitchwise location, z/c_a, and y-axis is C_p, C_{po} and U/U_∞. Figure 2-30(a) shows a maximized velocity distribution with a U/U_∞ ratio of 1 across blades 3 through 6 satisfying the first requirement for a calibrated tunnel. Toward blade 2, the effects of the sidewall suction slot are seen as the pressure increases and the local velocity decreases. Overall, however, there is no net pitchwise pressure gradient which satisfies the second requirement.

Figure 2-30(b) shows the downstream pitchwise pressure and velocity distributions. These results show no net pitchwise pressure gradient across blades 2

through 6, satisfying the third requirement. The stagnation pressure and the velocity distribution are cyclic with the wakes being identified by the valleys. The wake region occurs periodically every z/c_a = 1.71 satisfying the final requirement for a calibrated tunnel. The stagnation pressure outside the wake region is equal to 1 showing that no additional work on the fluid was done as it passes through the cascade row.

While performing all of the measurements the backpressure (pressure measured at the exit plane of the tunnel) was maintained at a constant value. The backpressure coefficient was defined as:

$$C_{p,b} = \frac{P_b - P_\infty}{P_{o\infty} - P_\infty} \tag{2-4}$$

where P_b is the pressure measured by the pressure taps on the lower endwall at the exit plane of the tunnel. For all of the measurement runs, the backpressure coefficient was 0.40±0.004. Using the method detailed in Ma (2003), the total uncertainty in C_p was determined to be 1%.

Figure 2-1: GE Rotor B blades mounted in Virginia Tech's linear cascade tunnel

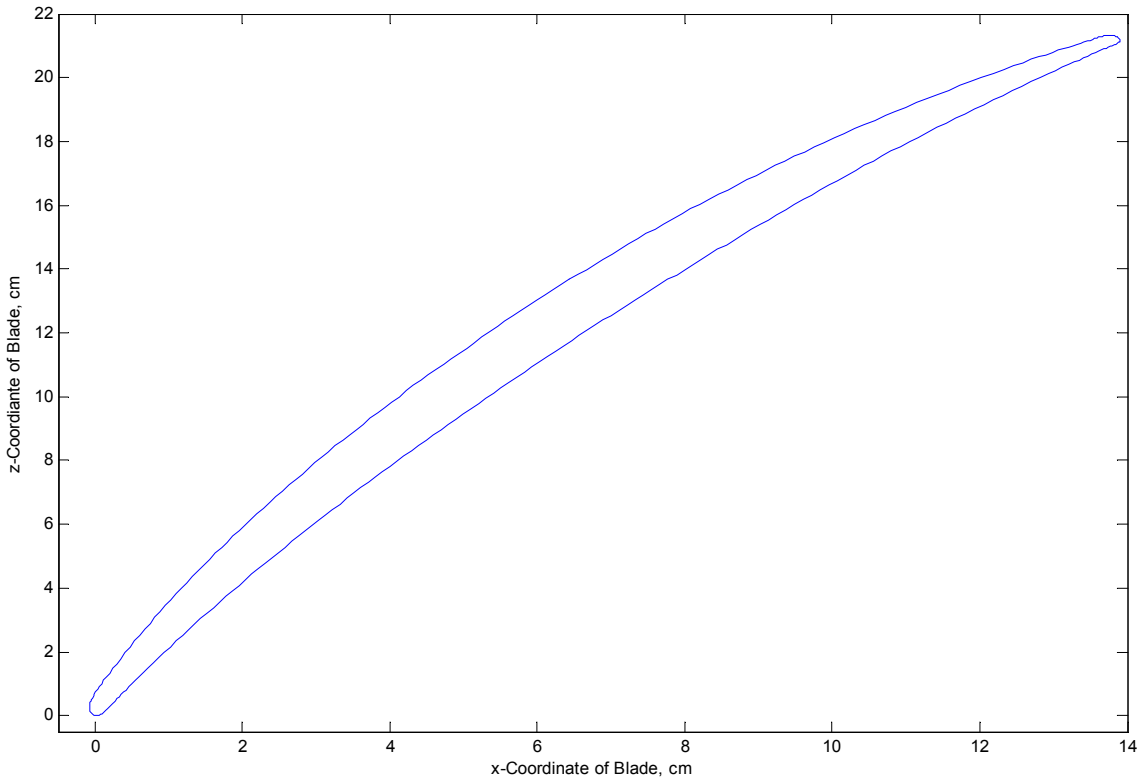

Figure 2-2: Profile of the GE Rotor B blade plotted as a function of the x_1- and z-coordinates

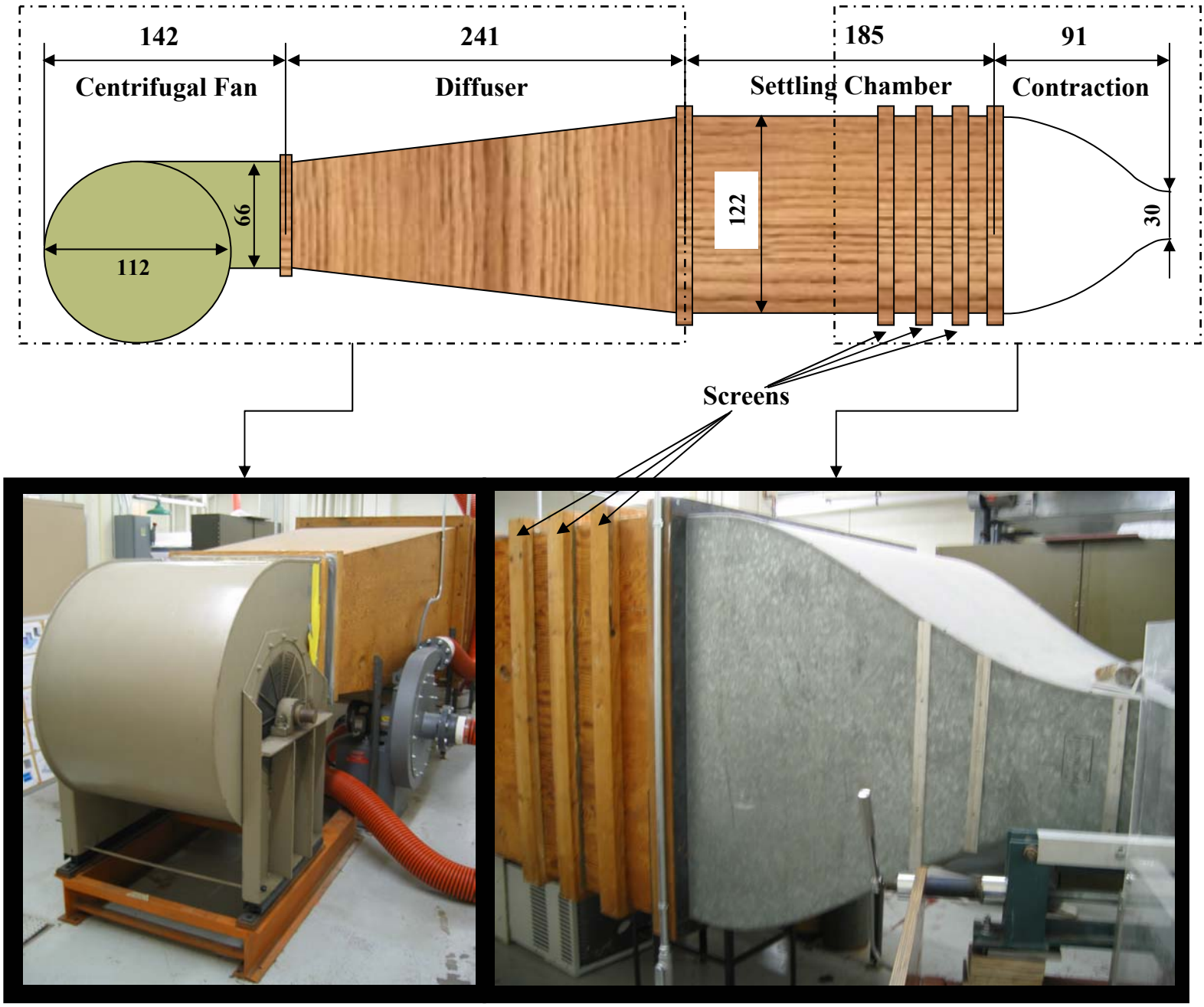

Figure 2-3: Side view of the upstream section of the Virginia Tech linear cascade tunnel showing the four major components. (All dimensions are given in centimeters)

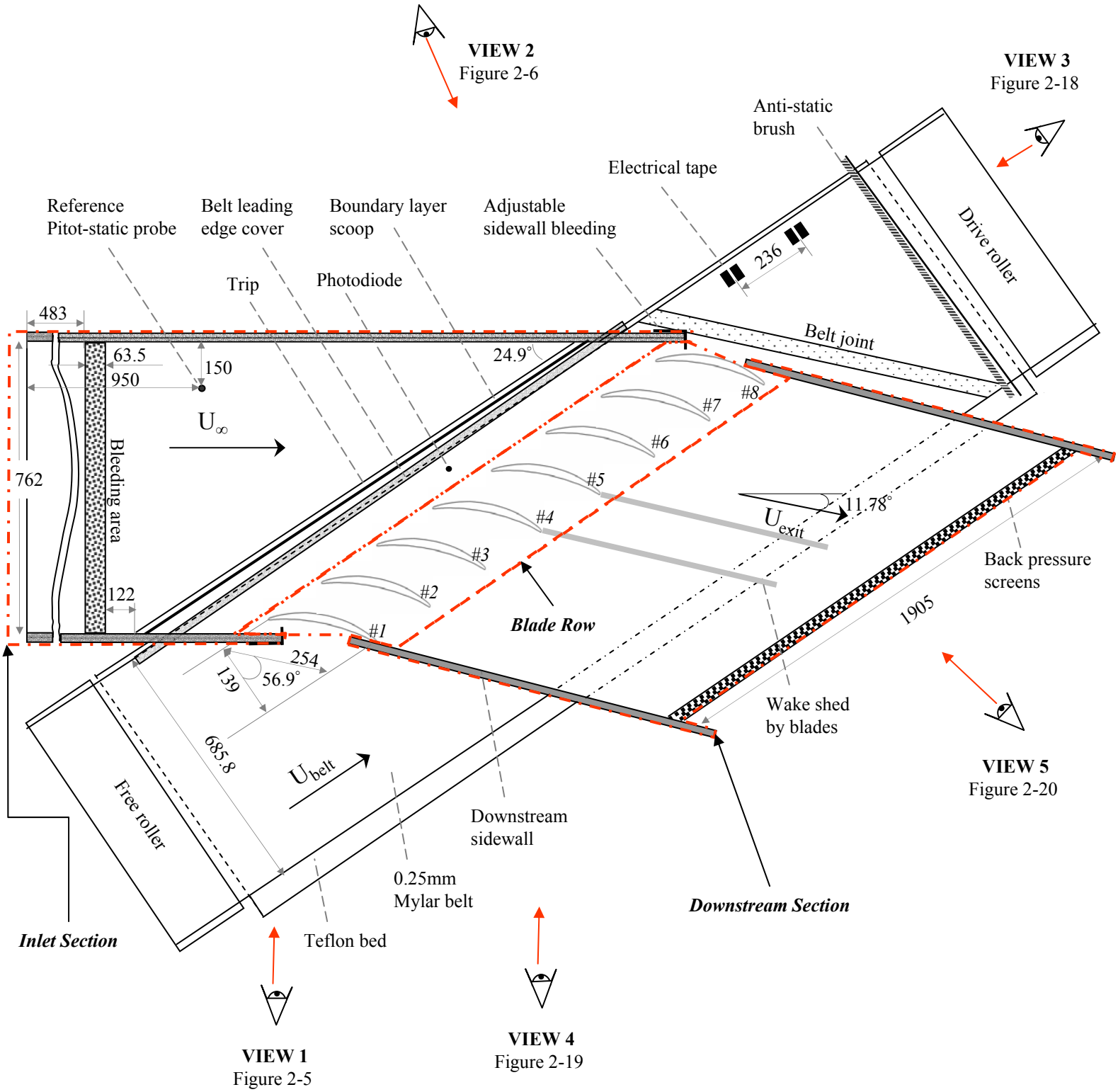

Figure 2-4: Top view of the test section of Virginia Tech's Linear Cascade Tunnel showing the inlet test section, blade row, downstream test and moving wall system (All dimensions are given in millimeters; figure courtesy of Ma (2003))

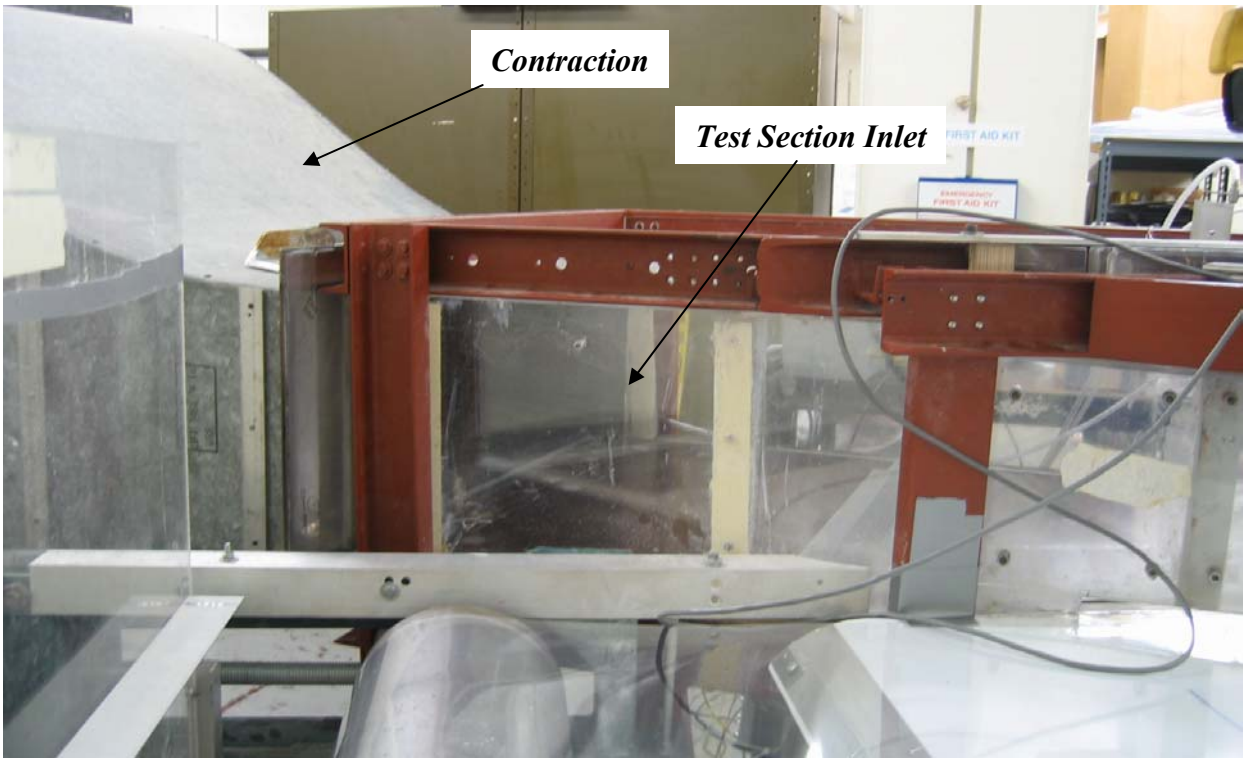

Figure 2-5: Side view of the short side upstream test section taken from the side moving wall system (view 1 in figure 2-4).

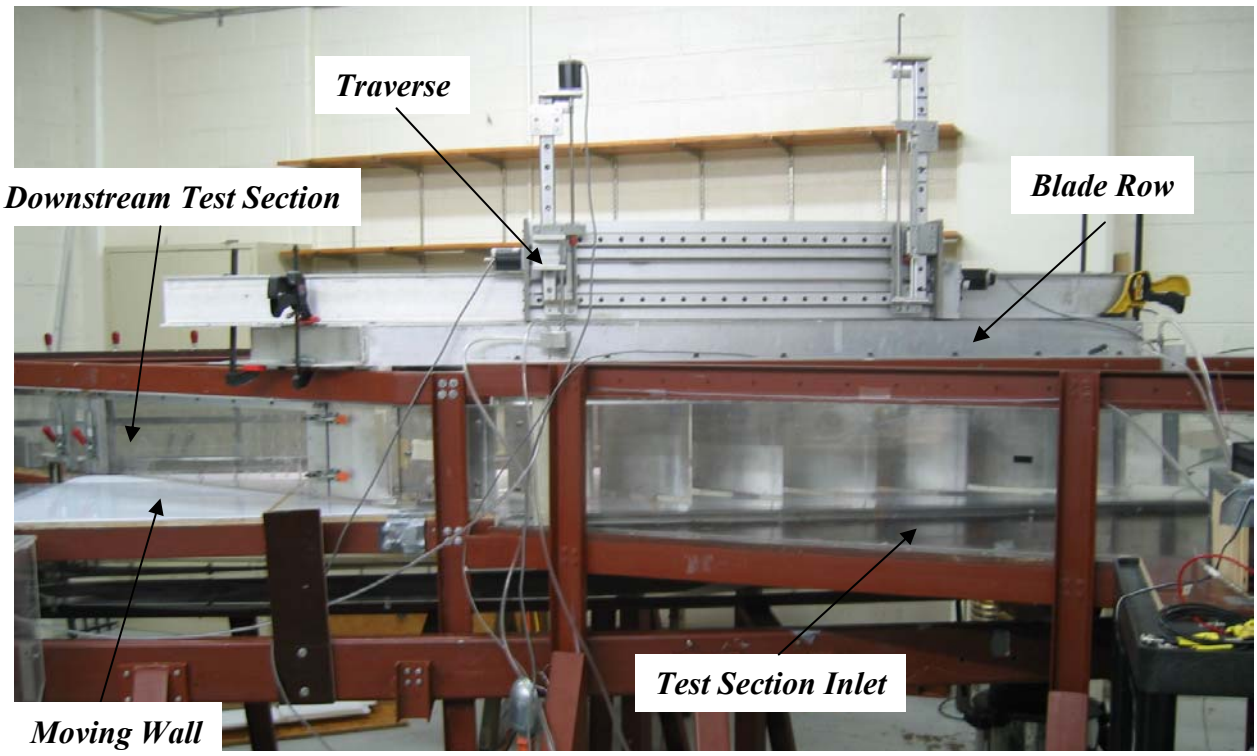

Figure 2-6: Side view of the entire test section taken from the long side of the cascade tunnel (view 2 in figure 2-4).

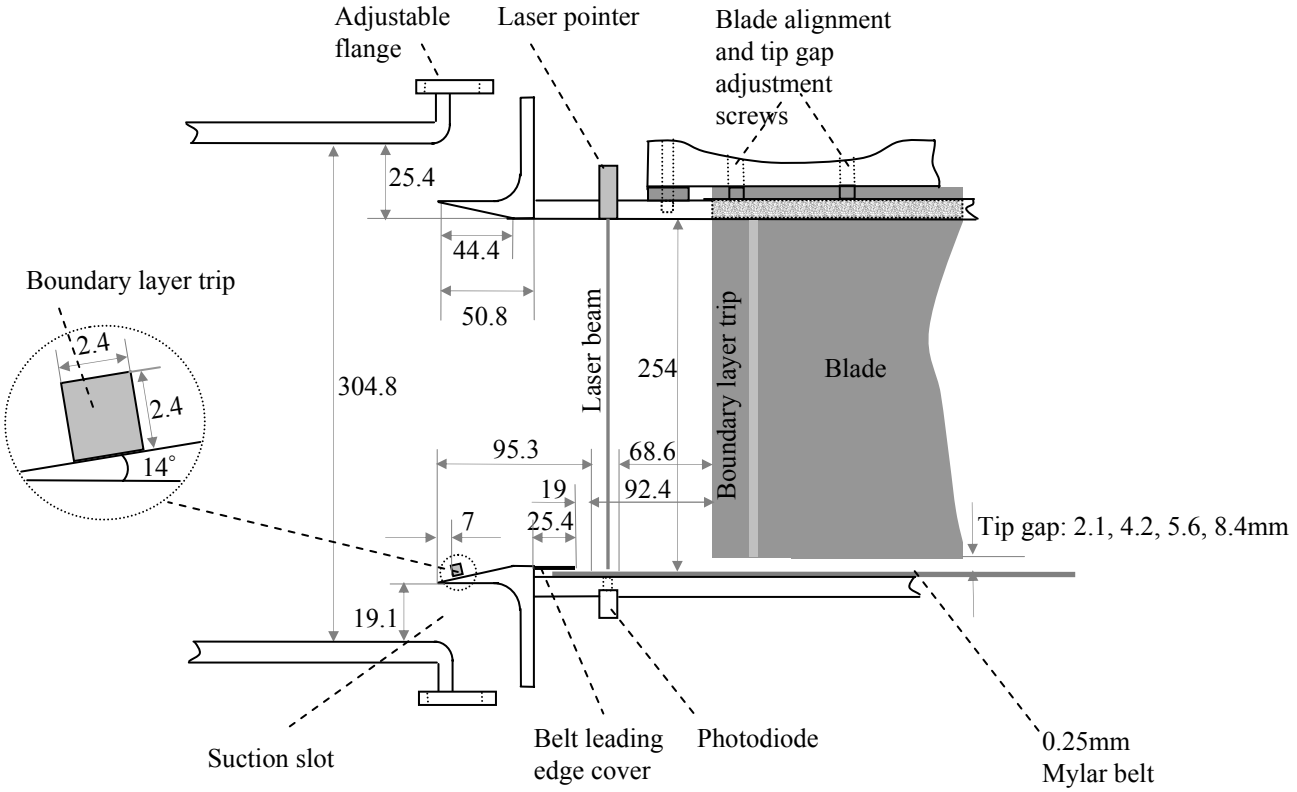

(a)

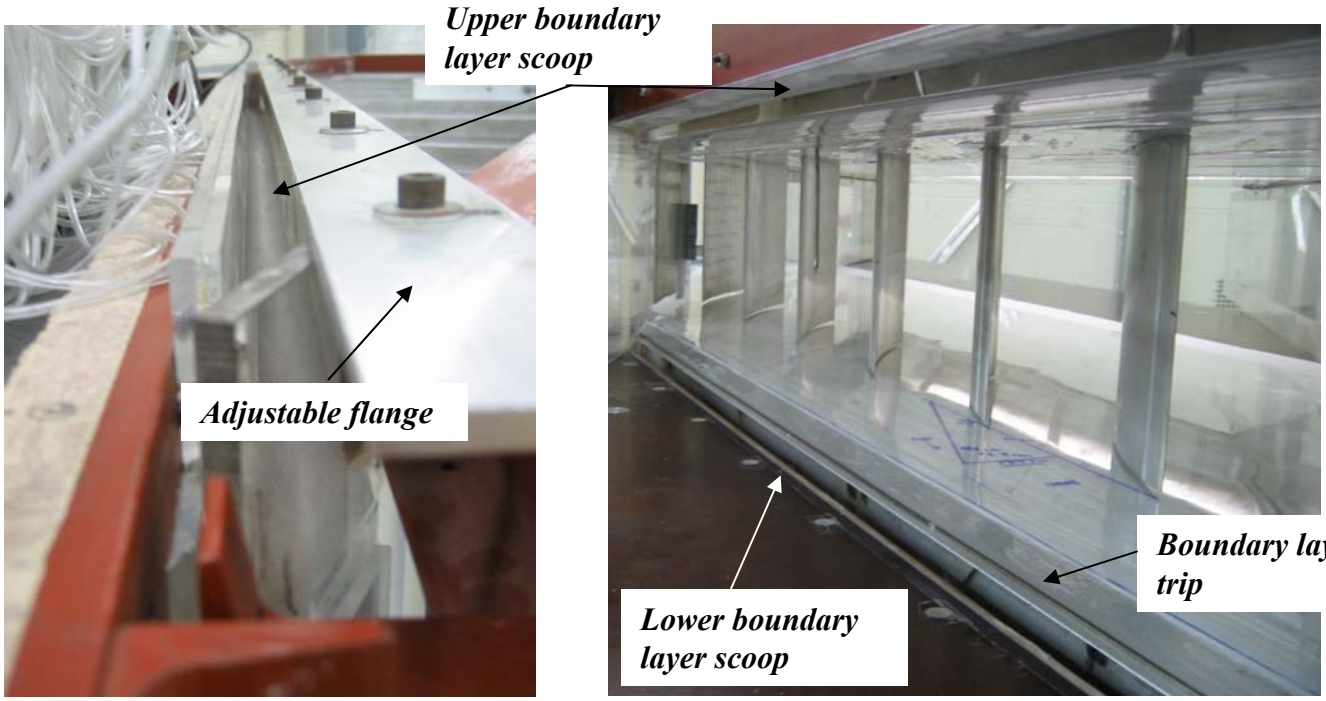

(b) **(c)**

Figure 2-7: Boundary layer in the inlet section of the test section: **(a)** Side-view sketch of boundary layer suction slots and blade row (Ma (2003)), **(b)** Outside view of upper boundary layer suction slot, **(c)** inside view of the upper and lower boundary layer slots

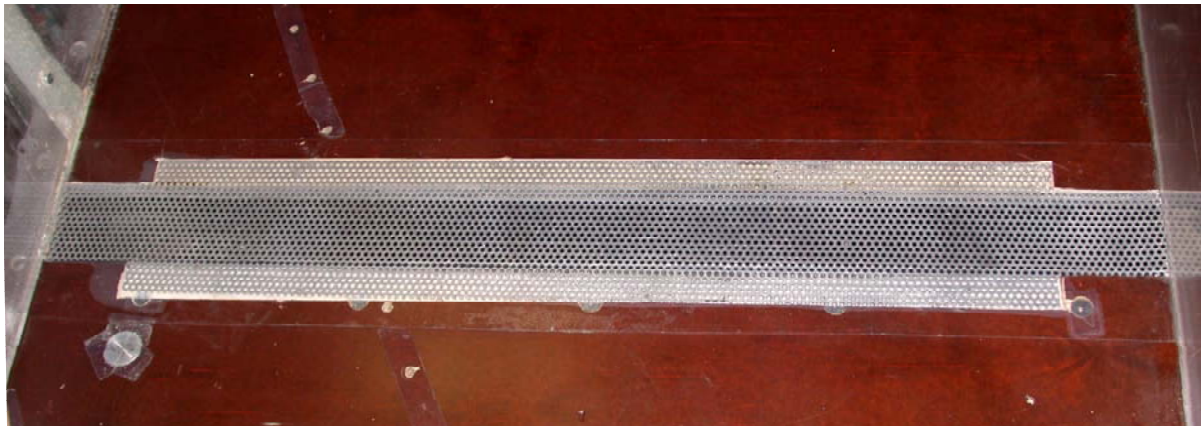

Figure 2-8: Upstream 762 mm by 63.5 mm rectangular bleed opening covered by a perforated steel sheet (Ma (2003)).

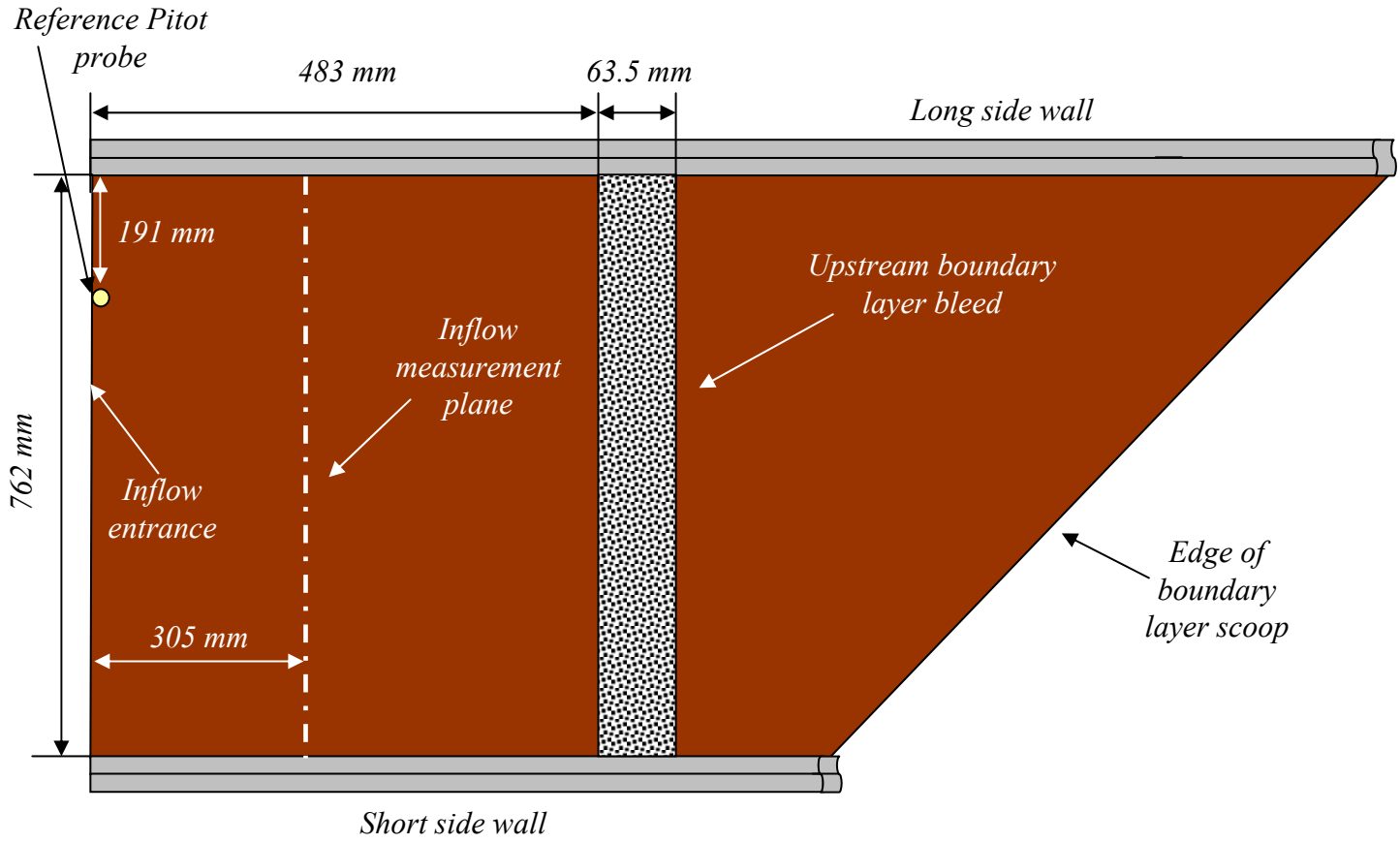

Figure 2-9: Diagram showing the location of the inflow cross-section measurement.

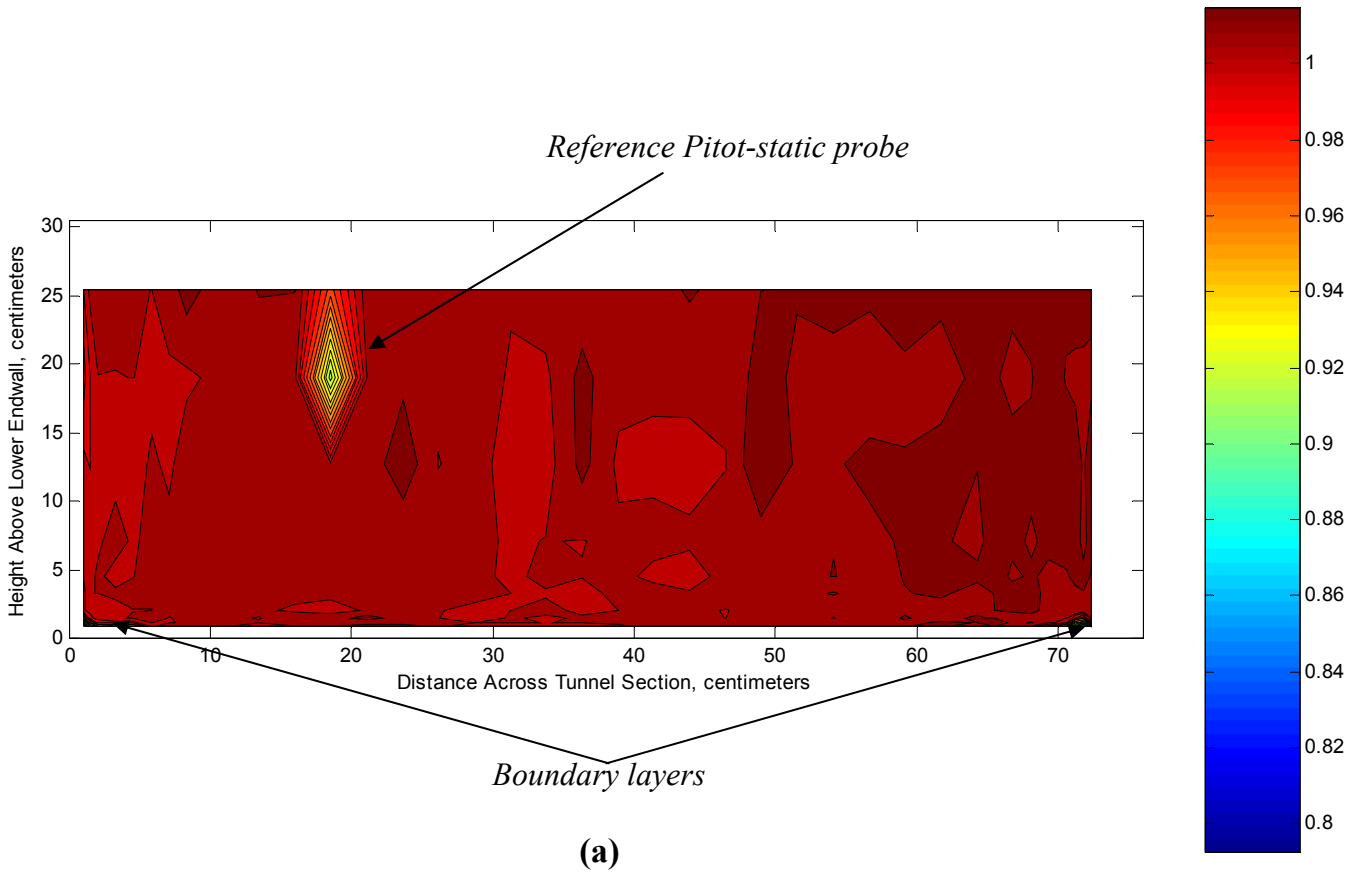

(a)

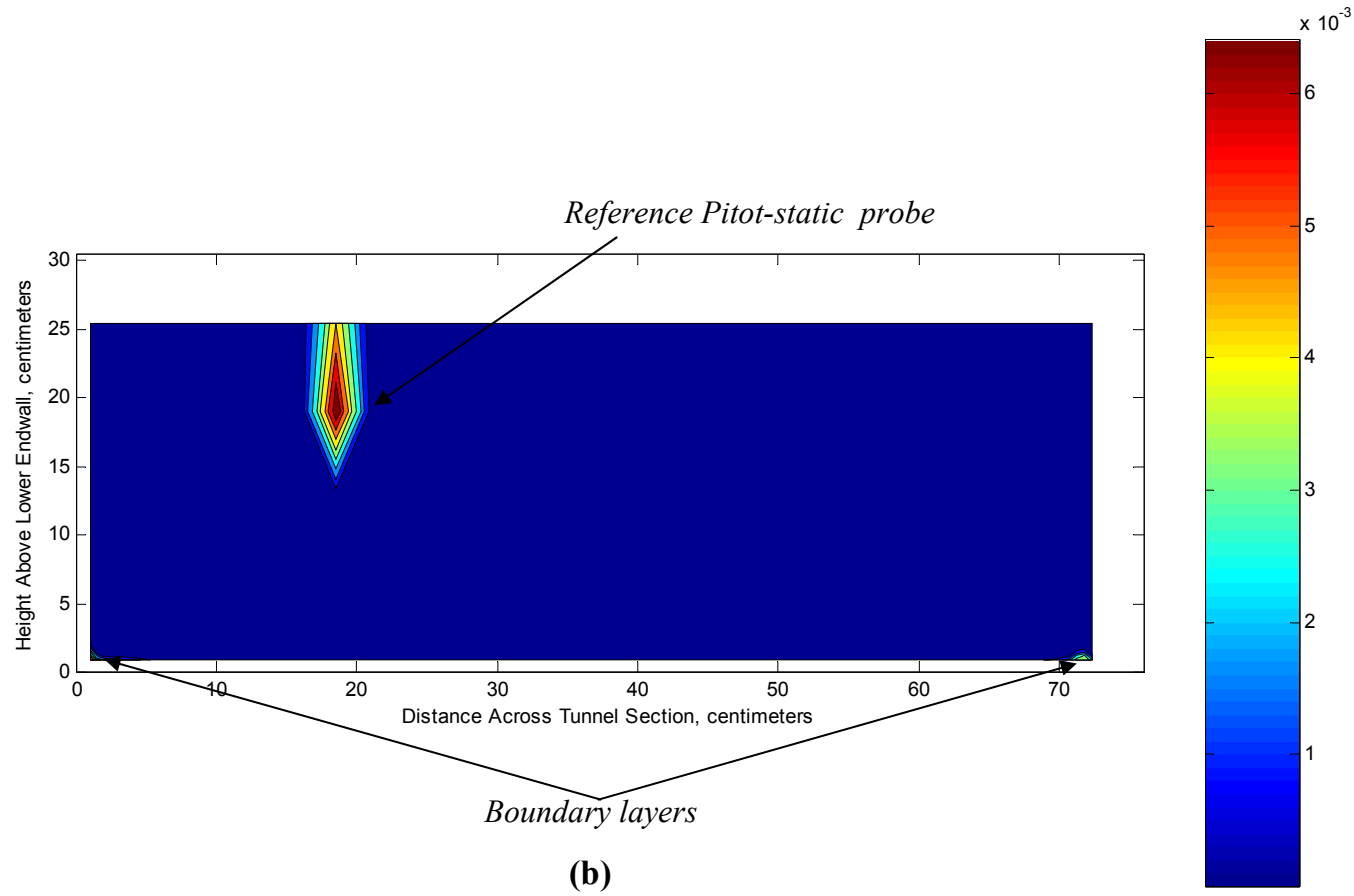

(b)

Figure 2-10: Flow properties of the inflow to the test section 30.5 cm downstream of the test section inlet: **(a)** velocity contour plot of U/U_∞, **(b)** turbulence contour plot of u^2/U_∞^2

Figure 2-11: GE Rotor B blades mounted in the cascade tunnel; view shown from the trailing edge.

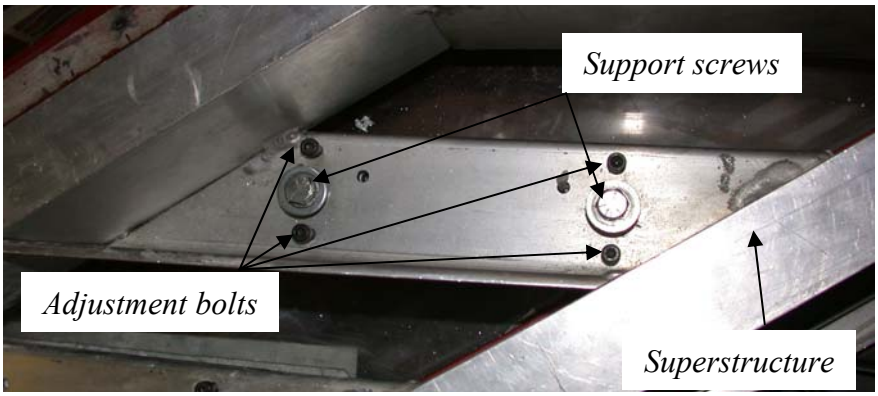

Figure 2-12: Top view of blade superstructure showing the adjustment bolts and support screws for one blade (Ma 2003))

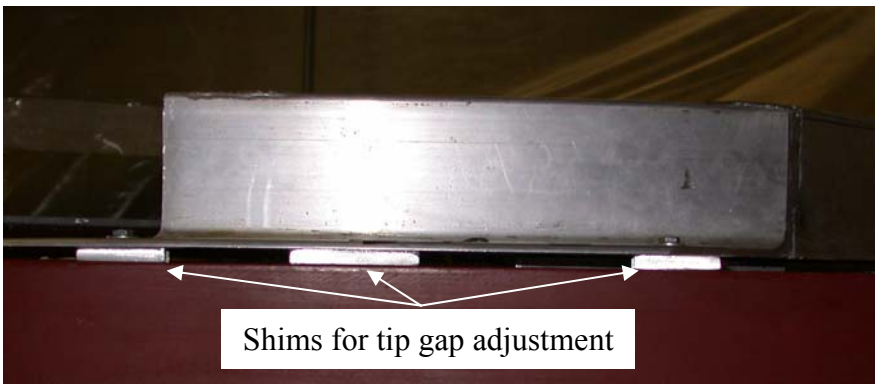

Figure 2-13: Shims used to preset the tip gap before using the fine adjustment bolts shown in figure 2-12 (Ma (2003)).

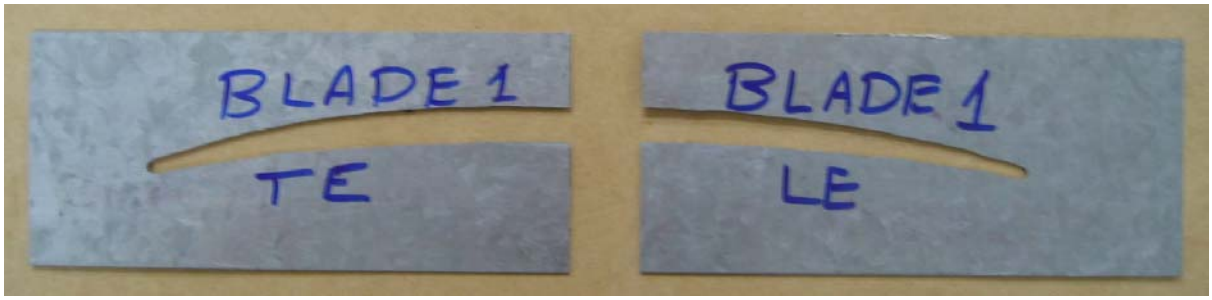

(a)

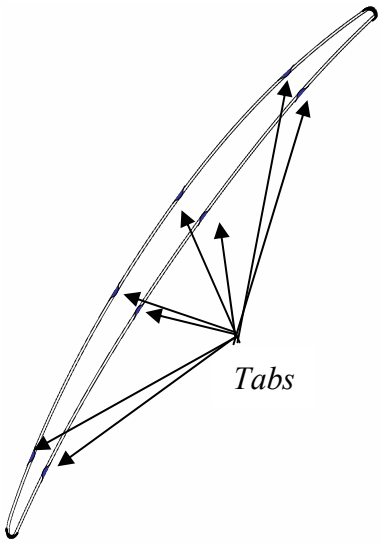

(b)

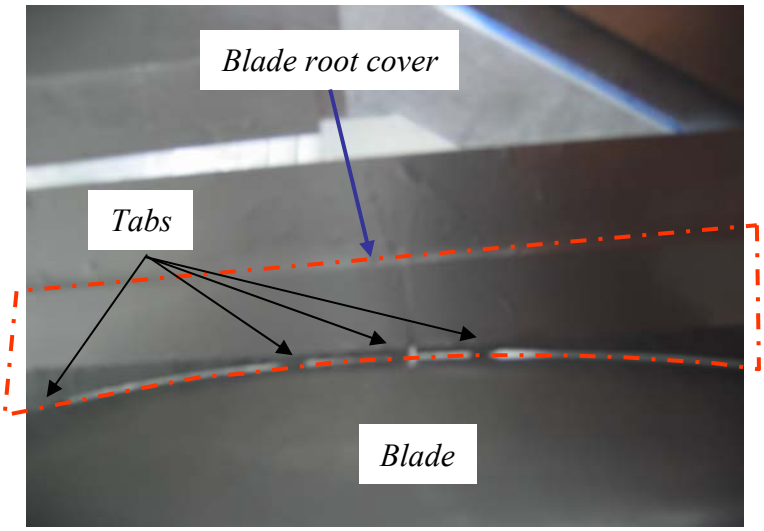

(c)

Figure 2-14: Blade root covers: **(a)** leading and trailing blade root covers, **(b)** profile used to make the blade root cover opening, **(c)** blade root cover installed in the tunnel showing 1 mm opening.

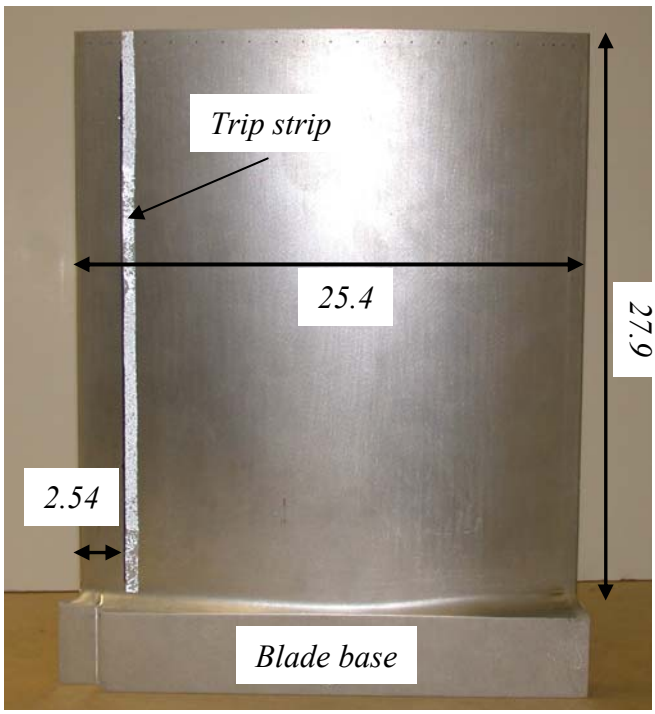

Figure 2-15: Plan view of GE-Rotor-B blade with dimensions (in cm).

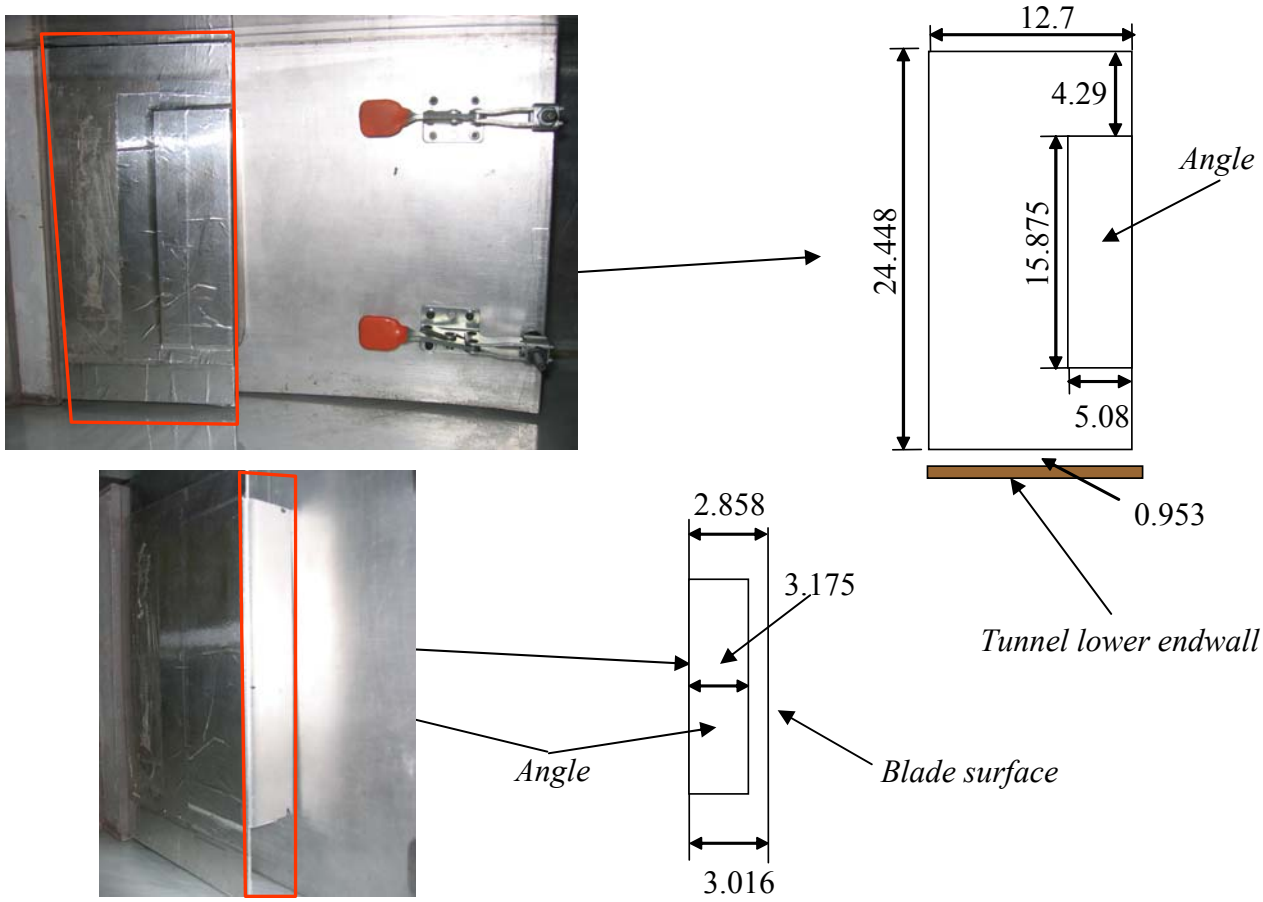

Figure 2-16: Short side boundary layer scoop (all dimensions in cm).

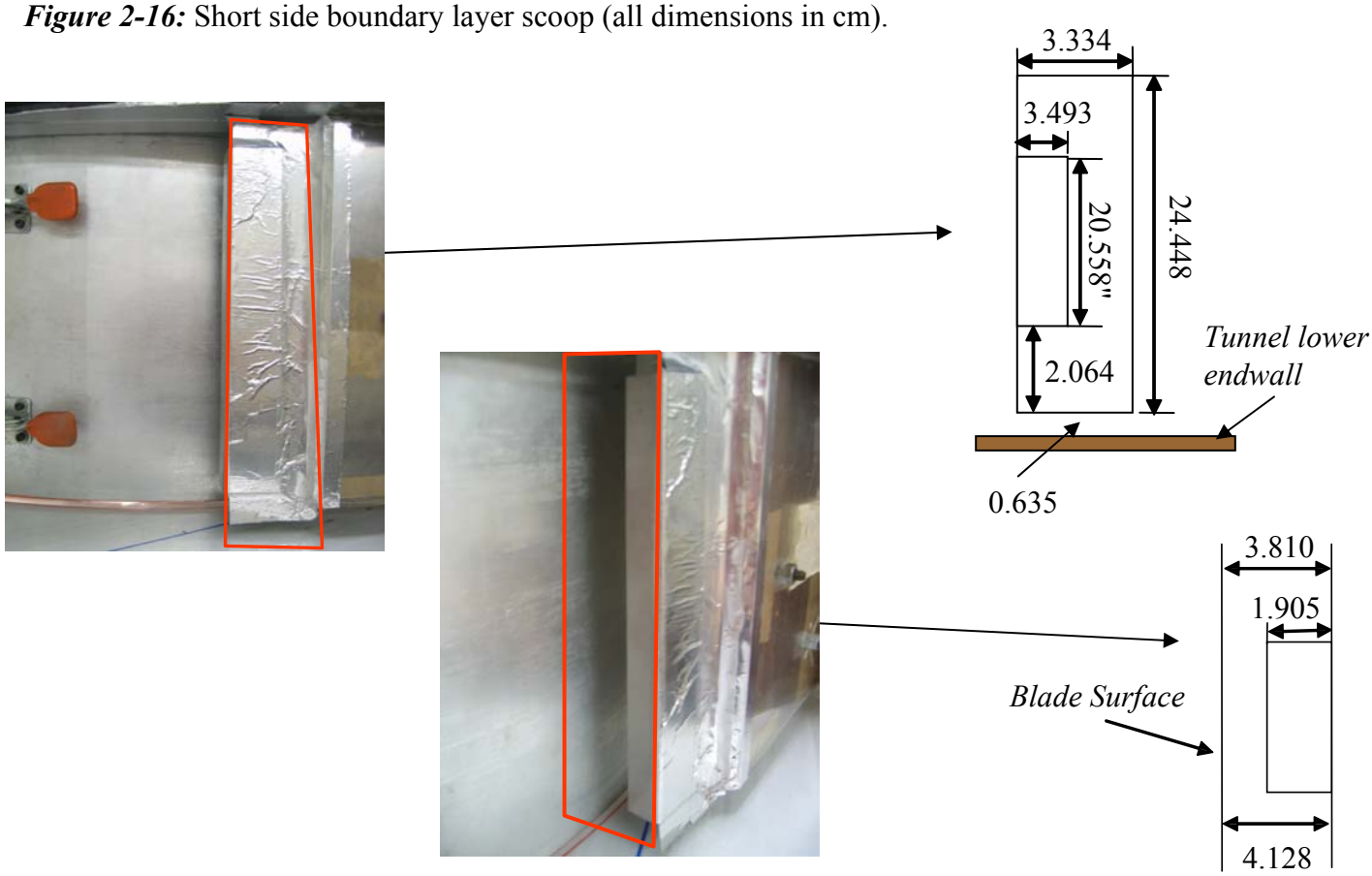

Figure 2-17: Long side boundary layer scoop (all dimensions in cm).

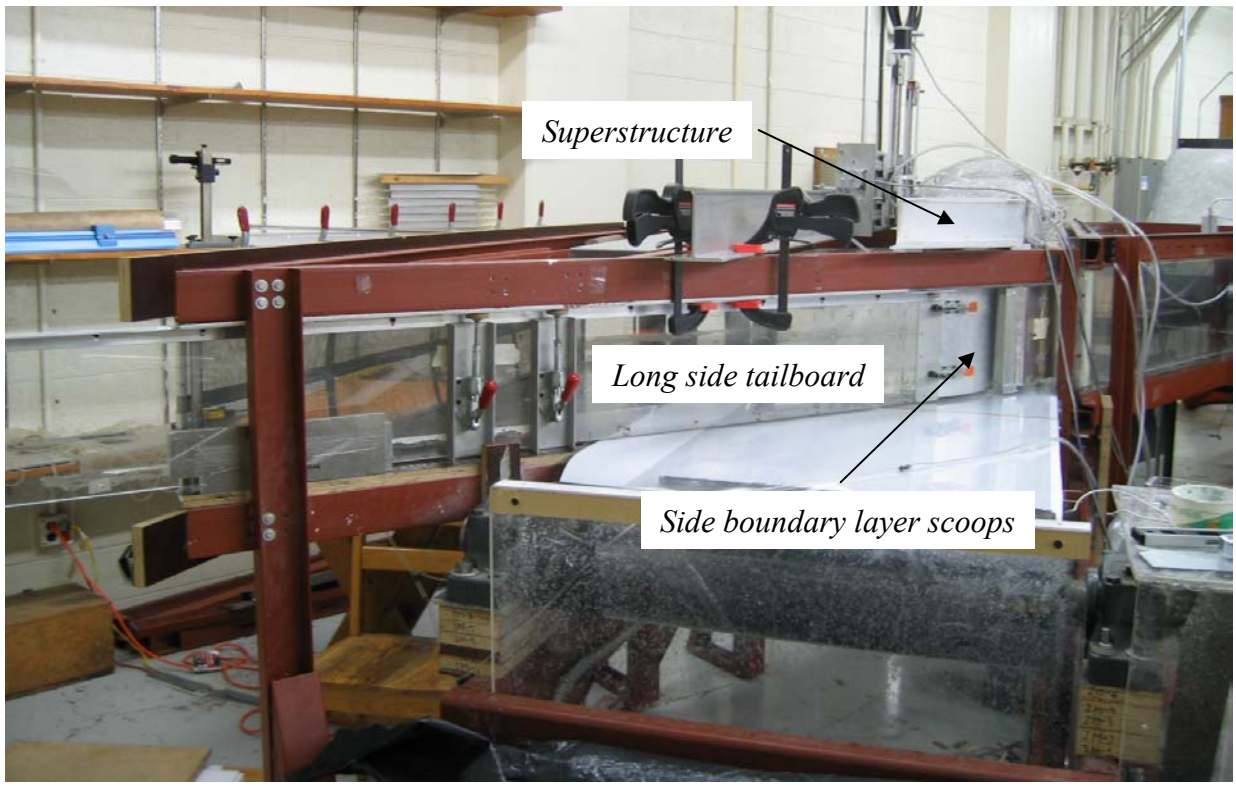

Figure 2-18: Side view of the blade row and downstream test section taken from the long side of the cascade tunnel (view 3 in figure 2-4)

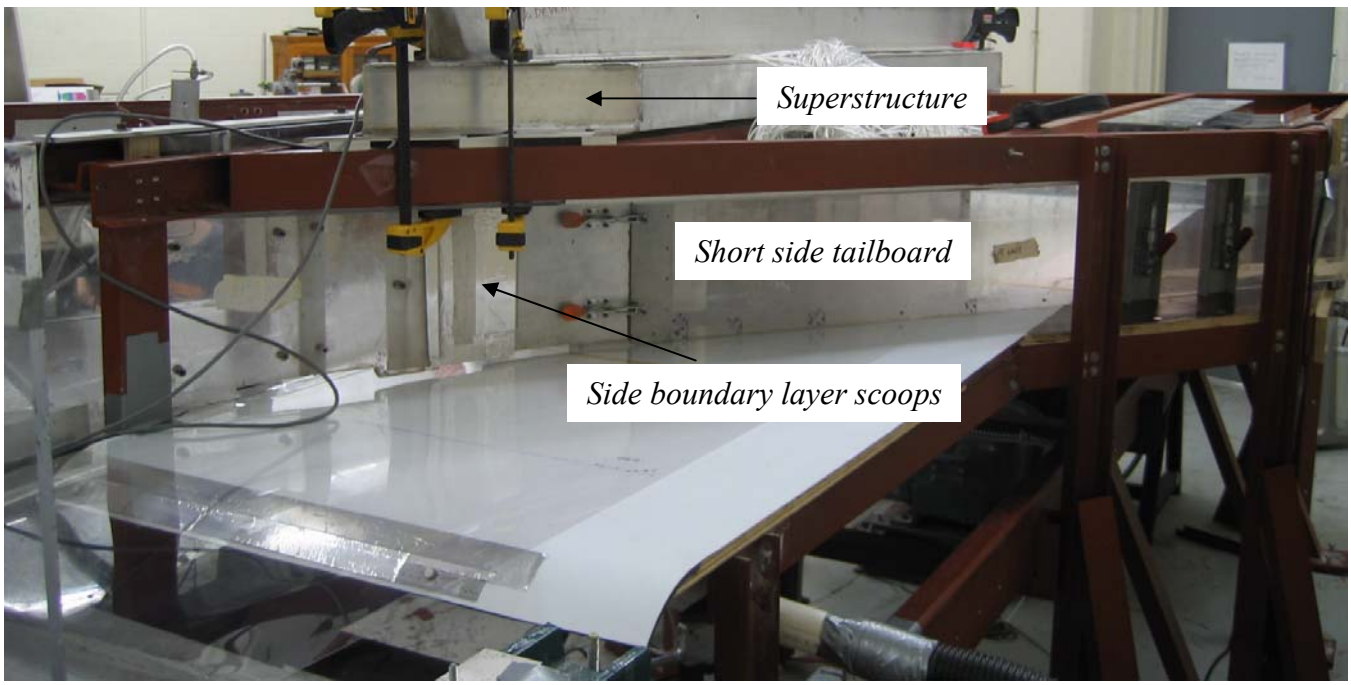

Figure 2-19: Side view of the blade row and downstream test section taken from the short side of the tunnel (view 4 in figure 2-4)

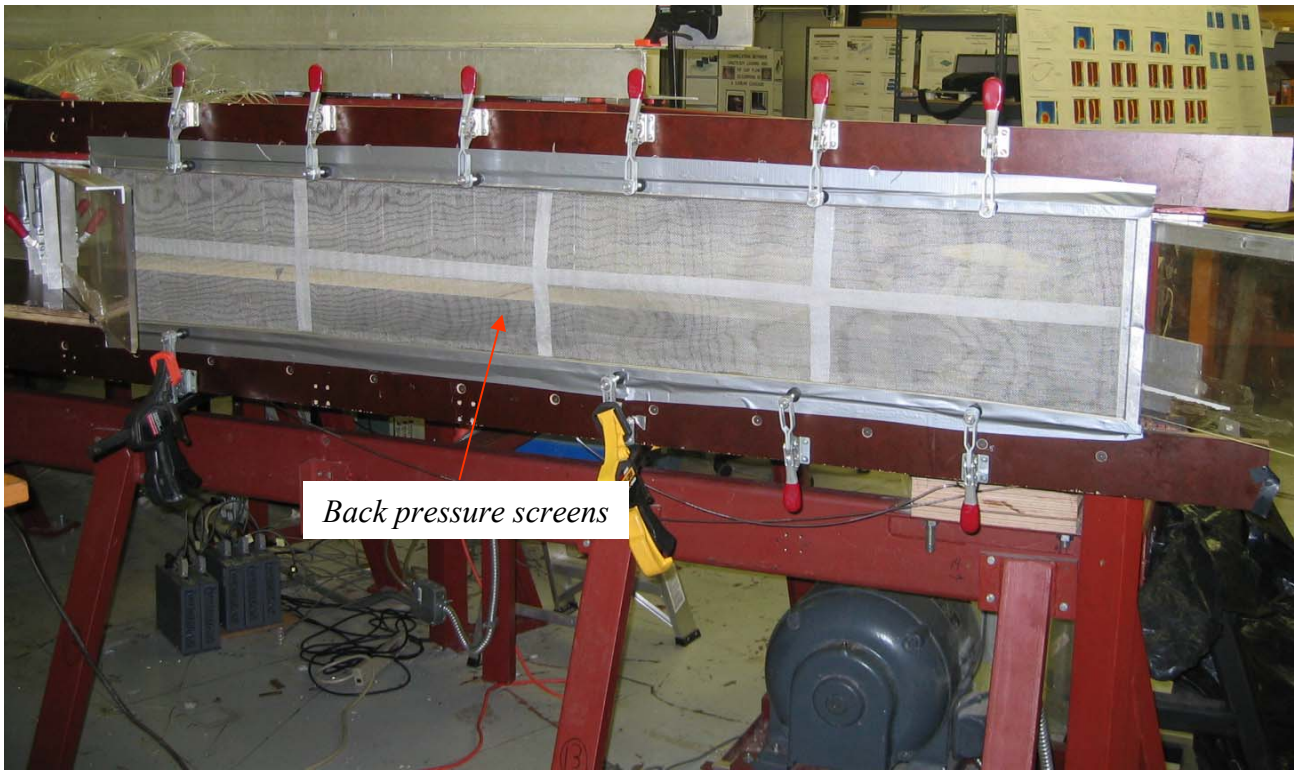

(a)

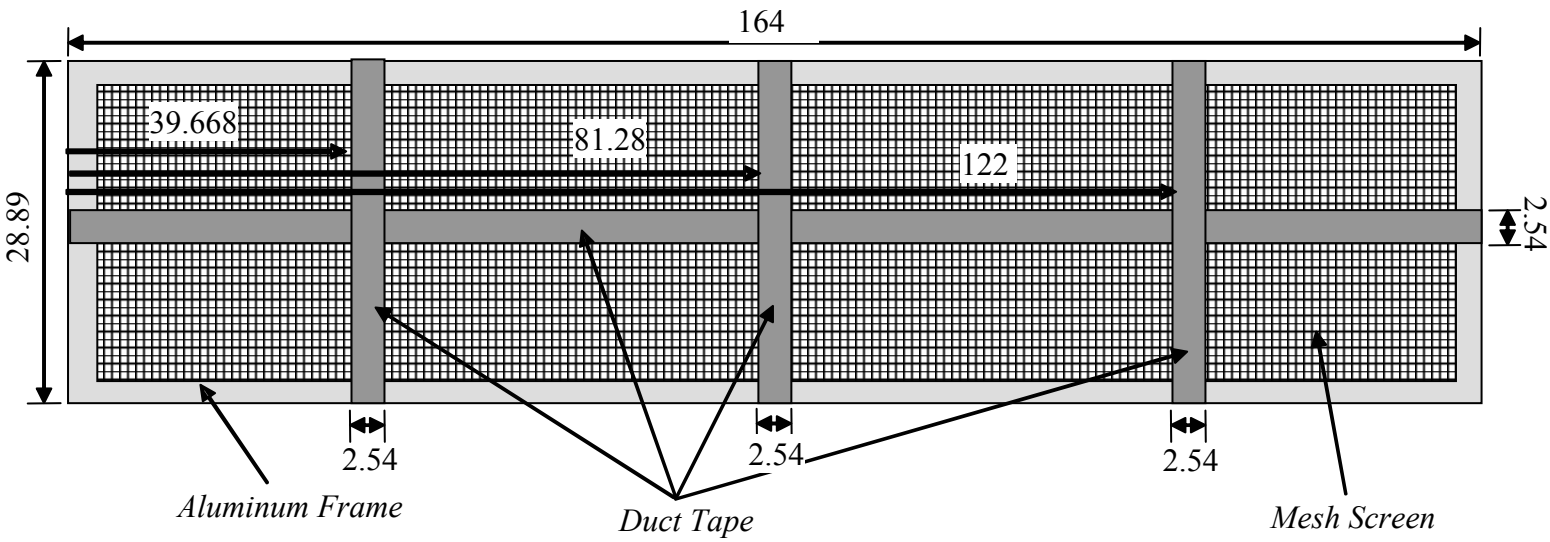

(b)

Figure 2-20: Back pressure screens: **(a)** installed at the exit plane of the tunnel, **(b)** screen diagram with dimensions in cm (view 5 in figure 2-4)

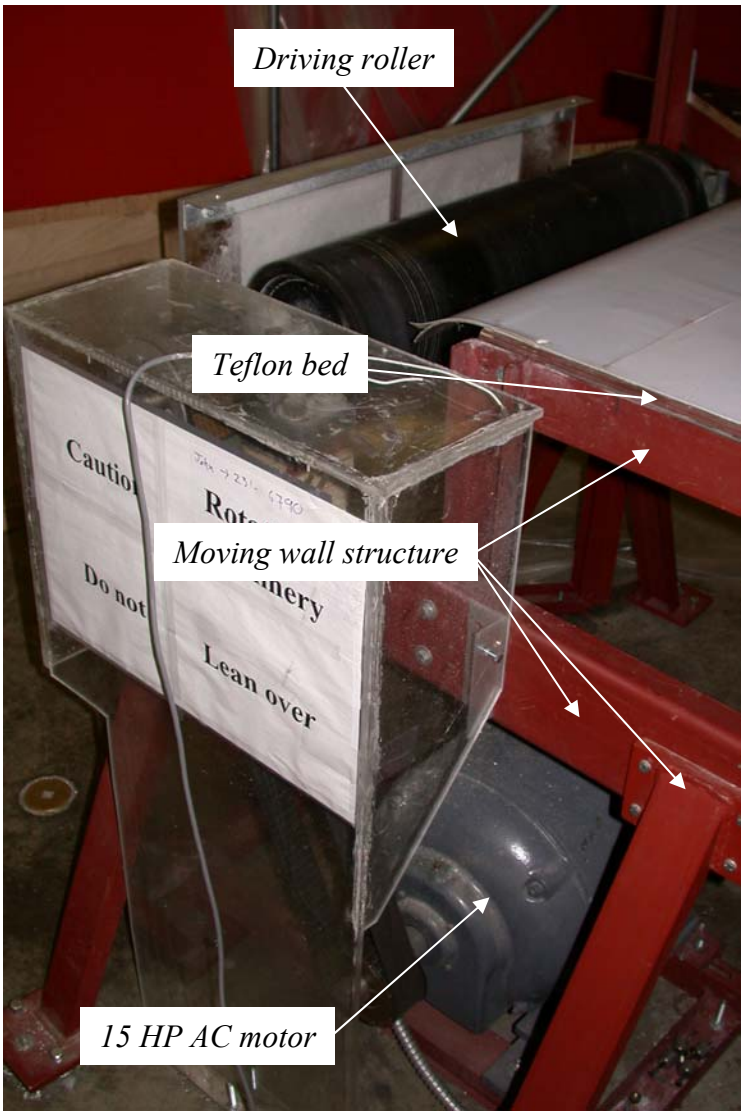

(a)

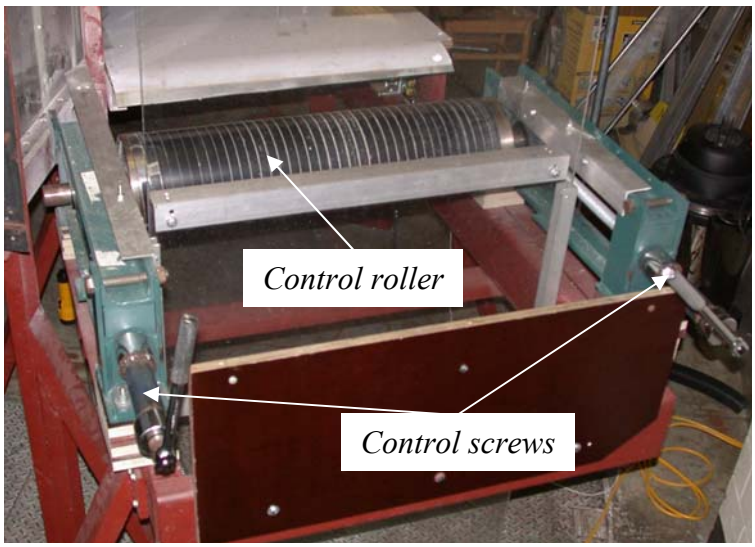

(b)

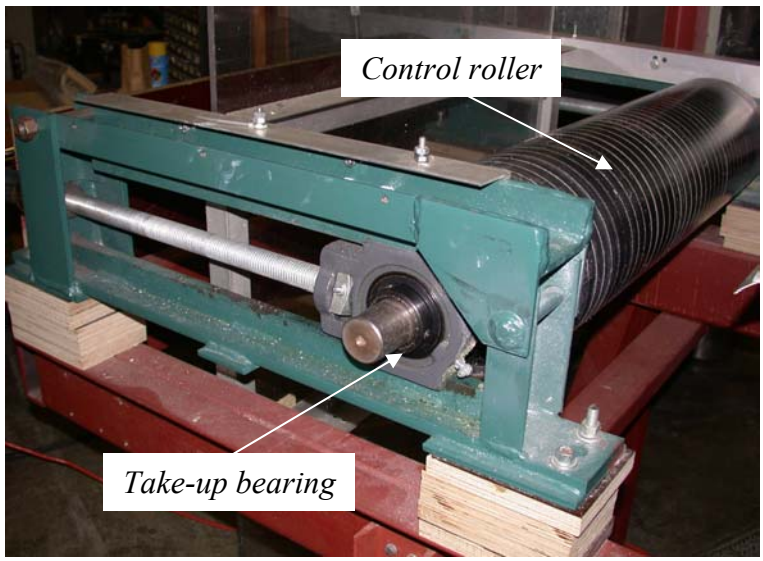

(c)

Figure 2-21: Moving wall system: **(a)** motor used to drive moving wall**, (b)** operator view of the control roller, **(c)** side view of the control roller (Ma (2003)).

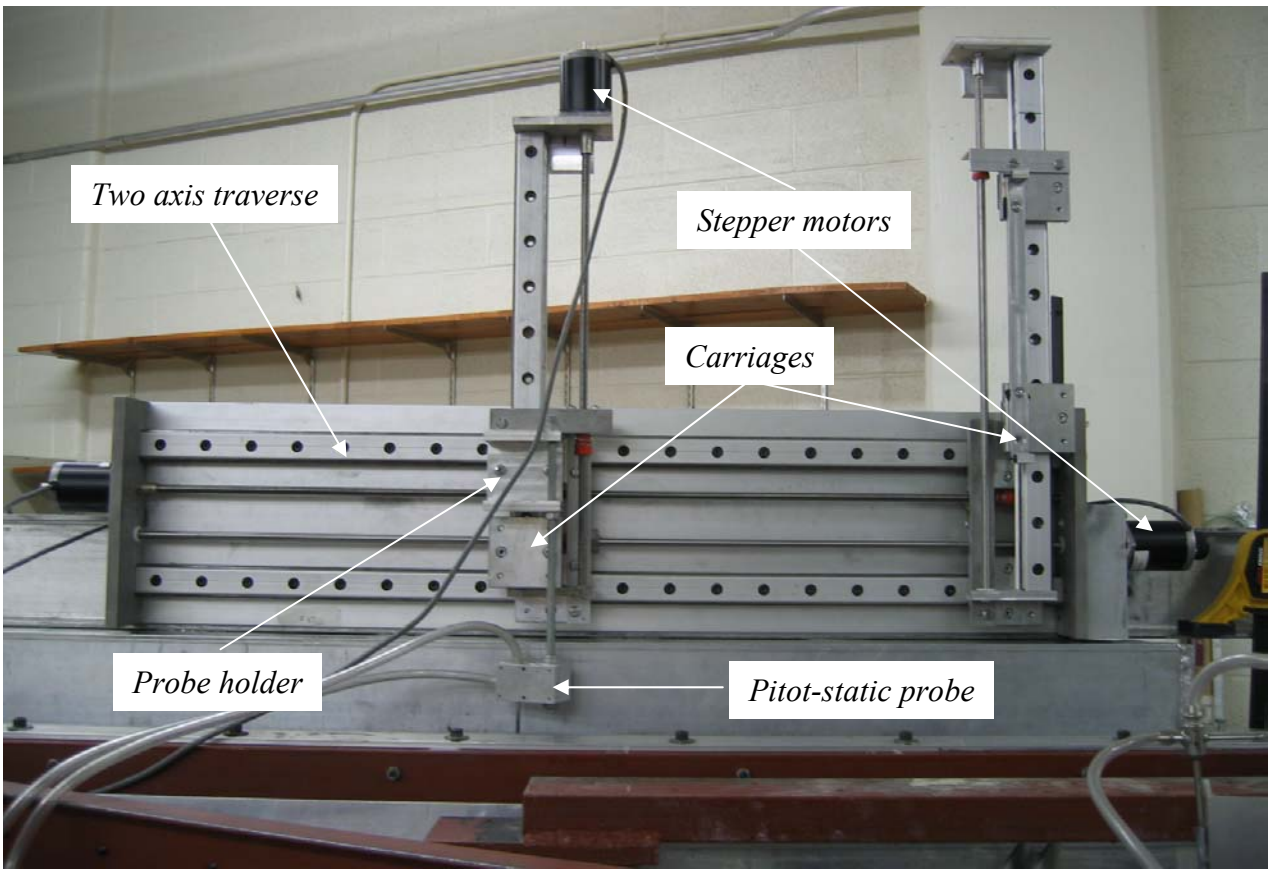

(a)

(b)

Figure 2-22: Two-axis traverse system: **(a)** two axis traverse mounted on the blade row supporting a Pitot-static probe , **(b)** Parker PDX13 single-axis package mini-step.

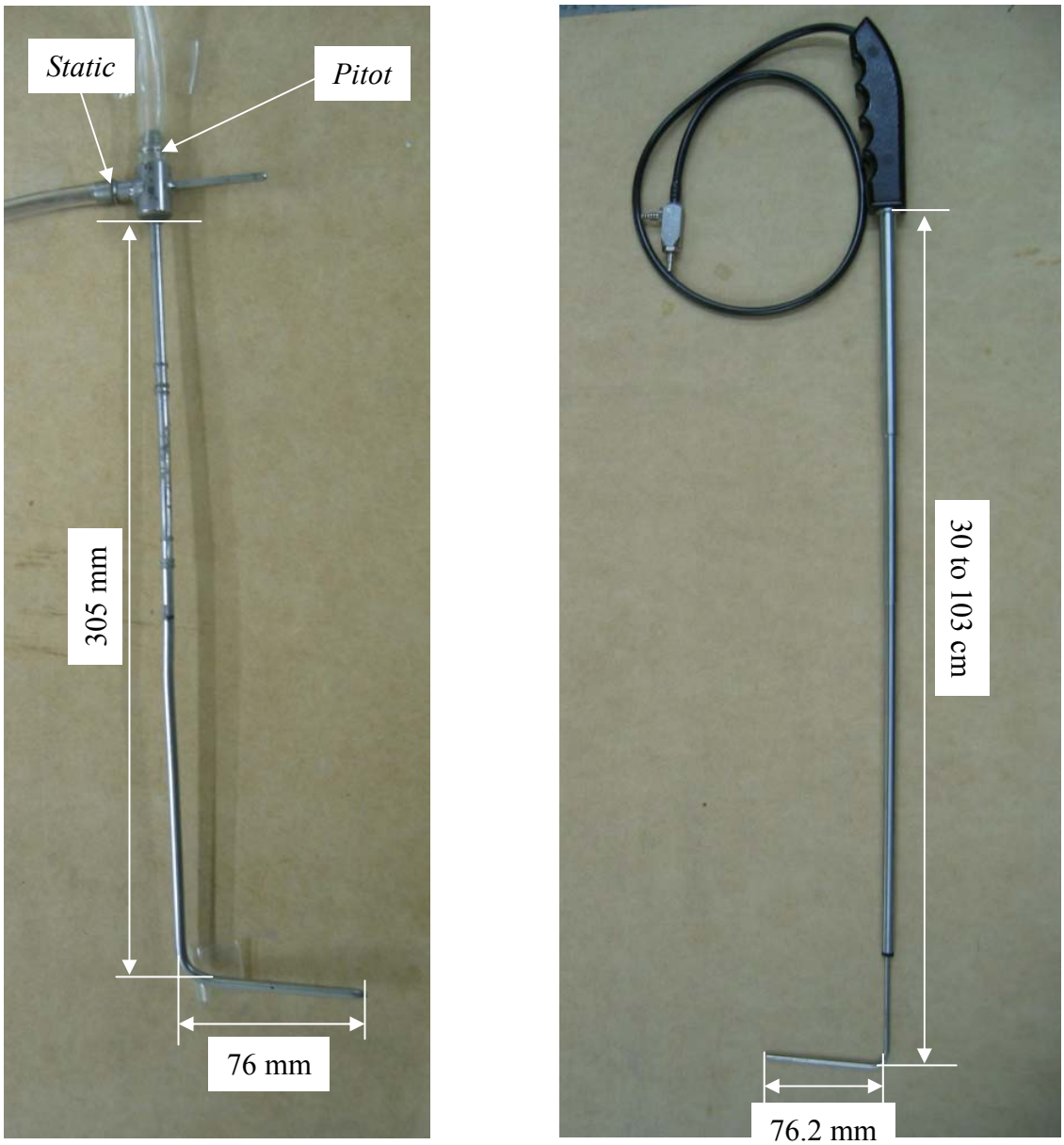

Figure 2-23: Pitot-static probes: **(a)** Dwyer Instruments Standard Model 160 Pitot Probe (Model 167-12) , **(b)** Dwyer Instruments Telescoping Pitot Tube (Model 166T).

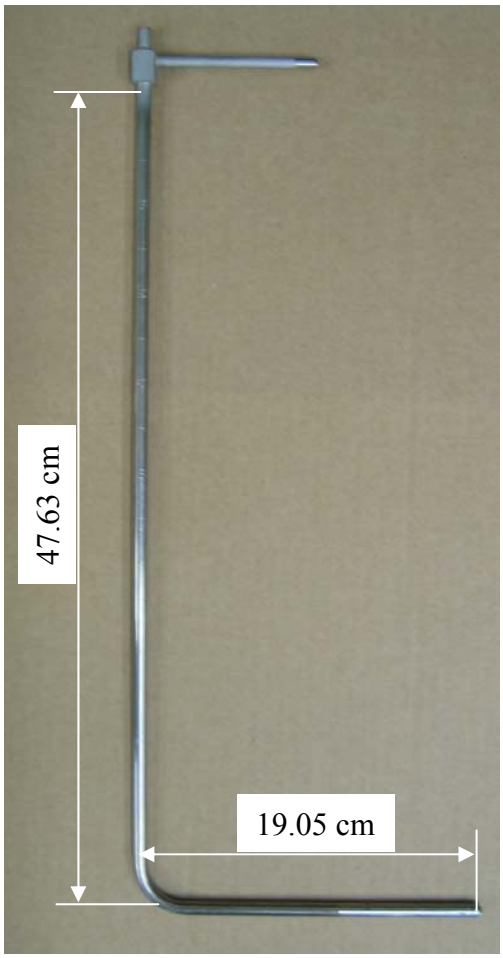

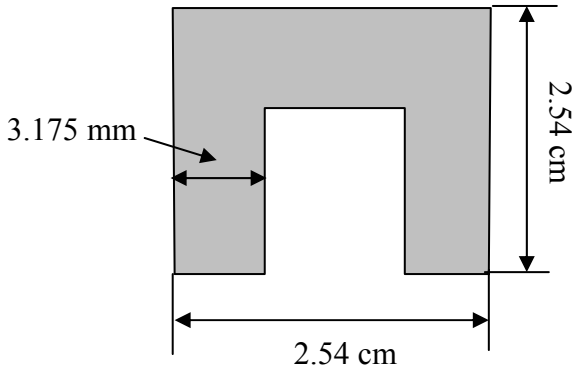

Support beam

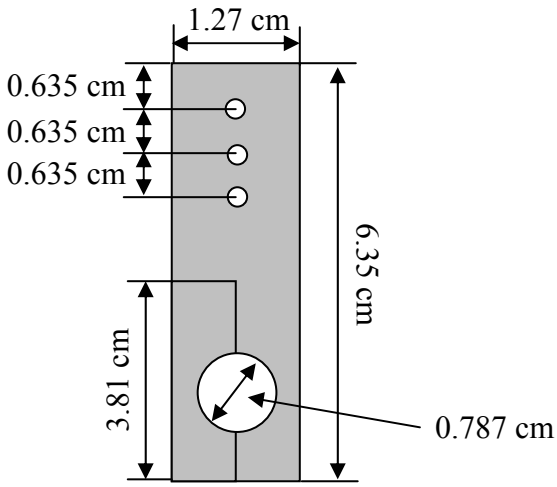

Probe holder

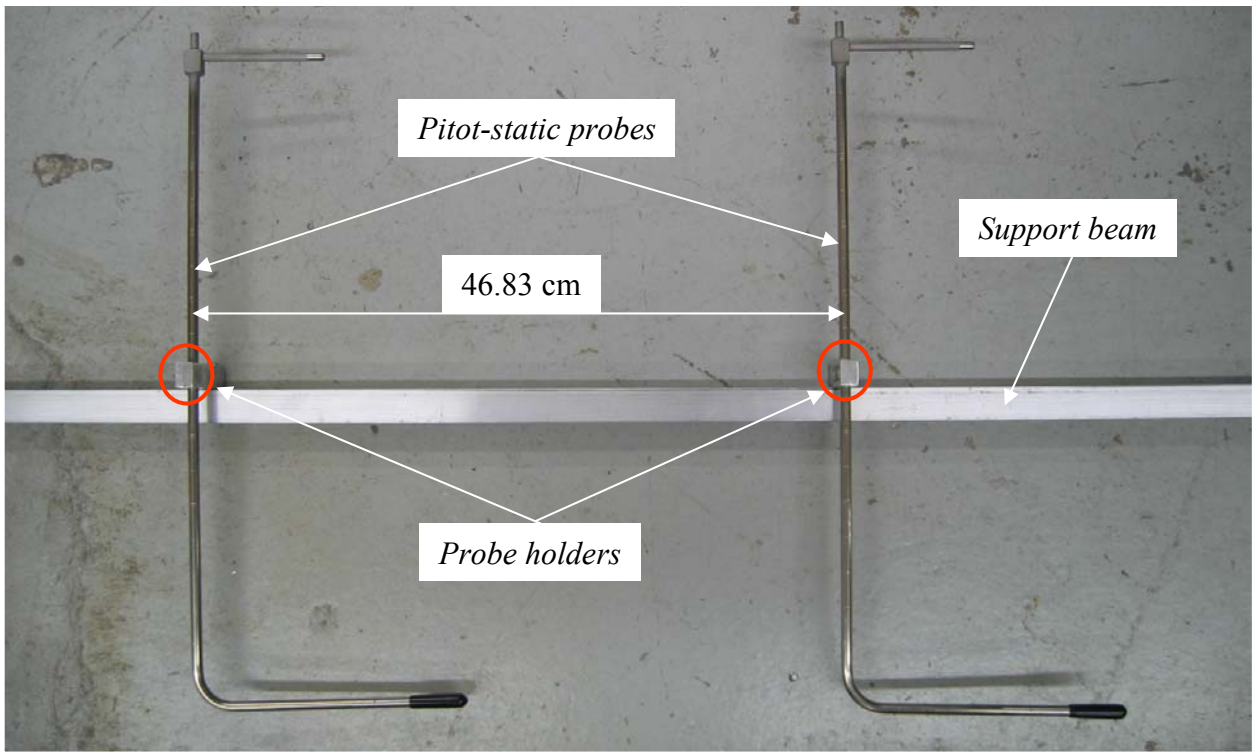

Figure 2-24: Dwyer Instruments Model 160 Pitot Probe (Model 160-18) with probe holders and support beam

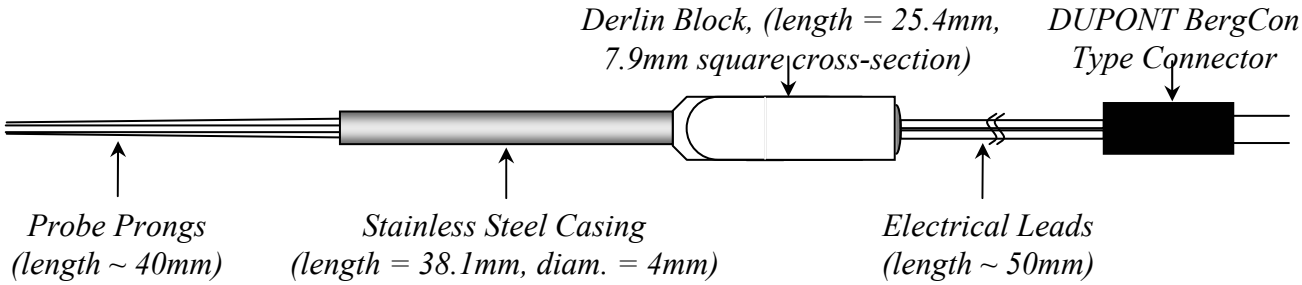

Figure 2-25: Miniature Kovaznay four-sensor hot-wire probe, type AVOP-4-100

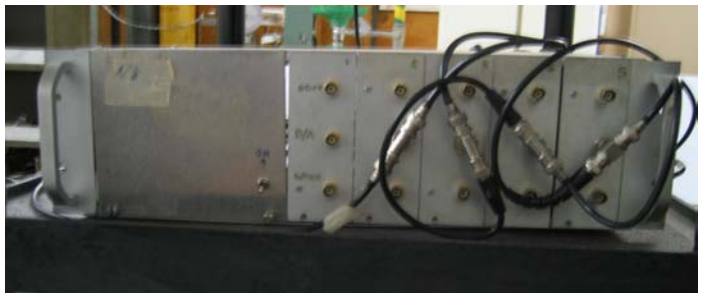

(a) **(b)**

Figure 2-26: Hot-wire anemometry components: **(a)** Dantec 56C17/56C01 constant temperature anemometer unit, **(b)** Four 10- buck-and-gain amplifiers equipped with calibrated RC filters.

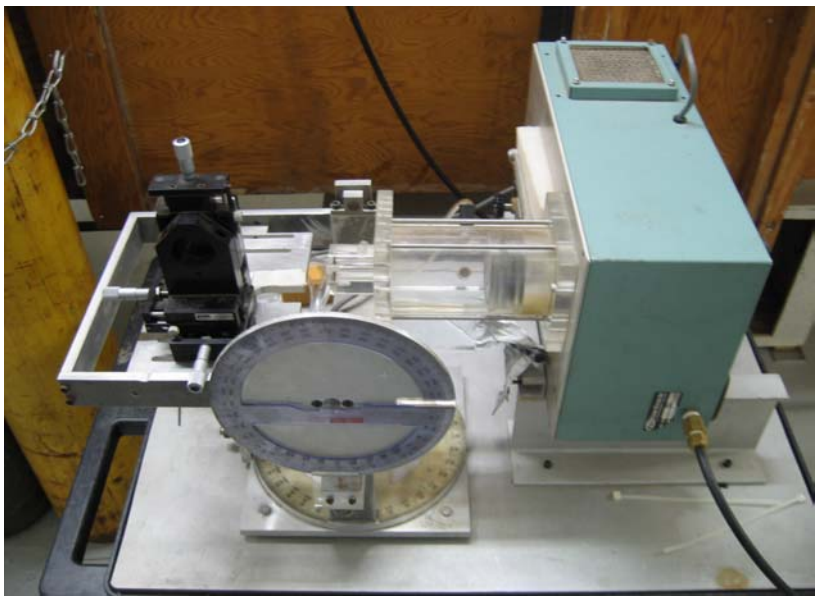

Figure 2-27: TSI velocity and angle calibrator jet

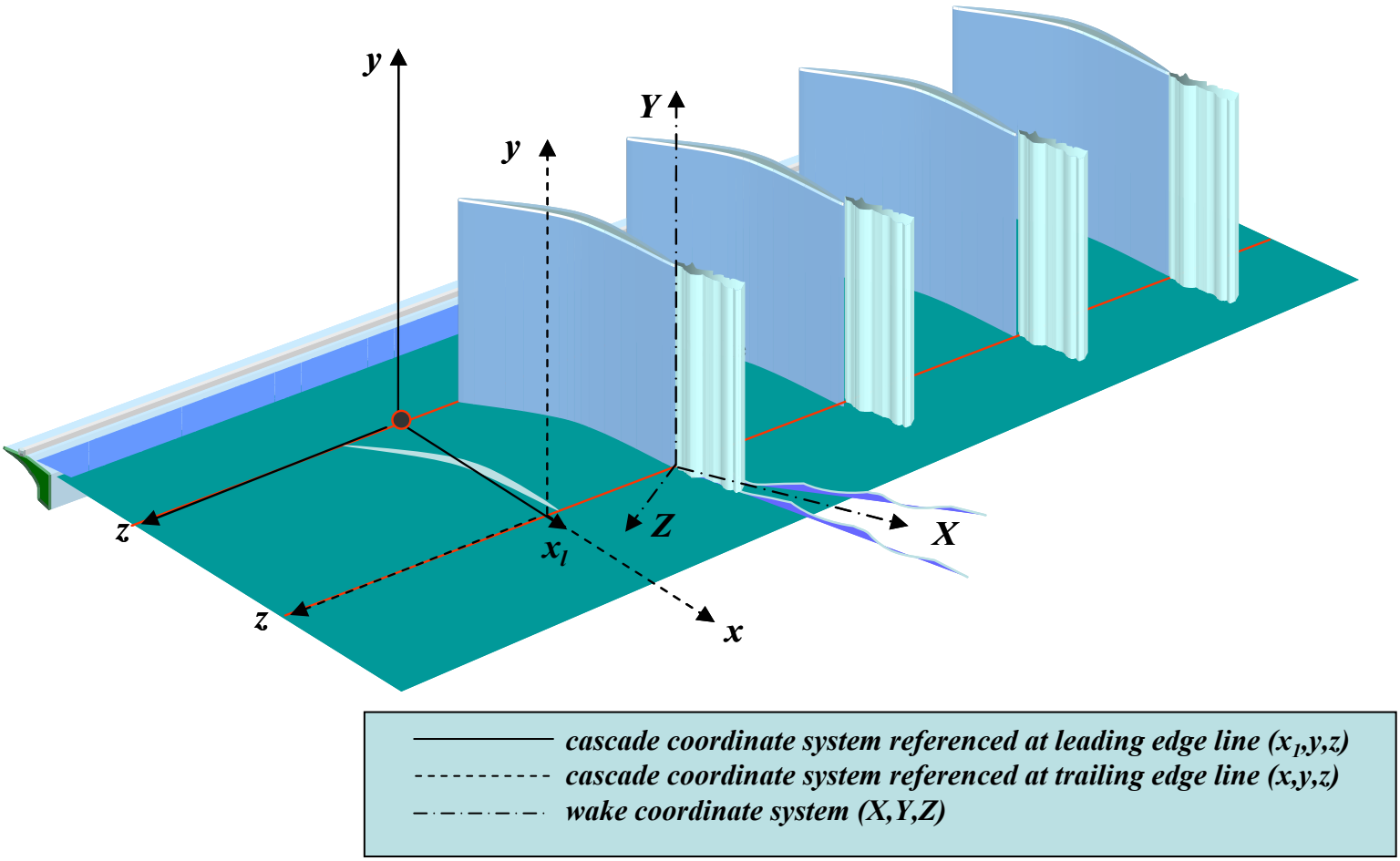

Figure 2-28: The three coordinate systems used in the cascade tunnel.

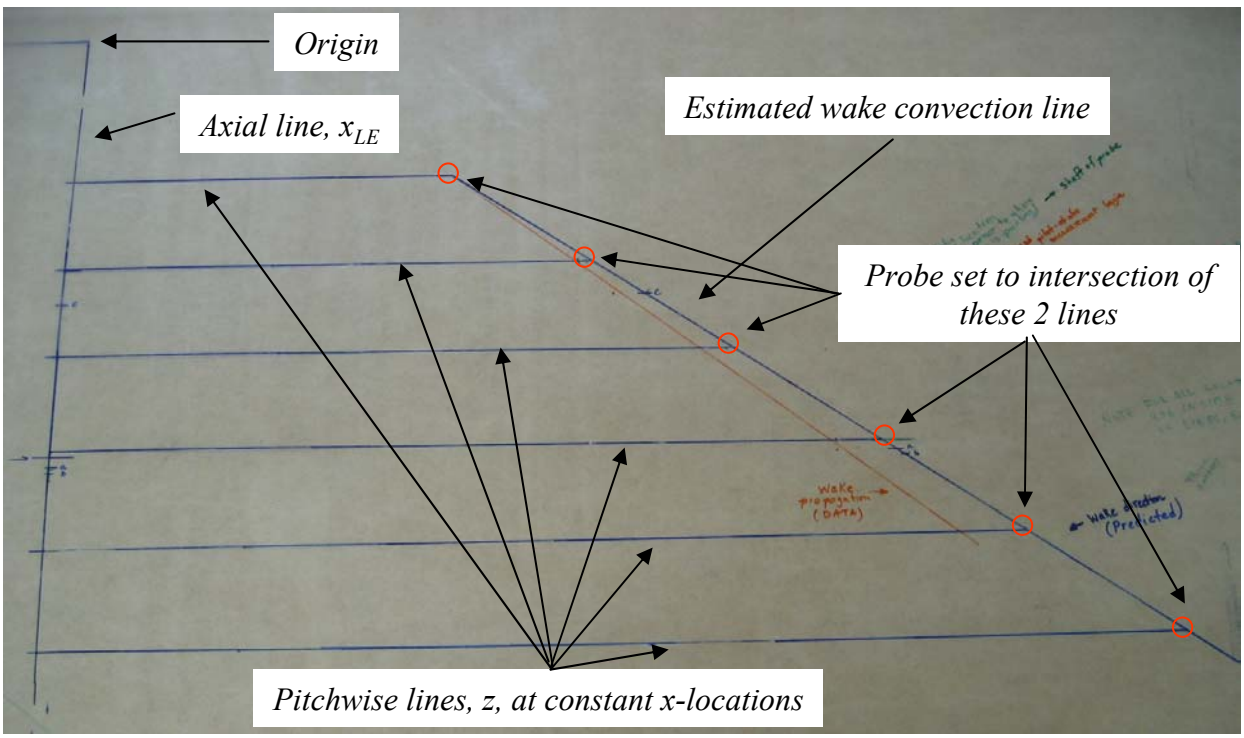

Figure 2-29: Mylar measurement grid used to set the Pitot-static and four sensor hot-wire probes.

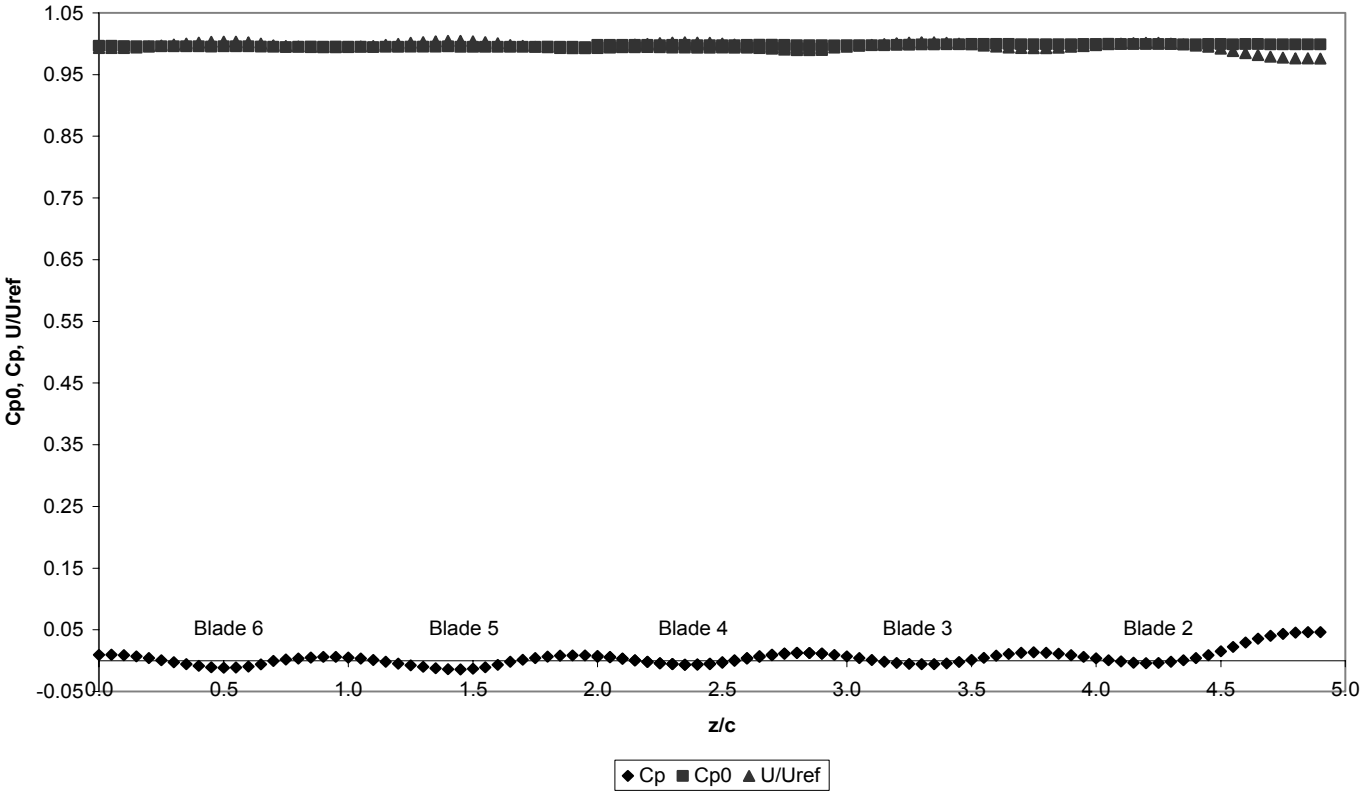

(a)

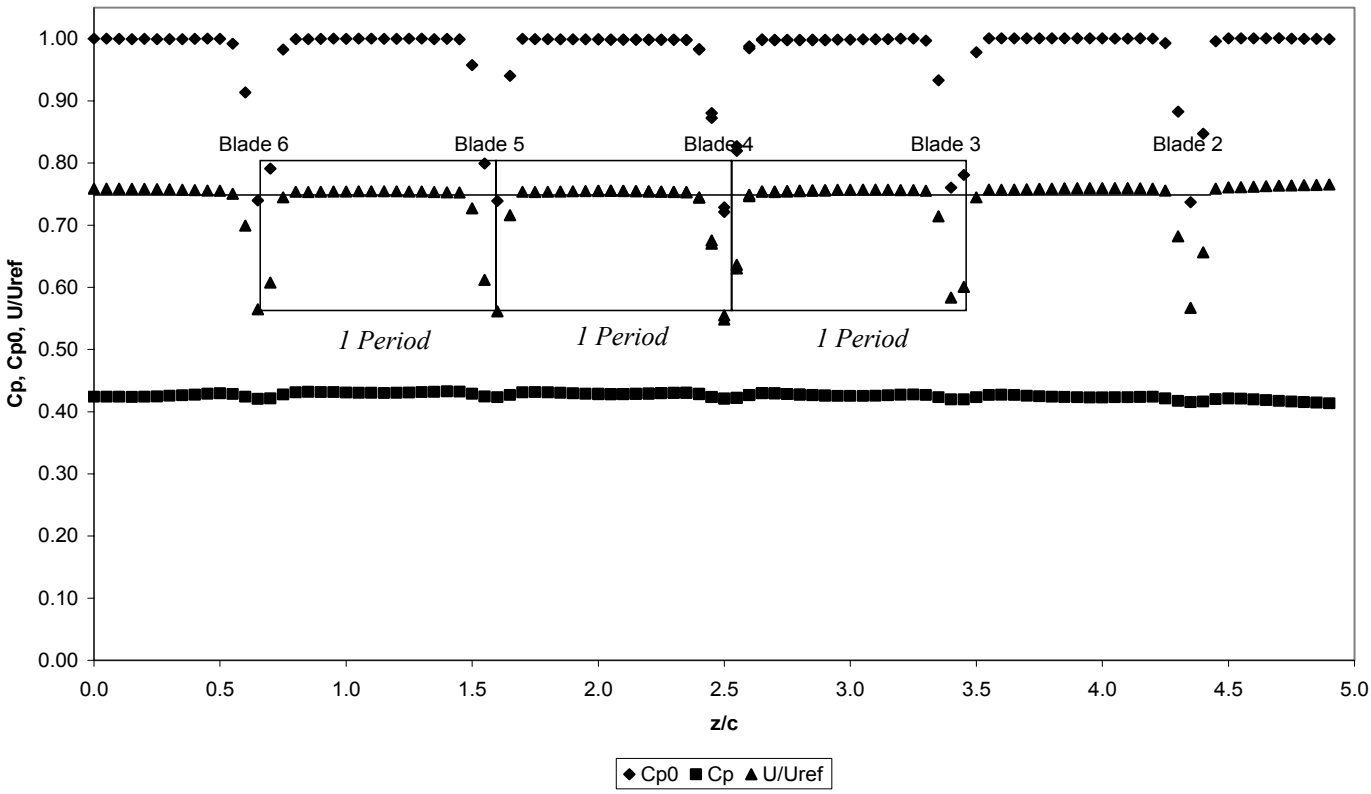

(b)

Figure 2-30: Upstream and downstream pressure measurements: (a) inflow pressure measurement performed at x/c_a = -0.65 and y/c_a = 0.92, (b) downstream pressure measurement performed at x/c_a = 1.79 and y/c_a = 0.92

CHAPTER THREE

3. Analysis of Baseline GE-Rotor-B Blades

3.1 Introduction

The first step to understanding the controlling parameters of the wakes created by the serrated trailing edges is to study the wakes of the baseline GE-Rotor-B blades. This chapter discusses the results and the analysis of the measurements performed on the baseline blades in the Virginia Tech Linear Cascade Tunnel. The wake measurements were performed downstream of the blade row with a tip gap setting of 4.19 mm which is 1.65% of the blade chord, c. Midspan profiles were measured with single-wires and quad-wires at four downstream axial locations each to reveal the wake structure, while cross-sectional measurements were performed at two of the four axial locations to reveal the tip leakage vortex.

Single-sensor hot-wire measurements were performed at the downstream axial locations of x/c_a = 0.002, 0.60, 1.19, and 1.79 where c_a is the axial chord of 139 mm. Four-sensor hot-wire measurements were performed at x/c_a = 0.61, 1.18, 1.82 and 2.38. Cross-sectional measurements were performed with the four-senor hot-wire at two of the axial locations of $0.61c_a$ and $1.82c_a$. Additional cross-sectional measurements were performed with the telescoping Pitot-static probe at x/c_a = 0.84 and 1.88. The measurement locations for the three measurement techniques are depicted in figure 3-1. Also, shown is the wake centerline location (defined as the locus of the minimum streamwsie velocity) at midspan for blade 5 as well as the leading edge and trailing edge coordinate systems defined in section 2-6 and shown in figure 2-28.

Blade loading measurements will be presented first, along with integrated values of circulation and lift. Secondly, cross-sectional measurements of total and static pressure as well as mean velocity measured, with the Pitot-static probe, will be presented. Next, mean velocity and turbulence cross-sectional measurements obtained with the four-sensor hot-wires will be presented. Also discussed will be the two-dimensionality and three-dimensionality of the wake region and the structure of the tip leakage vortex. Next, the wake measurements at the blade mid-span will be presented. These data will be compared to prior plane wake studies and conclusions will be drawn about the wakes shed by the baseline blades. Finally, the entire chapter will be summarized highlighting the important characteristics of the wake.

3.2. Measurement Scheme

Various measurement schemes were used to measure the wakes of the baseline blades. Measurements with the Dwyer Instruments Telescoping Pitot tube were taken over one pitchwise period of the cascade (236 mm) centered on wake of blade 5, at positions from 2.54 mm to 249 mm from the endwall as shown in figure 3-2. Variable step-sizes were used to reduce the number of points used in the passage to add extra points where the velocity gradients were greatest. Step sizes were integer fractions of the blade spacing, and a step size of 11.80 mm was used in the passage while in the wake region the step size was 4.72 mm. In total, this grid contained 1,130 points. At each point 5 record of 1024 samples of the pressure transducer voltage outputs were recorded at a sampling rate of 3200Hz. Successive records were spaced at intervals of 2 seconds.

For the cross-sectional four-sensor hot-wire measurements a different measurement grid was used for the two axial locations. The measurement grid used at x/c_a = 0.61 consisted of 327 points. These points were distributed over pitchwise distance of -494 mm to -199 mm measured from the origin and a spanwise distance of 4 mm to 127 mm measured from the lower endwall. Of the 326 points 233 points were located between 4 mm and 54 mm measured from the lower endwall in the spanwise direction to detail the wake in the near wall region and the structure of the tip leakage vortex. This grid is shown in figure 3-3. At x/c_a = 1.82 the grid was increased slightly in size to

accommodate the larger wake width. The grid size used was 366 points, which were distributed over a pitchwise distance of -732mm to -414 mm measured from origin and over the spanwise distance of 4 mm to 127 mm measured from the lower endwall. This grid is shown in figure 3-4. For both cross-sectional grids, the majority of the points were sampled at a frequency of 3,200 Hz, and contained 30 records each with a record length of 1024. Every fifth point was sampled at 51.2 kHz, and contained 100 records with a record length of 2048. These sampling characteristics were chosen to allow the calculation of spectra. There was no wait time between measurements and anti-aliasing was used.

Wake profile measurements were performed at the midspan location (y/c_a = 0.92) using both single and four-sensor hot-wires. These measurements were each performed at four downstream axial locations. The profile step-size and number of points depended greatly on the axial location. For example at x/c_a = 0.002, 41 points were used over a pitchwise distance of 127 mm, at x/c_a = 0.61, 51 points were used over the pitchwise distance of 76 mm, at x/c_a = 1.18, 60 points were used over the pitchwise distance of 130 mm, at x/c_a = 1.82, 60 points were used over the pitchwise distance of 152 mm and finally at x/c_a = 2.38, 82 points were used over the pitchwise distance of 209 mm. These five profiles mentioned here are shown in figure 3-5. The z-axis in this figure is the local coordinate of the measurement location, where 0 corresponds to the location shown in figure 3-1. The profiles are not centered on the 0 location because when the wakes were measured they were not centered around that point, the profiles were offset to adjust for this. At every measurement point hot-wire sensor signals were sampled at a frequency of 51.2 kHz over 100 records each with a record length of 2048. There was about a 0.5 second delay between the measurement of successive record. Anti-aliasing filters with a roll off at 20kHz was used to eliminate the high frequency noise.

Measurement uncertainties were calculated for 20:1 odds using the Kline and McClintock (1953) method. Table 3-1 below lists the uncertainty for mean velocities, Reynolds stress, turbulence kinetic energy and streamwise vorticity. As stated at the end of chapter 2, the uncertainty in C_p is 1%.

Table 3-1: Measurement uncertainty estimates using the Kline and McClintock (1953) method.

Quantity	***Uncertainty***
$\delta(U, V, W)/U_\infty$	1%
$\delta(\overline{u'^2}, \overline{v'^2}, \overline{w'^2})/U_\infty^2$	3%, 6%, 6%
$\delta(\overline{u'v'}, \overline{v'w'}, \overline{u'w'})/U_\infty^2$	3%
$\delta(k)/k$	4%
$\delta(\Omega_x)/\Omega_x$	2.2%

3.3 Blade Loading

The blade loading of the GE Rotor B blades were measured to define the initial conditions of the downstream wake. Knowing the blade loading, the circulation on the blades can be calculated.

Blade loading was measured for the both the blade with the controlled 1 mm opening near the blade root and for one without by measuring static pressure on the blade surface using the embedded pressure ports at spanwise location of $y/c_a = 0.95$. There are 46 ports located on the surfaces of blades 4 and 5, as was described in chapter 2. Measuring the static pressures P_s on the blade surface, the coefficient of pressure, $C_{p,s}$ can be calculated:

$$C_{p,s} = \frac{P_s - P_\infty}{P_{o\infty} - P_\infty} \tag{3-1}$$

where P_∞ is the freestream velocity and $P_{o,\infty}$ is the total freestream pressure The blade loading, $C_{p,s}$, is plotted versus the axial distance from the leading edge, x_1/c_a (defined in figure 3-1 above and in figure 2-28) in figure 3-6.

Near the leading edge of the blade in figure 3-6, at approximately $x_1/c_a = 0.05$, the fluctuations in the level of the blade loading for both plots on both the pressure and suction sides are due to the trip strips. Over almost the first quarter of the blade axial chord on the suction side, a favorable pressure gradient is present. The minimum pressure is found on the suction side of the blade at $x_1/c_a = 0.22$ with a $C_{p,s} = -0.2$ for both plots. After reaching this minimum point, an adverse pressure gradient is present over the remaining three quarters of the axial chord. The maximum pressure on the suction side is

reached near trailing edge with a $C_{p,s}$ = 0.30. On the pressure side the two plots deviate after x_1/c_a = 0.1 which is after the boundary layer trip strip. For both plots, the pressure steadily increases until it reaches a maximum at x_1/c_a = 0.70, with a maximum $C_{p,s}$ = 0.40 for the controlled 1 mm blade root opening and $C_{p,s}$ = 0.49 for the non-controlled blade rooting opening. Between this point and the trailing edge, the pressure drops for both plots most likely due to the acceleration of the flow to match the pressure on the suction side of the blade near the trailing edge.

The normalized edge velocity just outside the blade boundary as a fraction of the free stream velocity can be estimated by using Bernoulli's equation:

$$\frac{U}{U_\infty} = \sqrt{1 - C_p} \tag{3-2}$$

This velocity can be used to calculate the circulation around the blade:

$$\Gamma = \oint U \bullet ds \tag{3-3}$$

where the U is the local surface velocity and ds is an elemental blade surface length. Using equation (3-3) the circulation for the baseline blades with the uncontrolled blade root opening was determined to be $0.47 U_\infty c_a$, which agrees with circulation calculated by Muthanna (2002), while the 1 mm opening at the blade root cover had a circulation of $0.45 U_\infty c_a$. This is a variation of approximately 4.3% between the two runs. Subsequent measurements were only made with the controlled root opening.

3.4 Pitot-Static Cross-Sectional Measurements

Figure 3-7 shows the Pitot-static measurement at x/c_a = 0.84 while figure 3-8 shows the Pitot-static measurement at x/c_a = 1.88. In both of these figures the total pressure, $C_{p,o}$, static pressure, C_p, and the normalized velocity, U/U_∞, are plotted as a function of the pitchwise coordinate, z/c_a (refer to equations 2-1 through 2-3 for calculating these variables). Plotted in each of these figures are the locations of the mid-span measurements described in the latter sections of this chapter.

In figure 3-7(a), the total pressure remains constant outside of the wake region with a value of approximately 1. The wake of blade 5 is revealed by the vertical region of

lowered pressures towards the center of the figure. The wake centerline – the line of lowest streamwise velocity and stagnation pressure coefficient is not straight but bowed slightly, presumably, by the velocities induced on the wake by the vorticity at the two endwalls. The wake thickness, measured from the wake centerline appears slightly greater on the suction (right hand) side of the wake, especially near the upper endwall The boundary layer on the upper endwall is thickest to the suction side of the wake (about $0.18c_a$) and much thinner near the pressure side. The minimum thickness reached at z/c_a = -3.25 is about $0.082c_a$, this is two times thinner than the suction side boundary layer, and only about one-fifth thickness of the wake itself. On the lower endwall, the leakage vortex region, shed from blade 4, is clearly visible, through the large oval shaped region of velocity defect it produces on the pressure side of the wake of blade 5. From the plot, the vortex center, identified as the location of largest defect, is located at approximately z/c_a = -2.85 and y/c_a = 0.18. The outer edge of the vortex region extends to approximately y/c_a = 0.45. In figure 3-7(b) the normalized streamwise velocity, U/U_∞, is plotted and this plot shows the same wake features found in figure 3-7(a). The streamwise velocity in the free-stream is $0.76U_\infty$ and the lowest velocity is found in the vortex center, with a velocity of approximately $0.35U_\infty$. The velocity in the wake center is approximately $0.56U_\infty$.

At x/c_a = 1.88 it can be seen that wake has spread as shown in the total pressure plot in figure 3-8(a) and the velocity in the wake center has increased as can be seen in the normalized velocity plot of figure 3-8(b). In figure 3-8(a), the total pressure is plotted and it has similar flow-field structure as x/c_a = 0.84 where the wake and vortex regions are clearly visible. The wake centerline is also not straight here but bowed slightly to the suction side of the wake. Also, the wake appears to be thicker on the suction side compared to the pressure side. The wake also seems to have the same type of characteristics near the upper endwall as at x/c_a = 0.84. The maximum thickness of the upper boundary layer is found to on the suction side and is the same as the x/c_a = 0.84 which is about $0.18c_a$. The minimum thickness is found at z/c_a = -4.5 and it is also the same as at x/c_a = 0.84 with a value of $0.082c_a$. At the lower endwall, the tip leakage vortex of blade 4 is still clearly visible. The vortex is centered at approximately z/c_a = -4.35 and y/c_a = 0.2 and the outer edge of the vortex region increases over the x/c_a = 0.84

to y/c_a = 0.6. The normalized velocity plot in figure 3-8(b) shows the same wake characteristics as the total pressure plot in figure 3-8(a). The free-stream velocity is once again $0.76U_\infty$ and the minimum velocity is found in the vortex center with a value of $0.51U_\infty$ which is 1.45 times faster than the velocity in the vortex center at x/c_a = 0.84. The minimum velocity in the wake is approximately $0.6U_\infty$ which is only slightly faster than at x/c_a = 0.84.

3.5 Fundamentals of Turbulent Wake Measurements

The single-wire and quad-wire anemometer systems measure the mean velocity and their fluctuations in the fluid medium in which they are placed. In general, the fluid velocity field can be decomposed into the mean velocity and the fluctuation by using Reynolds decomposition which is defined as:

$$U(x,t) = \overline{U(x,t)} + u(x,t) \tag{3-4}$$

where $U(x,t)$ is the velocity, $\overline{U(x,t)}$ is the mean velocity and $u(x,t)$ is the fluctuating term. When the mean of the momentum equation using Reynolds decomposition is taken, the mean of the non-linear term $\overline{U_i U_j}$ will become:

$$\overline{U_i U_j} = \overline{U_i}\,\overline{U_j} + \overline{u'_i\, u'_j} \tag{3-5}$$

where $\overline{u'_i\, u'_j}$ is known as the Reynolds stress. The Reynolds stresses can be written in matrix form as:

$$\begin{bmatrix} \overline{u'u'} & \overline{u'v'} & \overline{u'w'} \\ \overline{v'u'} & \overline{v'v'} & \overline{v'w'} \\ \overline{w'u'} & \overline{w'v'} & \overline{w'w'} \end{bmatrix} \tag{3-6}$$

where the diagonal terms are known as the normal stress terms and the off-diagonal terms are the shear stress terms. The Reynolds stresses are symmetric where $\overline{u'_i\, u'_j} = \overline{u'_j\, u'_i}$. These stresses define the fluctuations in the velocity field where the fluctuations define the turbulent flow field. This derivation is the fundamental underlying of the turbulent wake measurements performed in this experiment.

3.5.1 Rotation Technique for Quad-Wire Measurements

The three component velocity, the Reynolds stresses, the turbulence triple-products and spectral data obtained from the experiment are in an unrotated state. By unrotated this means the data has been not rotated to accommodate for the small probe angles that may arise through the set-up process. To set the probe in the tunnel, it was necessary to predict the direction of the wake propagation prior to taking any data. The wake was assumed to travel parallel to the end walls. By predicting the propagation of the wake, it is possible to approximately align the probe with flow direction thus reducing the angle between the probe and the flow direction. Even though the probe is aligned with the approximate wake propagation, variation in the angle of the probe may occur when the probe is actually mounted in the probe support in the tunnel.

To rotate the three component velocity, Reynolds stresses, turbulence triple-product and spectral data obtained from the measurements Euler angles were used. Pitch and yaw angles were determined by assuming that streamlines outside the midspan of the blade were aligned with the mainstream while for the midspan profile measurements the roll angle was determined by examining the distribution of the residual $\overline{v'w'}$ stress. Table 3-2 lists the Euler angles used to rotate the data obtained by the four-sensor hot-wires.

Table 3-2: Values of Euler angles used to rotate four-sensor hot-wire data

Location (x/c_a)	***Measurement***	θ_x	θ_y	θ_z
0.61	Mid-Span	3.00	-4.11	-0.81
0.61	Cross-Section	0	-1.28	-6.60
1.18	Mid-Span	-1.00	-2.41	-1.36
1.82	Mid-Span	0.50	-1.90	-1.27
1.82	Cross-Section	0	-2.29	-3.40
2.38	Mid-Span	8.00	-2.03	-3.09

3.6 Cross-Sectional Measurements

Cross-sectional measurements were performed to determine the three-dimensionality of the flow-field, which includes the mean velocity and the turbulence properties, from the lower end-wall to the mid-span of the blade. From the Pitot-static

cross-sections, the flow field was shown to be quite three-dimensional near the lower end-wall but since the Pitot-static measurements can only measure the streamwise component of the flow-field, these measurements were performed to obtain the other two components. The mean velocity and turbulence properties are described in the following sections.

3.6.1 Mean Velocity

Figure 3-9 shows plots of the normalized streamwise velocity, U/U_∞, as a function of spanwise, y/c_a, and pitchwise, z/c_a, coordinates at the downstream axial locations of x/c_a = 0.608 and x/c_a = 1.82. The wakes of blades 4 and 5 identified by the vertical regions of lowered velocity (blade 4 wake located at the edge of plot) and the circular region near the lower endwall representing the tip leakage vortex of blade 4 are visible. The minimum streamwise velocity in the cross-section is found near the vortex center at x/c_a = 0.61 and x/c_a = 1.82 and they are $0.33U_\infty$ and $0.48U_\infty$, respectively, which are similar to the values in the Pitot-static cross-sections. Other similarities seen with the Pitot-static cross-sections are in how the wakes spread as they propagate downstream, the radius of the vortex increases in size and the flow field outside of the vortex and wake regions is uniform with a value of about $0.74U_\infty$. In these plots it is possible to see the periodic behavior of the wakes in the pitchwise direction. One period in these plots is indicated by a dashed line and it can be seen the flow is periodic all throughout the flow-field and not only at spanwise location of y/c_a = 0.92.

The effects of the tip leakage vortex on the velocity field can be seen in figure 3-10. In this plot the velocity vector field in the *y-z* plane is plotted. On the y-axis is the spanwise coordinate, y/c_a, and on the horizontal-axis is the pitchwise coordinate, z/c_a. At the axial location of x/c_a = 0.61, shown in figure 3-10(a), the tip leakage vortex is clockwise rotating (positive). It has the highest velocities near the lower end wall and on the side closest to blade 5. At approximately z/c_a = -2.9 and above y/c_a = 0.3, the vectors are acting in the positive spanwise direction creating a line. To the left of this line the flow is being pulled into the tip leakage vortex of blade 4 and to the right it is being pulled into the tip leakage vortex of blade 5 (not shown). This most likely creates a weak

counter-clockwsie rotating vortex located directly above the endwall and at the pitchwise location of z/c_a = -3.0. At the axial location of x/c_a = 1.82, the tip leakage vortex area has spread, and the magnitude of the velocites have decreased throughout the cross-section. Once again the region of vertical velocity can be seen at z/c_a = -4.6 and a possible region of negative vorticity can be seen centered at z/c_a = -4.9. In both cases, the velocity vectors near the midspan station (y/c_a=*0.91*) have a magnitude of no more than $0.024U_\infty$, which is negligible compared to the rest of the flow field. Therefore, the wake at the midspan is almost two-dimensional even with a three-dimensional flow field created by the tip leakage vortex.

The streamwise vorticity for the cross-sectional measurements was calculated. The streamwise vorticity was determined by

$$\Omega_x = \frac{\partial W}{\partial Y} - \frac{\partial V}{\partial Z} \tag{3-7}$$

where Ω_x is the streamwise vorticity. The derivates $\frac{\partial W}{\partial Y}$ and $\frac{\partial V}{\partial Z}$ were calculated by using a finite difference calculation based on a grid of interpolated points, and by assuming streamwise derivatives to be negligible. Figures 3-11(a) and (b) are contour plots of the normalized streamwise vorticity at the axial locations of x/c_a = 0.61 and 1.82. On the *y*-axis is the spanwise coordinate, y/c_a, and on the *x*-axis is the pitchwise coordinate z/c_a, while the contours represent different levels of normalized vorticity, $\Omega_x c_a / U_\infty$. In the cross-sections, the streamwise vorticity is primarily limited to the vortex region of the flow field and is positive. The peak streamwise vorticitiy at x/c_a = 0.61 and 1.819 are given in table 3-3 and the locations are indicated in plots in figure 3-11 by a white cross. The vorticity remains centered at the same spanwise coordinate and the strength decays as the vortex travels downstream. The peak streamwise vorticity at x/c_a = 1.82 is 58% less than at x/c_a = 0.61. At x/c_a = 0.61, near the lower endwall regions of negative vorticity that is 64% of the strength of the main vortex can be seen. These regions are in the vicinity of the negative rotation hypothesized in figure 3-10(a). At x/c_a = 1.82 the negative vorticity regions do not appear at the same location as those smaller negative vortices in figure 3-10(b). In the wake at x/c_a = 0.61 there is negative vorticity on the

order of -0.66U_∞/c_a at z/c_a = -3.0 and y/c_a = 0.12 but this all but this is 56% less at x/c_a = 1.82.

Table 3-3: Streamwise vorticity strength and location of the tip leak vortex and secondary vortex

Tip Leak Vortex

x/c_a	y/c_a	z/c_a	$\Omega_x c_a/U_\infty$
0.61	0.12	-2.57	1.85
1.82	0.12	-4.28	0.77

Secondary Vortex

x/c_a	y/c_a	z/c_a	$\Omega_x c_a/U_\infty$
0.61	0.12	-3.0	-0.66
1.82	0.12	-4.28	-0.29

3.6.2 Turbulence Properties

Plotted in figure 3-12 are the Reynolds stress contours of $\overline{u'^2}$, $\overline{v'^2}$ and $\overline{w'^2}$ as function of the spanwise, y/c_a, and pitchwise, z/c_a, coordinates at the downstream axial locations of 0.61c_a and 1.82c_a. At the both location, the turbulence levels are greatest in the vortex for all three velocity components. For the turbulence stress $\overline{u'^2}$ at x/c_a = 0.61, the region of maximum turbulence forms a semi-circular shape with the highest levels along the vertical line at z/c_a = -2.9 and extends to about 0.3c_a from the lower endwall. This is the line were the flow field is being influenced be tip leakage vortex of either blade 4 or blade 5. The other half of this region of high $\overline{u'^2}$ is centered on y/c_a = 0.30 and extends from about z/c_a = -2.25 to -2.9. The streamwise turbulence levels in this region are approximately 0.009U_∞^2. The turbulence stress, $\overline{v'^2}$, figure 3-12(b), has the highest level centered around the point z/c_a = -2.75 and y/c_a = 0.30, corresponding to the region above the vortex center and has a maximum value of approximately 0.0072U_∞^2. In figure 3-12(c), the cross-wake turbulence stress $\overline{w'^2}$ is greatest along the line where the flow is being influenced by either tip leakage of blade 4 or 5 and has a maximum value of approximately 0.009U_∞^2. At x/c_a = 1.82 a visible decay in all of the turbulence stresses can be seen and the location of the maximum levels has also shifted. The peak turbulence

stress $\overline{u'^2}$ is now located at the upper outer edge of the vortex region at z/c_a = -4.1 and y/c_a = 0.35. For $\overline{v'^2}$, it is now located in the center of the vortex and for $\overline{w'^2}$ it is to the left of the vortex center at z/c_a = -.4.0.

In the wake, the turbulence levels $\overline{u'^2}$ and $\overline{v'^2}$ are much lower than those found in vortex, but the levels of $\overline{w'^2}$ are comparable to those in the vortex. For $\overline{u'^2}$ the highest turbulence level is not found in the center of the wake but on its pressure side, while the $\overline{v'^2}$ and $\overline{w'^2}$ components of Reynolds stress are located in the wake center. The turbulence levels throughout the flow-field decrease at the axial location of x/c_a = 1.82. The highest turbulence levels are still found in the vortex, but now in the center of the vortex region. Also, the turbulence levels in the wake have decayed considerably. The Reynolds stresses seem not to be influenced by the tip leakage vortex above the spanwise height of y/c_a = 0.55 and 0.70 at the axial locations of x/c_a = 0.61 and 1.82, respectively.

The normalized shear Reynolds stress contours $\overline{u'v'}$, $\overline{v'w'}$ and $\overline{u'w'}$ are plotted as a function of the spanwise, y/c_a, and pitchwise, z/c_a, coordinates at the downstream axial locations of $0.61c_a$ and $1.82c_a$ and are shown in figure 3-13. In all of the plots, the highest shear stress level is found in the vortex region. Outside of the vortex region, the shear stresses $\overline{u'v'}$ and $\overline{v'w'}$ are almost 0 everywhere, while $\overline{u'w'}$ is anti-symmetric in the wake region. The shear stresses in the wake regions seem not to be influenced be influenced by the tip leakage vortex. At the axial locations of $0.61c_a$ and $1.82c_a$, the region of influence of the vortex seems to be limited to the area below the spanwise heights of $0.55c_a$ and $0.70c_a$, respectively.

The turbulence kinetic energy, k, was calculated at both downstream axial locations of $0.61c_a$ and $1.82c_a$. The turbulence kinetic energy was calculated by equation 3-8, which is determined from the trace of the Reynolds stress matrix:

$$k = \frac{1}{2}\overline{u_i u_i} \tag{3-8}$$

Plotted in figure 3-14 are the contours of turbulence kinetic energy as a function of the spanwise, y/c_a, and pitchwise, z/c_a, coordinates. At both locations the turbulence kinetic energy (TKE) is greatest in the vortex region. At x/c_a = 0.61 the maximum TKE of about $0.012U_\infty^2$ is found to the right of the vortex. At x/c_a = 1.82 the maximum TKE levels are found near the center of the vortex. The TKE levels decay between the two locations all

throughout the flow-field. As expected, the influence of the tip leakage vortex seems to be limited to the region below y/c_a = 0.55 and 0.70 at x/c_a = 0.61 and 1.82, respectively.

From the Reynolds averaged Navier-Stokes equations, the turbulent kinetic energy transport equation can be derived. The final form of the TKE transport equation is written in vector notion in equation (3-9) as:

$$\overline{U_j}\frac{\partial k}{\partial X_j} = -\overline{u_i'u_i'}\frac{\partial \overline{U_i}}{\partial X_j} - \frac{\partial \overline{k'u_j'}}{\partial X_j} - \frac{\partial \overline{pu_i'}}{\partial X_i} - \frac{\upsilon\partial^2 k}{\partial X_k \partial X_k} - \frac{\upsilon\overline{\partial u_i'\partial u'}_i}{\partial X_k \partial X_k} \qquad (3\text{-}9)$$

The term to the left of the equal sign is the TKE convection term. TKE production is the first term to the right of the equal sign, TKE diffusion is the second term to the right of the equal sign, pressure diffusion is the middle term and the last two terms on the right are TKE dissipation and viscous diffusion.

TKE production was estimated from the measured data by numerical differentiation and by ignoring derivatives in the streamwise X direction. Figure 3-15 shows the cross-sectional contours of TKE production, Pc_a/U_∞^3, at the axial locations of 0.61c$_a$ and 1.82c_a, as a function of the spanwise and pitchwise coordinates. At 0.61c_a, the TKE production is the greatest between z/c_a = -2.7 and -3.0 (corresponds to location of maximum TKE) with a value of $0.0075U_\infty^3/c_a$. In the rest vortex region, low levels of TKE production are found and a small region of negative TKE production is found at approximately z/c_a = -2.7 and y/c_a = 0.1. The wakes of blades 4 and 5 also show small levels of TKE production, on the order of $0.001U_\infty^3/c_a$ to $0.002U_\infty^3/c_a$. At x/c_a = 1.82, TKE production is much lower, with only a small region located between z/c_a = -3.75 and -4.5 and between y/c_a = 0.1 and 0.4. The TKE production in this region is no greater than $0.002U_\infty^3/c_a$

3.7 Wake Profiles Downstream of the Blade Midspan

The wakes of the baseline blades measured at spanwise location of 0.92c_a are compared to plane wakes in this section. The analysis of the results will serve as the basis for comparison with the serrated trailing edge blades discussed in chapters 4 and 5.

3.7.1 Definition of Wake Parameters

In this section, the important parameters of the wake are defined. These will be used to normalize the mean velocities, turbulence terms and lengths. The various wake parameters are defined in figure 3-18 in terms of a mean velocity profile measured perpendicular to the wake (i.e. in the Z direction). Note that all the present measurements were made in profiles and planes parallel to the pitchwise (z) direction, since this is the plane in which a downstream stator row would reside. To obtain wake parameters from the present data, for comparison with the results of other wake studies, pitchwise directions were converted to perpendicular-to-wake directions simply by multiplying by the cosine of the angle between them (53.32 degrees). This approach ignores the effect of the streamwise development of the wake upon the profile shape, a small but not negligible effect.

The edge velocity, U_e, is defined as the local potential core velocity outside the wake. The maximum streamwise velocity deficit, U_w, is defined as the difference between the edge velocity and the minimum velocity in the wake. The half-wake width L_w is the distance between the locations where the velocity deficit reaches its maximum value and the location where it is half that. Half-wake widths were determined by curve-fitting the measured mean velocity profiles. The momentum thickness θ, defined as

$$\theta = \int_{-\infty}^{\infty} \frac{U}{U_e}\left(1 - \frac{U}{U_e}\right) dZ \qquad (3\text{-}10)$$

was determined by integration of the measured data using the trapezium rule over the measured range of the data.

3.7.2 Wake Characteristics of the Baseline GE-Rotor-B Blades

Wake characteristics were determined from the single-wire and quad wire measurements. Wake parameters are listed in table 3-4. Figure 3-17, shows the wake half-width normalized on the momentum thickness, L_w/θ, as a function of streamwise location normalized on the momentum thickness, X/θ. Plotted in this figure are the quad-wire and single-wire measurements of the baseline blades (excluding the single-wire

measurement made at the trailing edge). These are compared to the fully developed plane wake measurements of Devenport *et al* (1999). Devenport *et al.* performed single and two point measurements in the wake of an isolated NACA 0012 airfoil at zero angle of attack with the motivation to develop a more realistic representation of turbulence to compute the broadband noise produced from blade-wake interactions in helicopter rotors. The present quad wire and single wire data indicate spreading rates that are proportional to $(X/\theta)^{0.45}$, while the NACA 0012 wake data has a spreading rate that is proportional to $(X/\theta)^{0.49}$. Ideally, a fully developed wake should have a spreading rate that is proportional to $x^{0.50}$ as indicated in Cimbala *et al.* (1990). However, as will be seen below, this does not imply the turbulent wakes of the blades are fully developed.

Table 3-4: Wake parameters at the downstream axial locations of x/c_a = 0.002, 0.61, 1.18, 1.82 and 2.38.

Location (x/c_a)	U_e/U_∞	U_w/U_∞	L_w/c_a	θ/c_a
0.002	0.771	0.674	0.0340	0.0171
0.61	0.750	0.204	0.0558	0.0250
1.18	0.729	0.136	0.0729	0.0249
1.82	0.727	0.108	0.0904	0.0248
2.38	0.747	0.0986	0.106	0.0267

Figure 3-18 shows the centerline mean velocity deficit normalized on the edge velocity, U_w/U_e, as a function of the streamwise distance, X/θ. The data are plotted in comparison to the NACA 0012 wake data obtained by Devenport *et al* (1999). The quad-wire and single-wire measurements have decay rates that are proportional to $(X/\theta)^{-0.58}$ while the NACA 0012 wake data has a decay rate that is proportional to $(X/\theta)^{-0.54}$. The theoretical decay rate for a fully developed wake, indicated in Cimbala *et al.* (1990), is proportional to $x^{-0.50}$.

For a small deficit turbulent wake, the momentum thickness should remain constant with downstream distance. Figure 3-19 depicts the evolution of the momentum thickness as the wake develops downstream and it can be seen that it remains constant from at least from X/c_a = 1.01 downstream. At X/c_a of 0.003, the momentum thickness is less than downstream but this is most likely due to the fact that wake is still forming and the pressure across the flow is unlikely to be uniform this close to the blade. Wygnanski

et al. (1986), who studied the two-dimensional, turbulent, small-deficit wakes behind circular cylinders, a symmetrical airfoil, a flat plate and an assortment of screens of varying solidity with similar momentum thickness to determine their structure and self-preserving states, developed a curve fit to the momentum thickness for fully developed plane wakes which shows the preservation of the wake momentum deficit follows a unique relationship when θ/L_w is plotted versus U_w/U_e. The relationship that was developed is a second order polynomial as given in equation 3-11:

$$\frac{\theta}{L_w} = \frac{U_w}{U_e}\left(\Psi_1 - \frac{U_w}{U_e}\Psi_2\right) \tag{3-11}$$

For this polynomial, Wygnanski *et al* .(1986) determined the coefficients Ψ_1 and Ψ_2 to be 2.06 and 1.505, respectively. This has been reinforced by Devenport *et al.* who determined Ψ_1 to be 2.058 and Ψ_2 to be 1.505 from their measurements. Plotting the data from the quad and single-wire measurements, figure 3-20, and determining the coefficients (table 3-5), it can be seen these values are close to those determined by Wygnanski *et al.* (1986) and Devenport *et al*. (1999). In the same figure, the curve fit to Devenport *et al.* (1999) data has also been plotted. It is important to note that the GE Rotor B blade data lies on this same curve as Devenport *et al*. (1999), showing that the four points used to determine the coefficients are not enough to accurately determine the values of Ψ_1 and Ψ_2. Since the wakes are not fully developed, which will be shown in a later section, the coefficients of curve fit may not be indicative of the final characteristics of the turbulent plane wake.

Table 3-5: Coefficients of the momentum thickness curve fit

Measurement	Ψ_1	Ψ_2
Baseline Blades (Quad-Wire)	2.138	1.758
Devenport *et al*	2.058	1.505

3.7.3 Mean Velocity Profiles

The mean velocity profiles, U/U_e, at the axial locations of $0.61c_a$, $1.18c_a$, $1.82c_a$ and $2.38c_a$ are plotted in figure 3-21 as a function of the pitchwise, z/c_a, and axial, x/c_a,

coordinates. This plot shows the wake does not propagate parallel to the axial coordinate, as was mentioned earlier. Also, the spreading of wake and the decay of the velocity deficit are evident in the profiles.

Figure 3-22 shows normalized mean velocity profiles at axial downstream locations of $0.002c_a$, for the single-sensor hot-wire measurements, and $0.61c_a$, $1.18c_a$, $1.82c_a$ and $2.32c_a$ for the four-sensor hot-wire. The velocity was normalized by:

$$\frac{U - U_e}{U_w} \tag{3-12}$$

where U is the mean velocity in the flow, U_e is the edge velocity of the wake and U_w is the maximum velocity deficit in the wake. While the profiles were, of course, measured in the pitchwise z direction they are presented here in terms of distance perpendicular to the plane of the wake Z. The distance Z, measured from the wake center, was normalized using the length scale of the wake, L_w. By using this type of normalization, it is clear to see in figure 3-22 that the plots of the mean velocity deficit at $0.61c_a$, $1.18c_a$, $1.82c_a$ and $2.38c_a$ are close to collapsing on top of each other or in other words becoming self-similar. According to Pope (2001) self-similarity is not reached until U_w/U_e is approximately equal to 1/10. Referring to figure 3-18, using the above criteria self-similarity will not be reached until $200X/\theta$ which is equivalent to 3.0 axial chords downstream of the blade row. In figure 3-22 the mean velocity profile deficit at x/c_a = 0.002 does not fit the trend at the other locations.

For the mean wake profiles, $(U\text{-}U_e)/U_w$ versus Z/L_w, Wygnanski *et al*. (1986) also developed a curve fit which accurately describes the profile shape. The curve fit for this data is an exponential function in the form of equation 3-13:

$$\frac{U - U_e}{U_w} = -\exp\left(-k_1 \frac{Z^2}{L_w^2} - k_2 \frac{Z^4}{L_w^4}\right) \tag{3-13}$$

where the constants k_1 and k_2 were determined to be 0.637 and 0.056 respectively. Using the same curve fit to describe their profile shape, Devenport *et al*. (1999) were able to determine the constants k_1 and k_2 to have the values of 0.632 and 0.0612. Applying the same curve fit to mean velocity data presented in figure 3-22(a), the constants k_1 and k_2 were determined to be 0.632 and 0.0247. The constants were determined through a trial-and-error method. Altering k_1 changes the width of the plot while altering the value of k_2

modifies the shape of the plot near the edge of the wake. The fully-developed plane wakes are symmetric about their center while the wakes measured in the linear cascade tunnel are close to being symmetric, but from the profile line through the data, it can be seen that suction side of the wake has a shallower slope than the pressure side. This may simply be because the data was not measured perpendicular to the wake, a difference that is also apparent in the turbulence intensities.

In a purely two-dimensional fully-developed plane wake the spanwise velocity component should be zero or negligible. However, in this flow field, there exists a small velocity component in the spanwise direction as shown in figure 3-23, which is plot of V/U_w versus Z/L_w. The magnitude of the velocity variation ranges from $2\%U_w$ to a maximum of $8\%U_w$ across the wake. The same variation in magnitude and velocity distribution was seen in Devenport *et al.* (1999) who believed the variation may be due to the presence of a vortex sheet in the fluid created by ±0.1 degree variation in the angle of attack of their airfoil. This may also be true here but some of the variation is due to the three-dimensional effects of the finite span blade. Also, three-dimensional effects are seen in the W component of the velocity in figure 3-24. The difference between the minimum and maximum peaks of the W velocity component decay with downstream location.

3.7.4 Turbulence Measurements

Figures 3-25(a), (b) and (c) show the normalized normal turbulence stresses, $\overline{u'^2}/U_w^2$ $\overline{v'^2}/U_w^2$, and $\overline{w'^2}/U_w^2$ plotted against distance perpendicular to the wake centerline, Z/L_w, while figures 3-26(a), (b) and (c) show the normalized shear turbulence stresses $\overline{u'v'}/U_w^2$, $\overline{u'w'}/U_w^2$, and $\overline{v'w'}/U_w^2$ versus Z/L_w. For a plane wake the normalized Reynolds stresses, $\overline{u'^2}$, $\overline{v'^2}$, $\overline{w'^2}$ and $\overline{u'w'}$, should all approach self-similarity. Clearly in figure 3-25(a) through 3-26(c) the wake has not reached self-similarity and it is still developing. Once self-similarity has been reached, Wygnanski *et al*. (1986) observed the Reynolds normal stress $\overline{u'^2}$ will obtain a maximum value of almost $0.18U_w^2$ while the Reynolds shear stress $\overline{u'w'}$ obtained a maximum value of $0.05U_w^2$ and a minimum value of $-0.05U_w^2$ in

the wake of a symmetric airfoil. The Reynolds normal stress $\overline{u'^2}$ in figure 3-25(a) has a maximum value of $0.15U_w^2$ and the Reynolds shear stress $\overline{u'w'}$ in figure 3-26(b) reaches a maximum value of $0.04U_w^2$ and a minimum close to $-0.05U_w^2$. This reinforces the fact the wakes are still developing at x/c_a of 2.38.

The Reynolds shear stress terms $\overline{u'v'}$ and $\overline{v'w'}$ in a truly plane wake are zero, however, in figure 3-26(a) and 3-26(c) this is not the case. Even though these values are non-zero they are smaller in magnitude compared to the cross term $\overline{u'w'}$. The shear terms $\overline{u'v'}$ and $\overline{v'w'}$ are at most ¼ of the $\overline{u'w'}$ stress. By comparing these plots to the mean velocity profiles V/U_w, the presence of the weak shed vorticity and the three-dimensional effects may have introduced a small shear term. Referring to figure 3-10 the spanwise velocity is small but not 0 at the midspan.

The turbulence kinetic energy, k, present in a wake can be determined by taking one-half of the trace of the Reynolds stress tensor and can be written as was shown in equation 3-8 above. Figure 3-27 shows the normalized turbulence kinetic energy, k/U_w^2, as a function of the normalized distance, Z/L_w, at x/c_a of 0.61, 1.18, 1.82 and 2.38. As is expected by looking at the Reynolds normal stresses, the progression toward a self-similar state is also seen in the kinetic energy plot.

3.7.5 Spectral Measurements

Spectral measurements were performed at every 5th measurement point in the midspan profiles at the downstream locations of x/c_a of 0.6, 1.2, 1.8 and 2.4. From the spectral measurements it is possible to determine the extent of any periodic behavior present in the turbulence and determine the amount of energy present in the periodic behavior.

Figures 3-28(a) through (c) are normalized spectral plots. The spectral functions G_{uu}, G_{vv} and G_{ww} on the vertical axis are normalized by $(1/U_w^2)(U_e/L_{w,p})$ and the frequency, f, on the horizontal axis is normalized by $(L_{w,p}/U_e)$. Here $L_{w,p}$ is the wake half width measured in the pitchwise direction, equal to $L_w/\cos(53.32^o)$. The first spectral figure, figure 3-28(a), shows the normalized spectral functions as a function of frequency at the wake center at the different streamwise locations. Similar to the velocity and the turbulence characteristics these spectral plots should also ultimately reach self-similarity,

but this has clearly not happened here. The inertial subregion (slope is -5/3) of the u and v components are approximately a decade wide in the frequency. In the w spectra there is a strong peak at normalized frequency, $f(L_{w,p}/U_e)$, of $2\text{x}10^{-1}$ which appears to decay rapidly with downstream distance, relative to the rest of the spectrum, perhaps indicating a periodic or quasi-periodic eddy structure in the early wake. A weaker peak is also seen in the v-spectra at the normalized frequency of $2\text{x}10^{-1}$ and this also decays with the downstream distance. By $x/c_a = 1.82$ the peak has completely disappeared.

3.7.6 Repeatability

At $x/c_a = 0.61$ multiple midspan wake measurements were performed. These multiple measurements were carried out with the intent to show repeatability of the experimental methods. To show repeatability, the same run was performed on different dates, for different calibrations of the quad wire, mounting and setting of the probe (which includes replacing the Mylar measurement grid), and removal and replacement of the tailboards.

Figure 3-29 is the plot of the normalized mean streamwise velocity profiles and figure 3-30 is a plot of the normalized TKE. In both plots, runs 2 and 3 are qualitatively identical. Run 2 is the data set used for analysis in the previous sections. In figure 3-31, the largest deviation occurs at the outer edges of the wake, which is most likely due to differences in the coordinate system rotation of the two profiles, while in figure 3-32, the largest deviation occurs in the peaks of the TKE, but these variations are still small compared to the scale.

The four wake parameters, U_e/U_∞, U_w/U_∞, L_w/c_a, and θ/c_a were calculated and compared for the two runs, table 3-6. For comparison purposes, run 2 was used as the reference. In table 3-5 below, the largest variation occurs between U_e/U_∞ and U_w/U_∞ with differences of 1.3% and 1.5%, respectively. This variation is most likely due to the variation of the free-stream velocity measured the two cases, because the difference in U_w/U_e between the two cases is 0. There was a small variation in L_w/c_a of 0.36% between the two runs, but this variation may have arisen through the polynomial approximation of

the wake profile. Finally, the momentum thicknesses for the two runs are identical, indicating that the initial conditions of the wakes are also identical.

Table 3-6: Comparison of wake properties for two runs performed at $x/c_a = 0.61$.

Measurement	U_e/U_∞	U_w/U_∞	U_w/U_e	L_w/c_a	θ/c_a
Run 2 (ref.)	0.750	0.204	0.272	0.0558	0.0250
Run 3	0.740	0.201	0.272	0.0556	0.0250
Δ	0.010	0.003	0	0.0002	0
% Difference	1.3%	1.5%	0	0.36%	0%

3.8 Summary

In this chapter the measurements performed on the wakes of the baseline GE-Rotor-B blades in Virginia Tech's Linear Cascade Tunnel were presented and analyzed. Various types of measurements were performed to determine the characteristics of the wake as well as the tip leakage vortex downstream of the blade row. Blade loading measurements were performed to establish the initial conditions of the wakes. The cross-sectional measurements performed at two downstream locations were performed to reveal tip leakage vortex and used to determine to what degree the wakes were two-dimensional. Finally, mid-span measurements were performed to determine wake characteristics, for example, spreading and velocity deficit decay rates, as well as to compare to previous studies performed on plane wakes.

The measurements that were analyzed were the Pitot-static cross-sections performed at $x/c_a = 0.84$ and 1.88 the four-senor hot-wire cross-sections at $x/c_a = 0.61$ and 1.82, the mid-span measurements performed with the single-wire at $x/c_a = 0.002$ and the four-sensor hot-wire mid-span measurements performed at $x/c_a = 0.61$, 1.18, 1.82 and 2.38.

Pitot-static cross-sectional measurements were performed across one period in the pitchwise direction and encompassed almost the entire spanwise height of the tunnel. From these measurements, the wake behind blade 5 and the tip leakage vortex of blade 4 were revealed. Also, the effects of the blade root covers could be seen on the flow in the vicinity of the upper endwall. The growth of the wake and vortex regions were seen in

these measurements as well as the decay of the velocity deficits in both of theses regions. These measurements were the fundamental measurements for the three-component velocity and turbulence cross-sectional measurements.

Cross-sectional four-sensor hot-wire measurements were performed at $x/c_a = 0.61$ and 1.82. These measurements were a continuation of the Pitot-static measurements, except they were only performed from the lower endwall to the mid-span of the blade. From these measurements, the three component velocity turbulence properties were obtained. The same flow-field features that were seen in the Pitot-static cross-sections were seen in these cross-sections. The maximum streamwise vorticity of the tip leakage was calculated and it was shown the maximum streamwise vorticity decayed from $x/c_a = 0.61$ to $x/c_a = 1.82$. Also, seen were the decay of the turbulence properties and triple-products over the entire flow field. The same features were seen in the TKE production. Finally, it was shown that the flow at the mid-span of the blades is almost two-dimensional.

The mid-span measurements were performed and compared to plane wakes. The wakes of the GE-Rotor-B blades are very similar to the plane wake, with a spreading rate proportional to $x^{0.47}$ and a velocity deficit decay rate proportional to $x^{-0.58}$. The wakes were also shown to be progressing towards self-similarity, with self-similarity being reached in the normalized streamwise velocity but not quite in the turbulence profiles. Finally, the spectral data showed the possibility of vortex shedding, when peaks were found in the *w*-spectra. Peaks were also found in the *v*-spectra at the axial stations closer to the blade row, but these decreased in size as the wake propagated downstream.

These measurements were performed to establish the baseline configuration to which the wakes of the serrated trailing edge blades will be compared to. The geometric profiles and the Pitot-static cross-sections of the serrated trailing edge blades are presented in the next chapter, chapter 4, while the three-component cross-sectional and mid-span measurements are analyzed and described in detail in chapter 5.

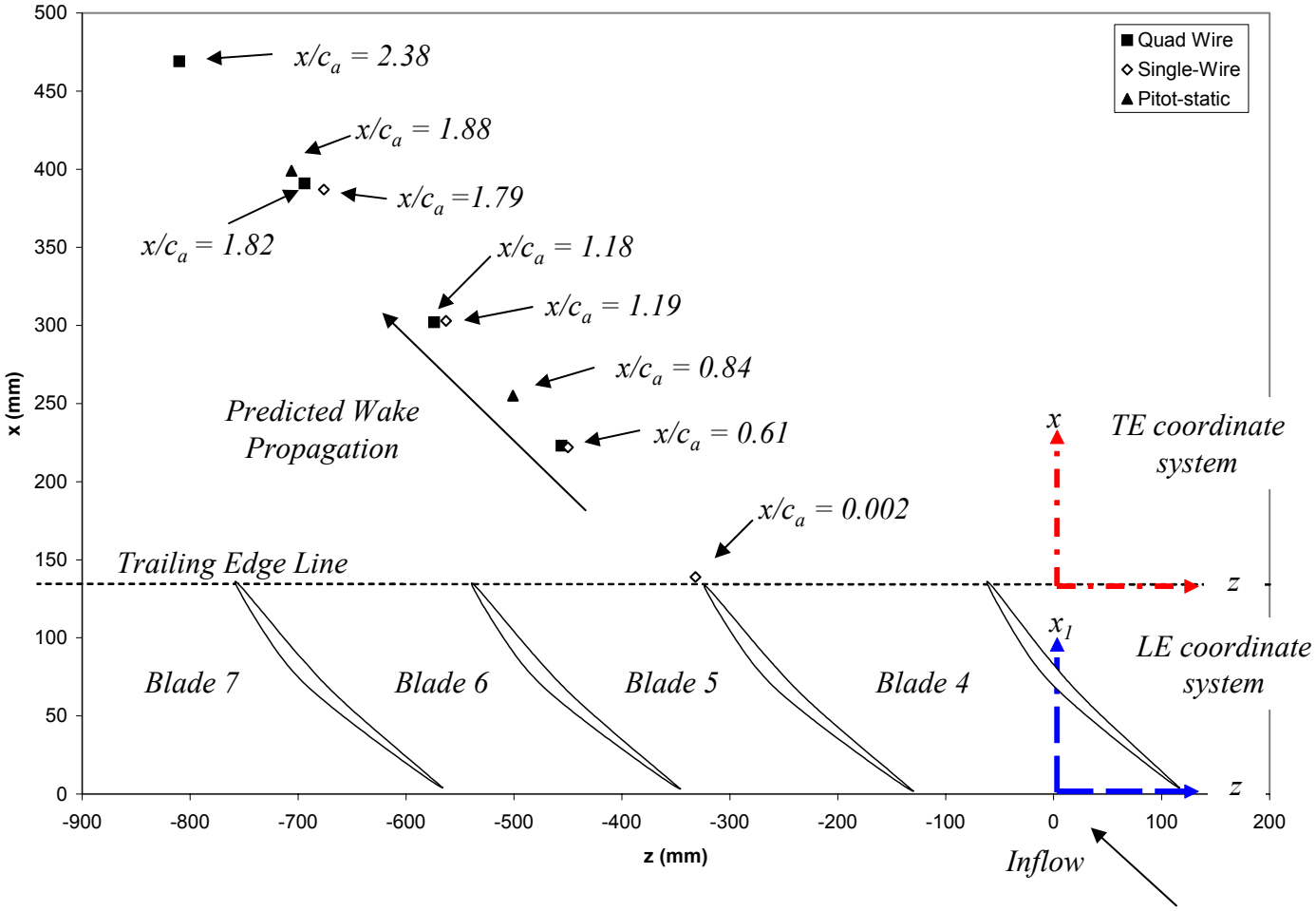

Figure 3-1: Wake measurement locations with respect to the trailing edge coordinate system.

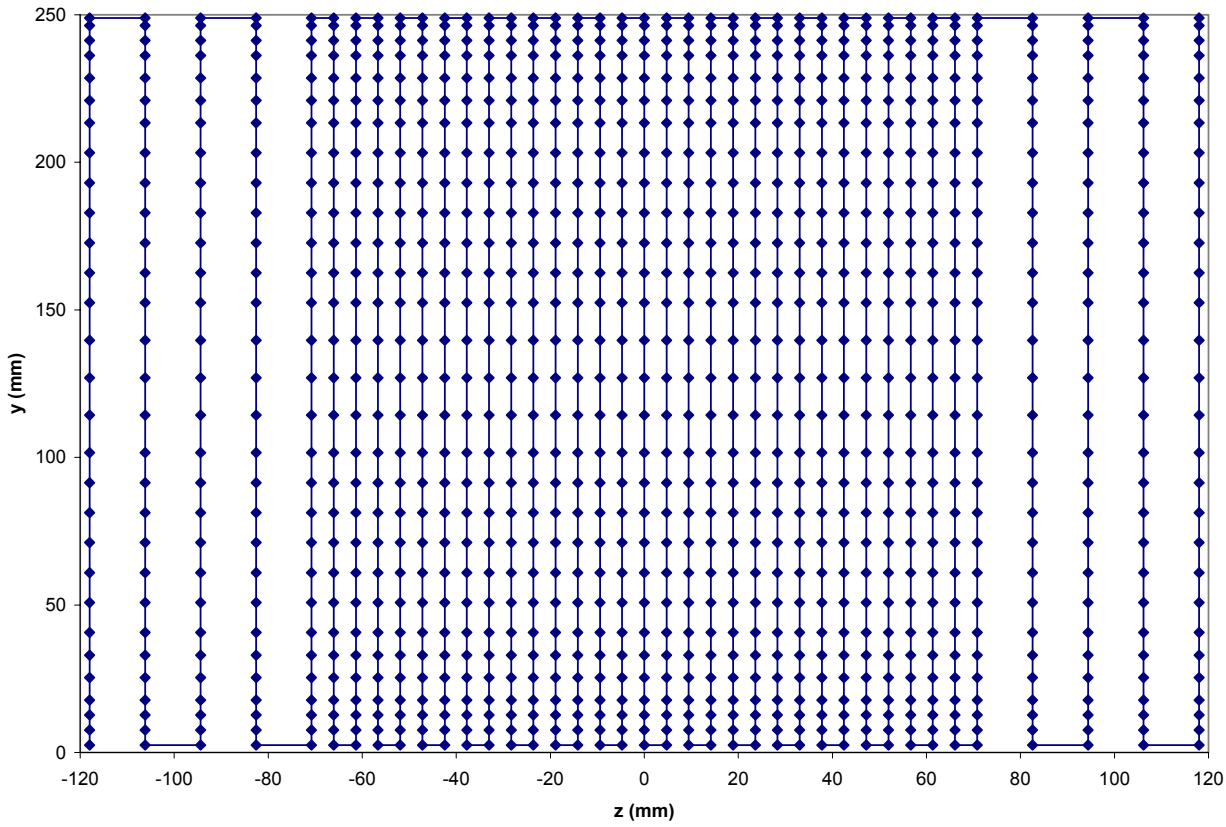

Figure 3-2: Pitot-static cross-sectional measurement grid used at $x/c_a = 0.84$ and 1.88

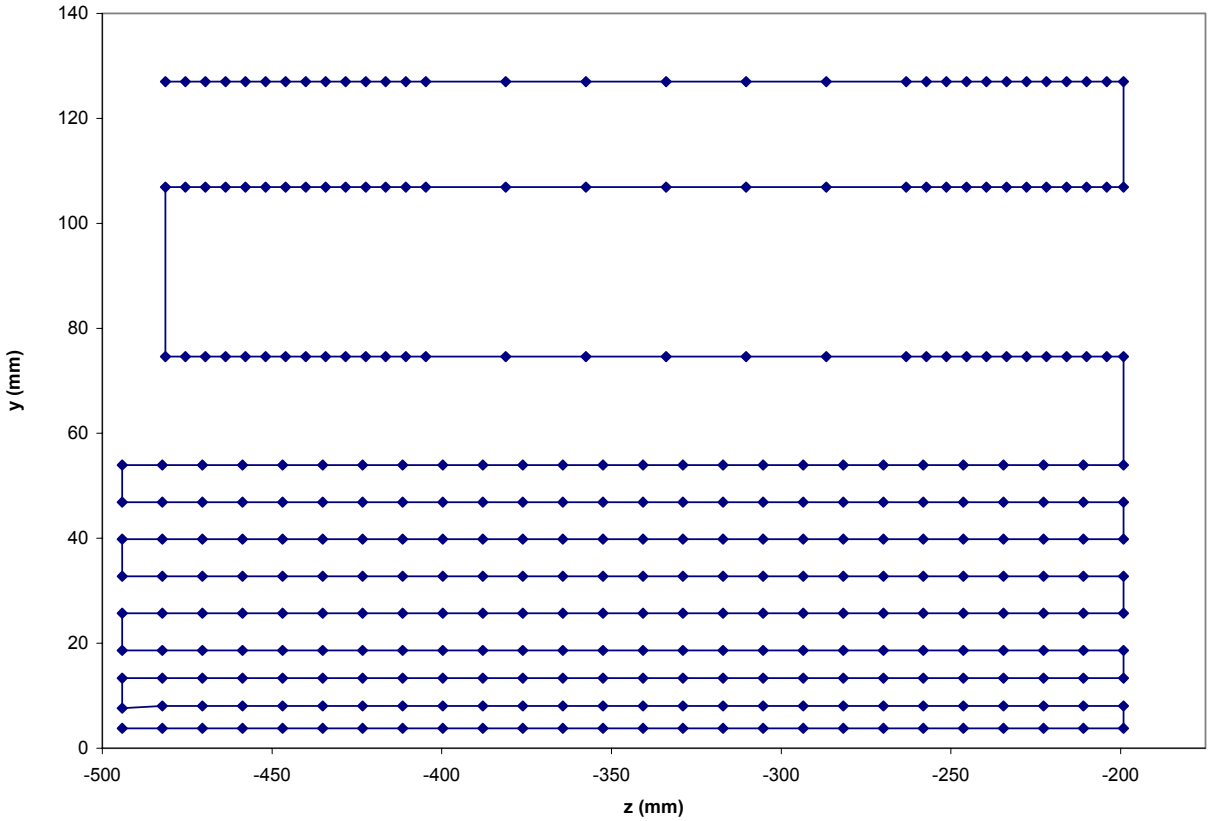

Figure 3-3:Cross-sectional measurement grid used at $x/c_a = 0.61$

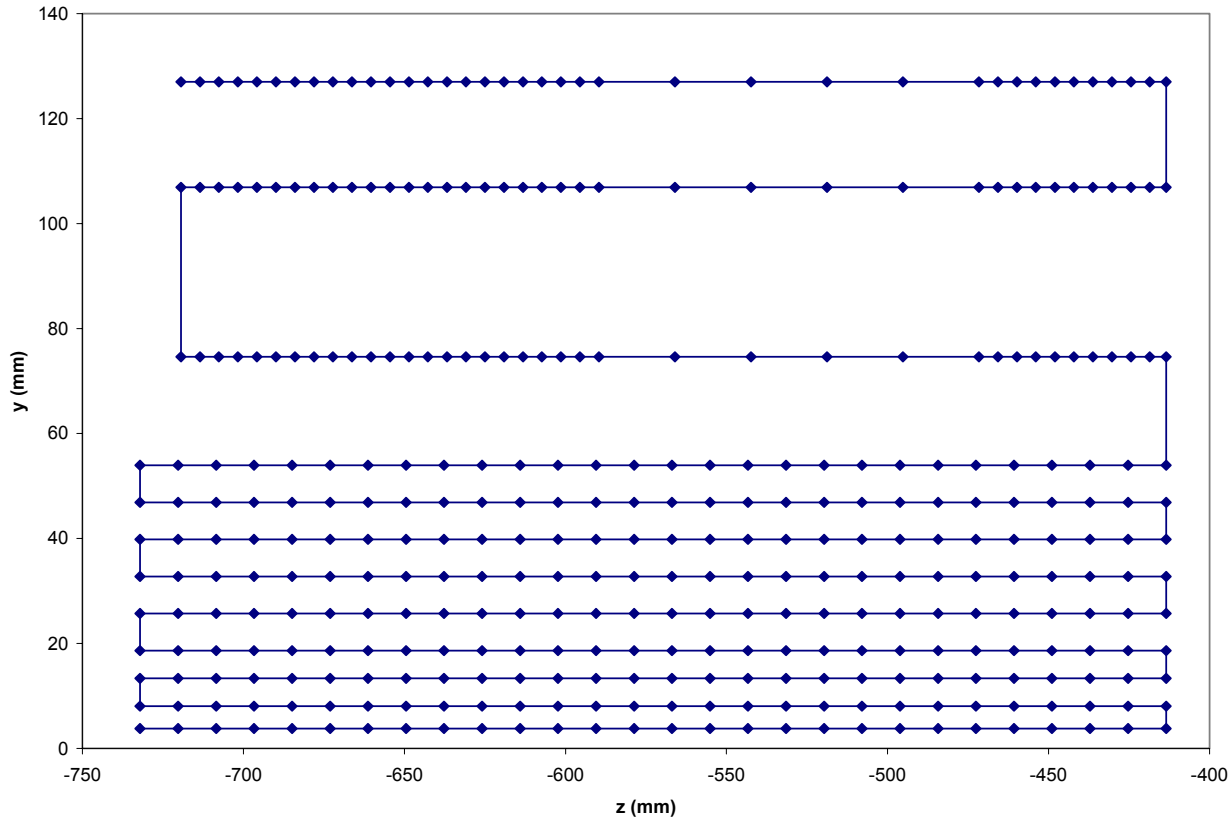

Figure 3-4: Cross-sectional measurement grid used at x/c_a=1.82

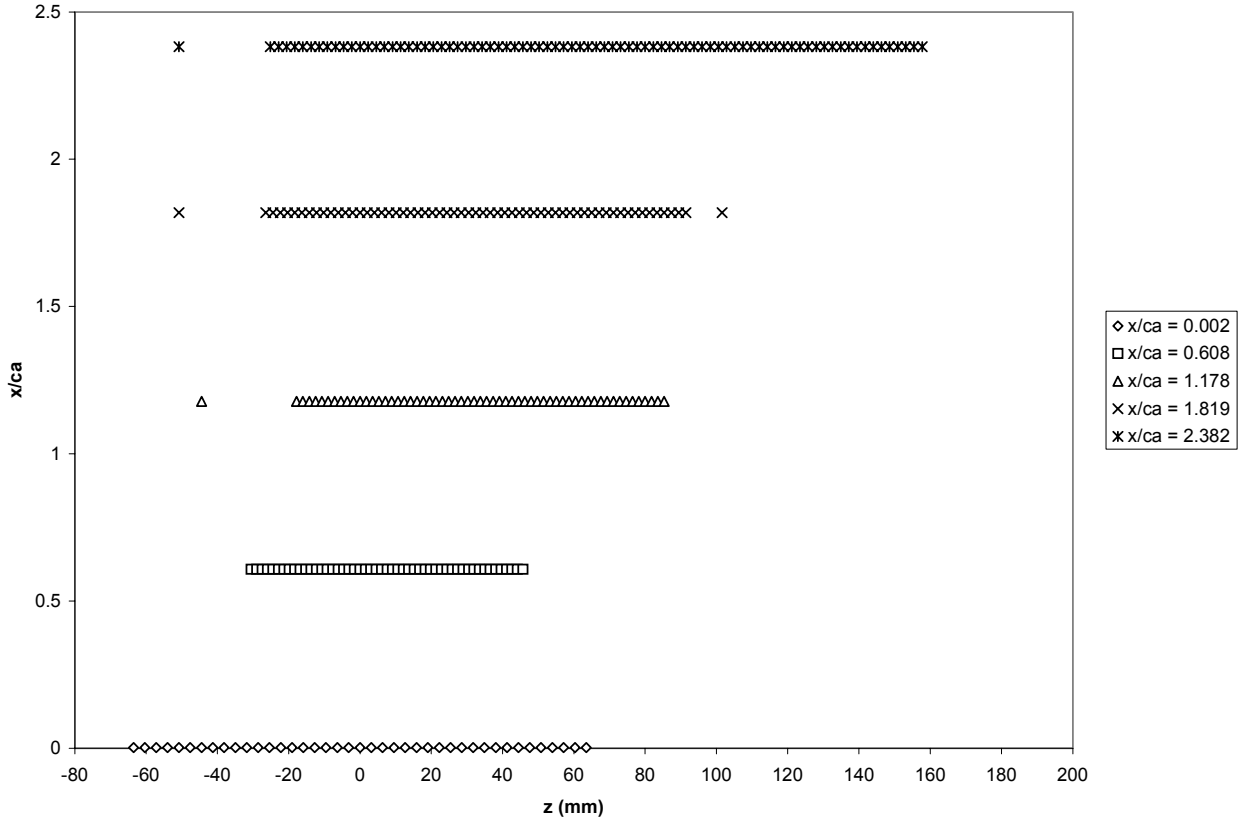

Figure 3-5: Grids for mid-span measurements performed at $y/c_a = 0.92$ for the downstream locations of $x/c_a = 0.002$, 0.61, 1.18, 1.82 and 2.38.

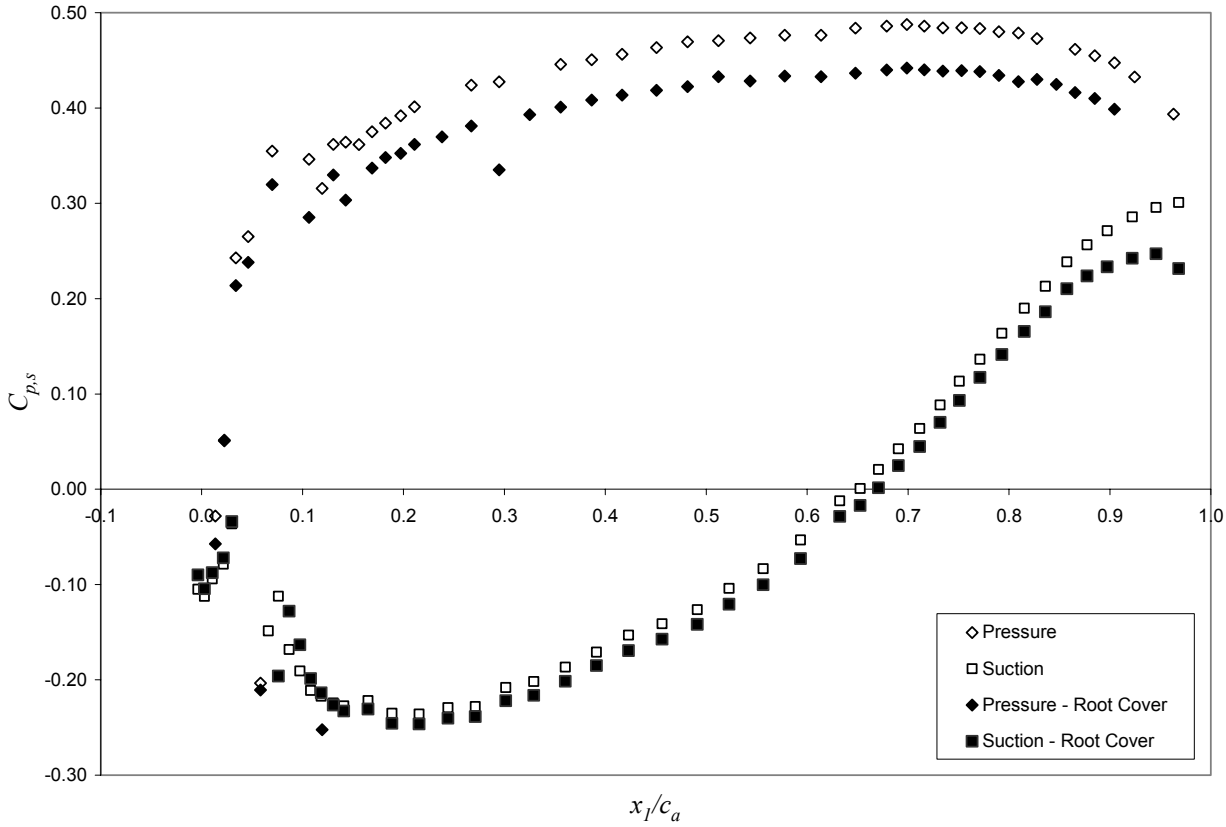

Figure 3-6: Blade loading, $C_{p,s}$, for both the uncontrolled and 1 mm controlled blade root opening versus the axial distance from the leading edge, x_1/c_a, for the baseline GE-Rotor-B blades

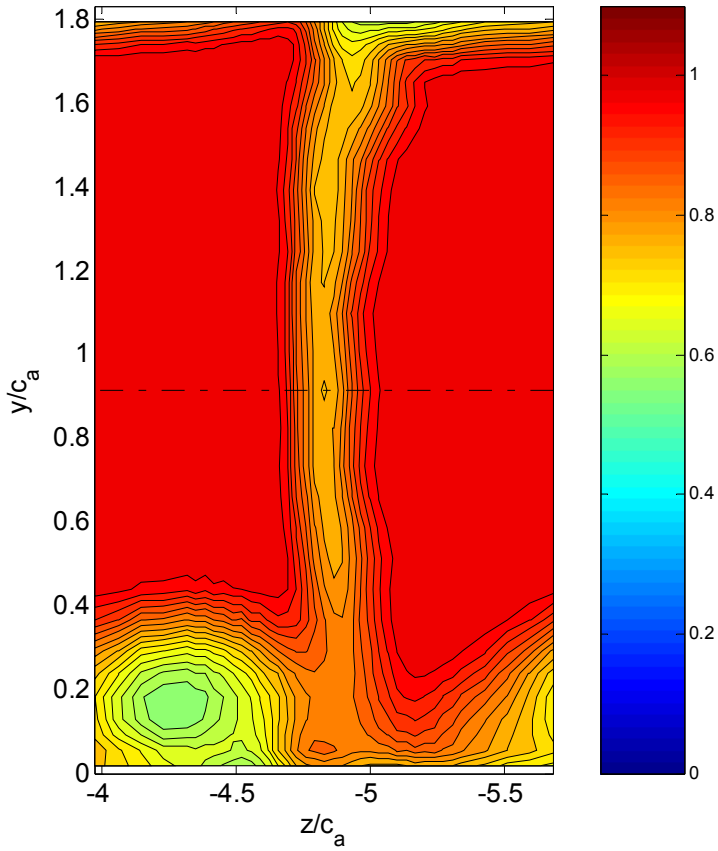

(a) Total pressure coefficient, $C_{p,o}$

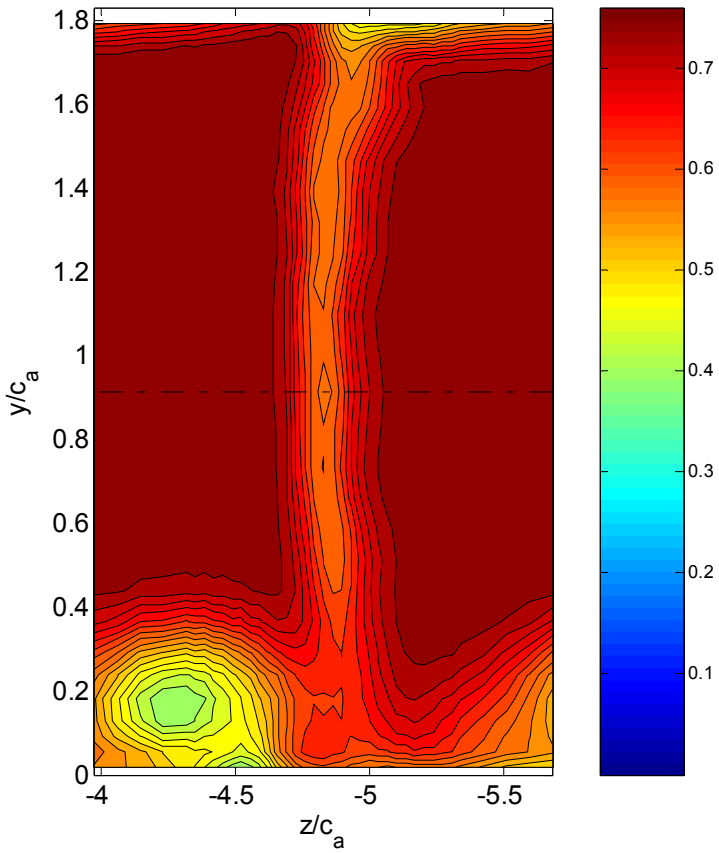

(b) Local mean streamwise velocity normalized on the reference velocity, U/U_∞

Figure 3-7: Pitot-static cross-sectional measurements for the baseline at $x/c_a = 0.83$

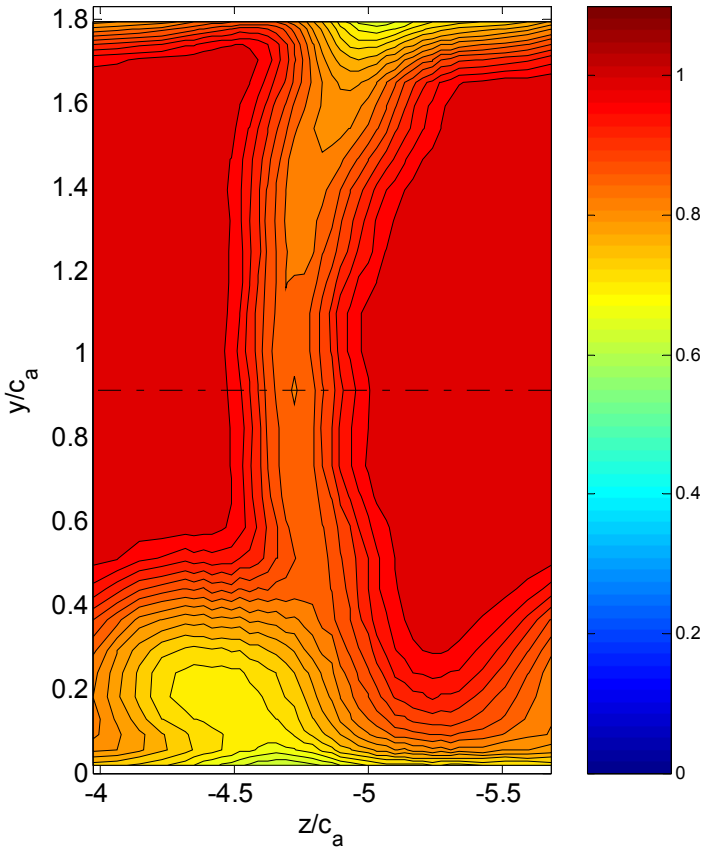

(a) Total pressure coefficient, $C_{p,o}$

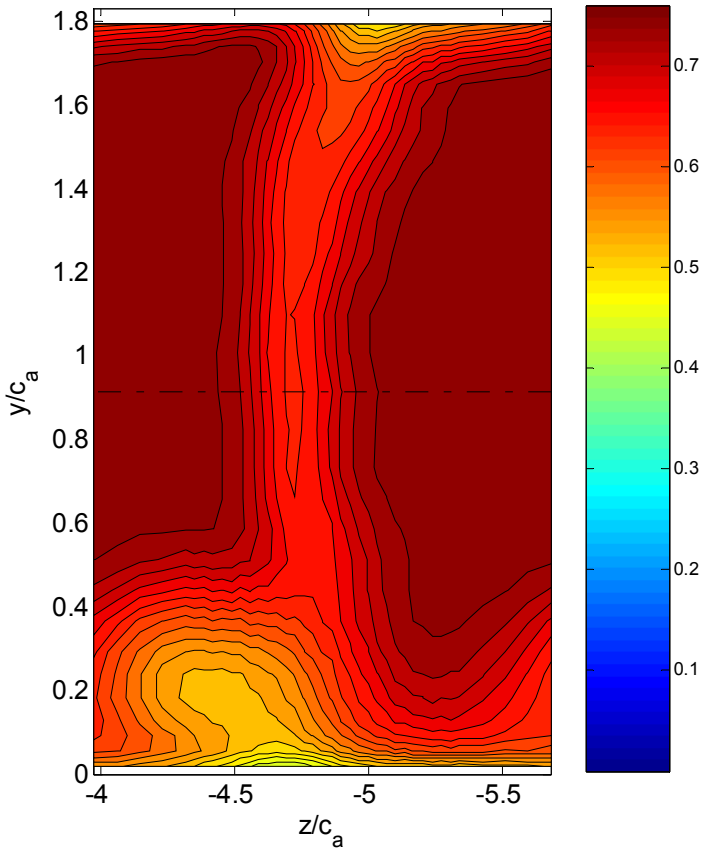

(b) Local mean streamwise velocity normalized on the reference velocity, U/U_∞

Figure 3-8: Pitot-static cross-sectional measurements for the baseline at $x/c_a = 1.88$

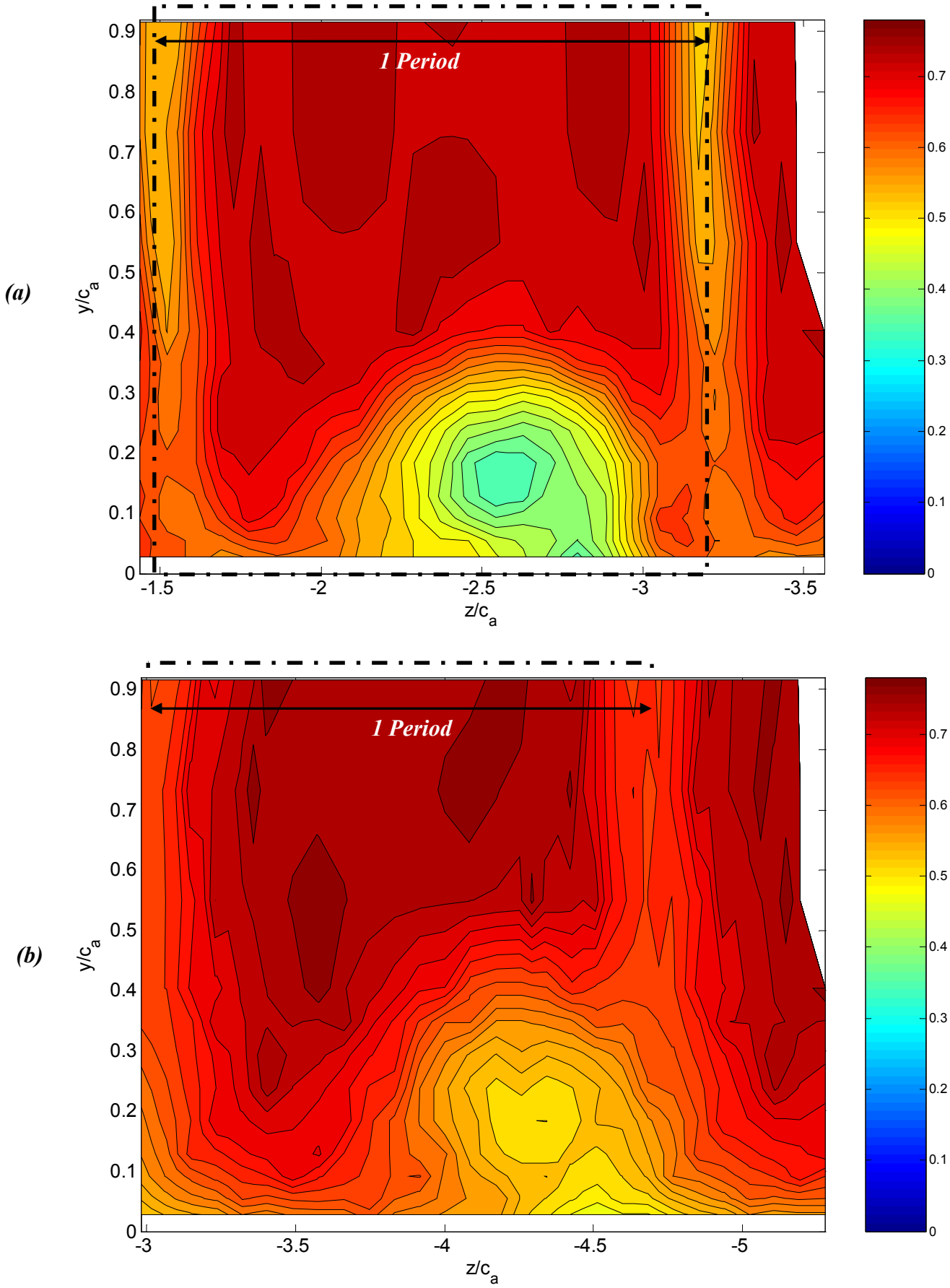

Figure 3-9: Cross-sectional normalized streamwise velocity profile, U/U_∞: ***(a)*** $x/c_a = 0.61$, ***(b)*** $x/c_a = 1.82$.

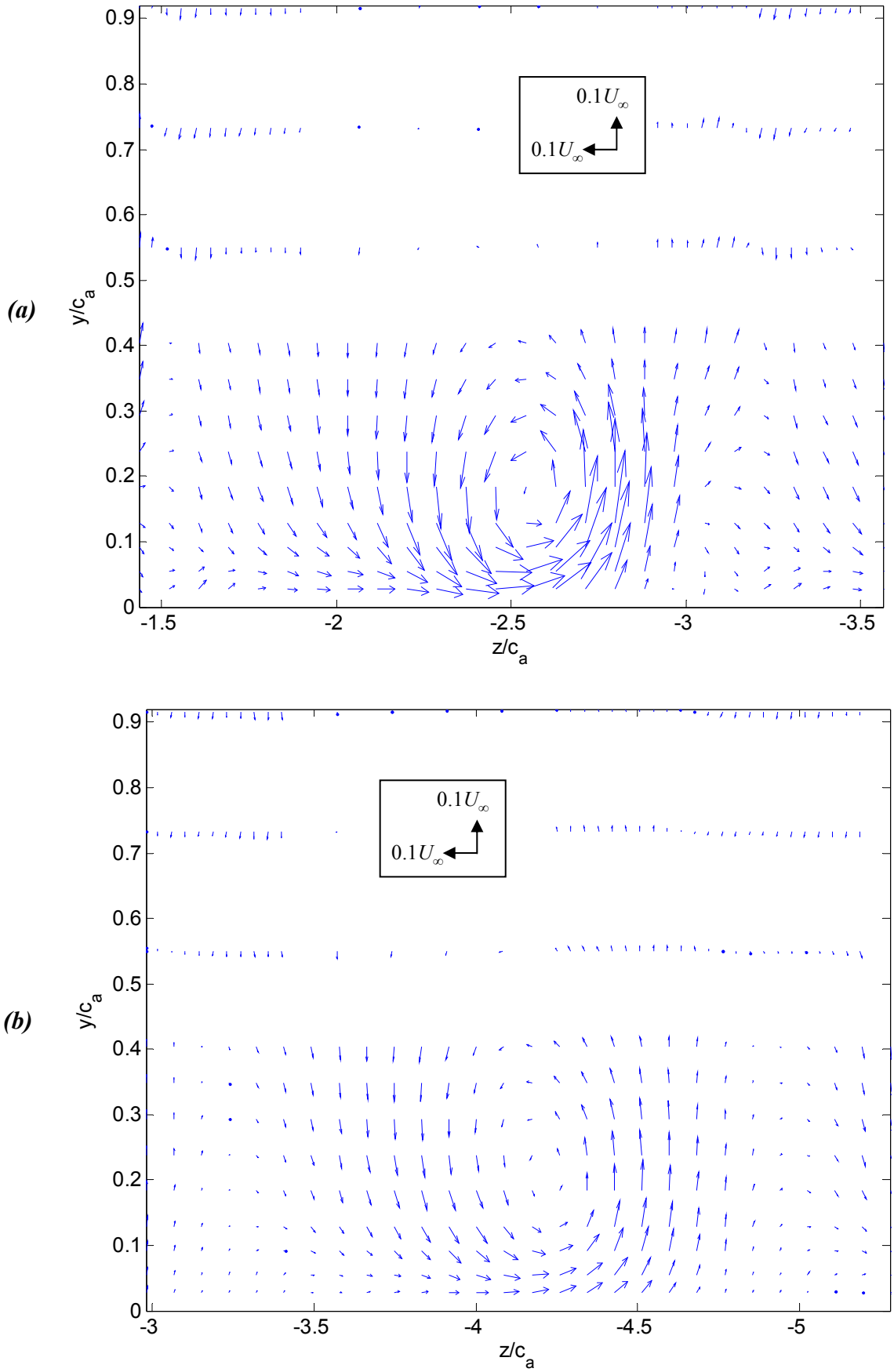

Figure 3-10: Cross-sectional vector plot of V/U_∞ and W/U_∞: ***(a)*** $x/c_a = 0.61$, ***(b)*** $x/c_a = 1.82$.

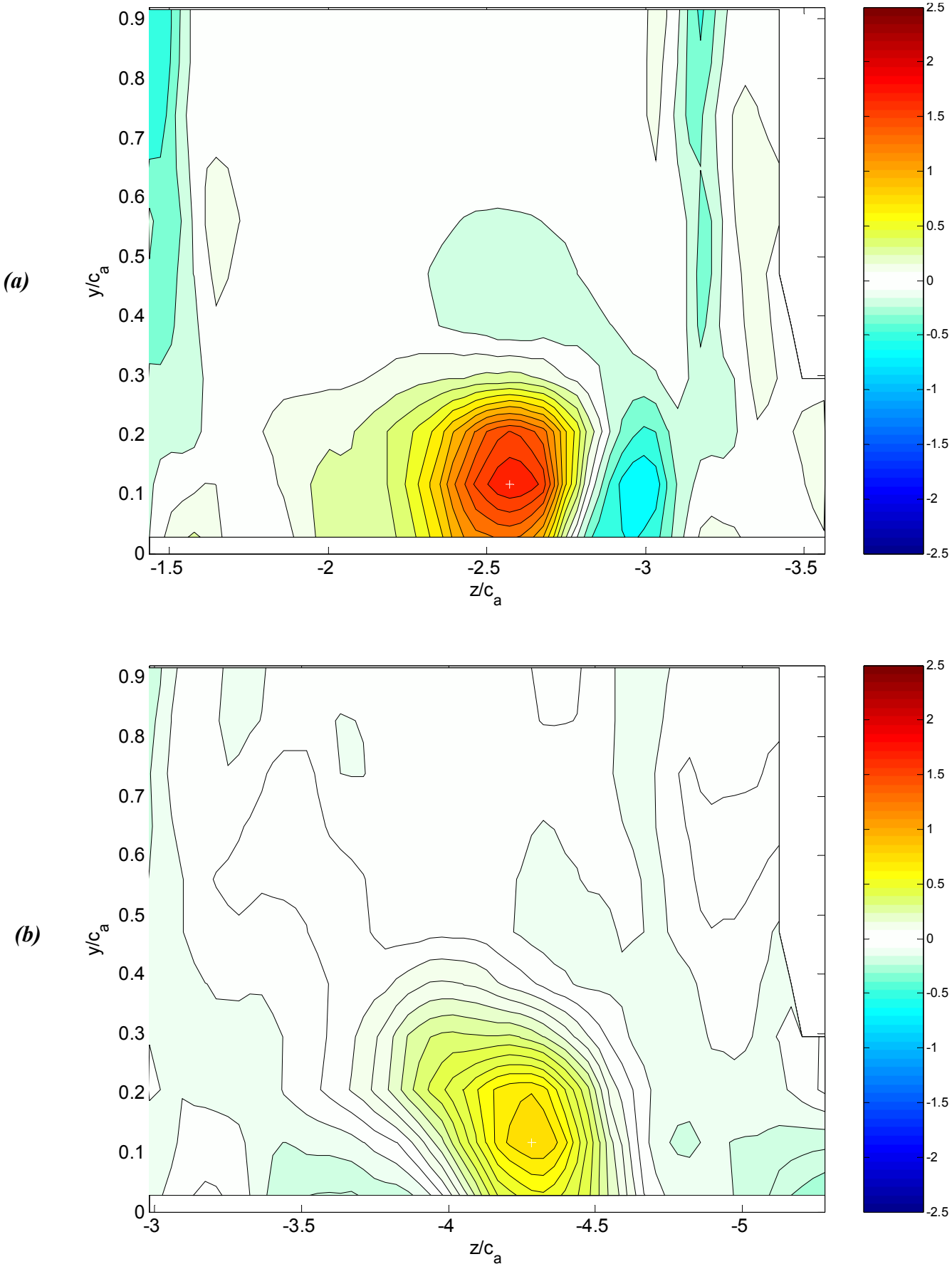

Figure 3-11: Streamwise vorticity plots, $\Omega_x c_a/U_\infty$: ***(a)*** $x/c_a = 0.61$, ***(b)*** $x/c_a = 1.82$.

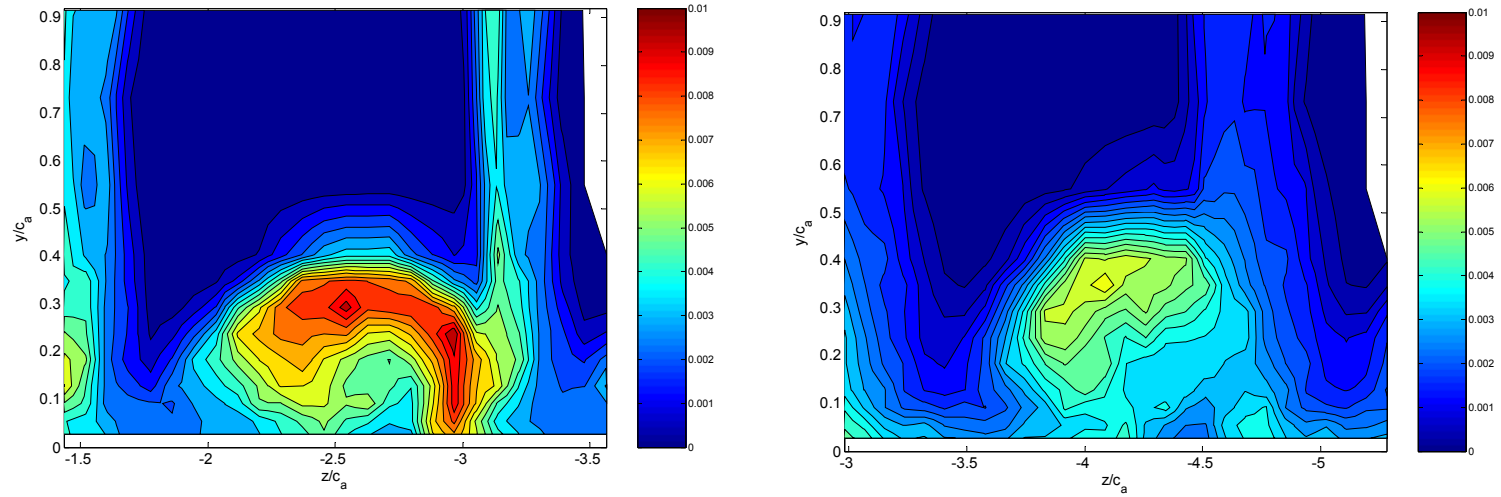

$x/c_a = 0.61$ ***(a)*** $x/c_a = 1.82$

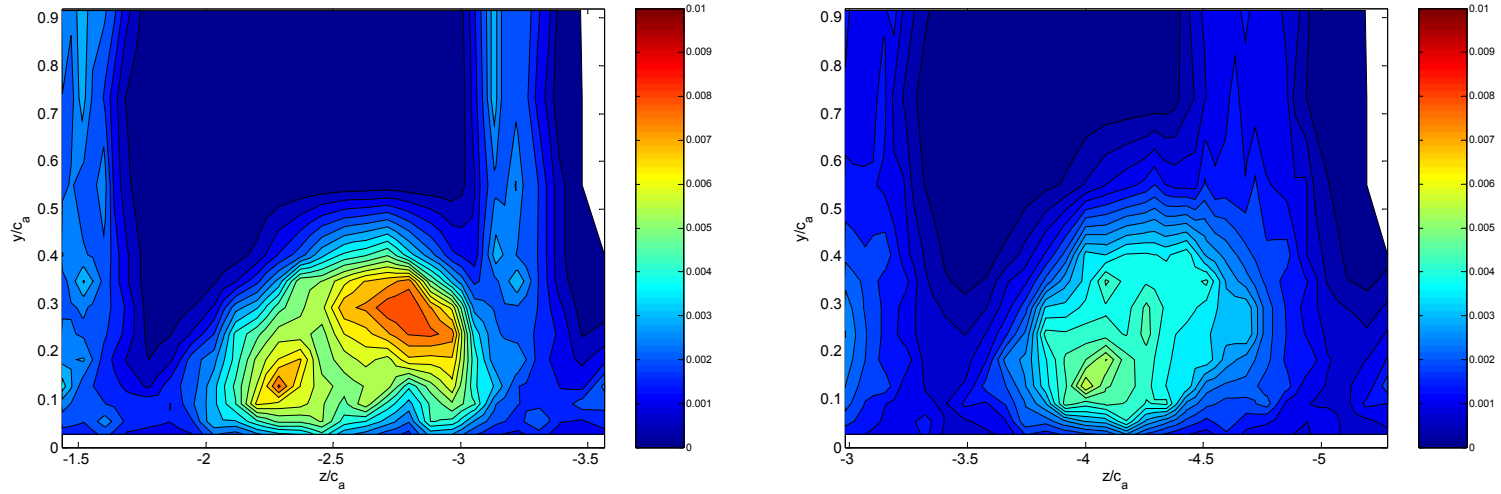

$x/c_a = 0.61$ ***(b)*** $x/c_a = 1.82$

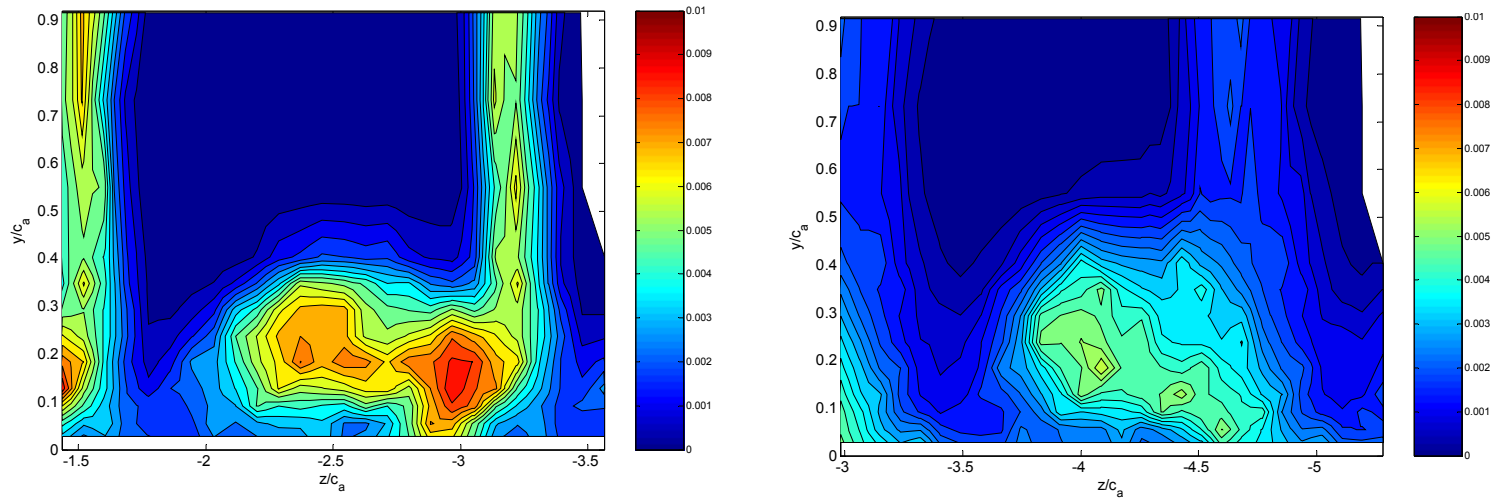

$x/c_a = 0.61$ ***(c)*** $x/c_a = 1.82$

Figure 3-12: Cross-sectional plots of turbulence intensities in the flow-field at $x/c_a = 0.61$ and 1.82 : ***(a)*** streamwise component, $\overline{u'^2}/U_\infty^2$, ***(b)*** spanwise component, $\overline{v'^2}/U_\infty^2$, ***(c)*** cross-wake component, $\overline{w'^2}/U_\infty^2$

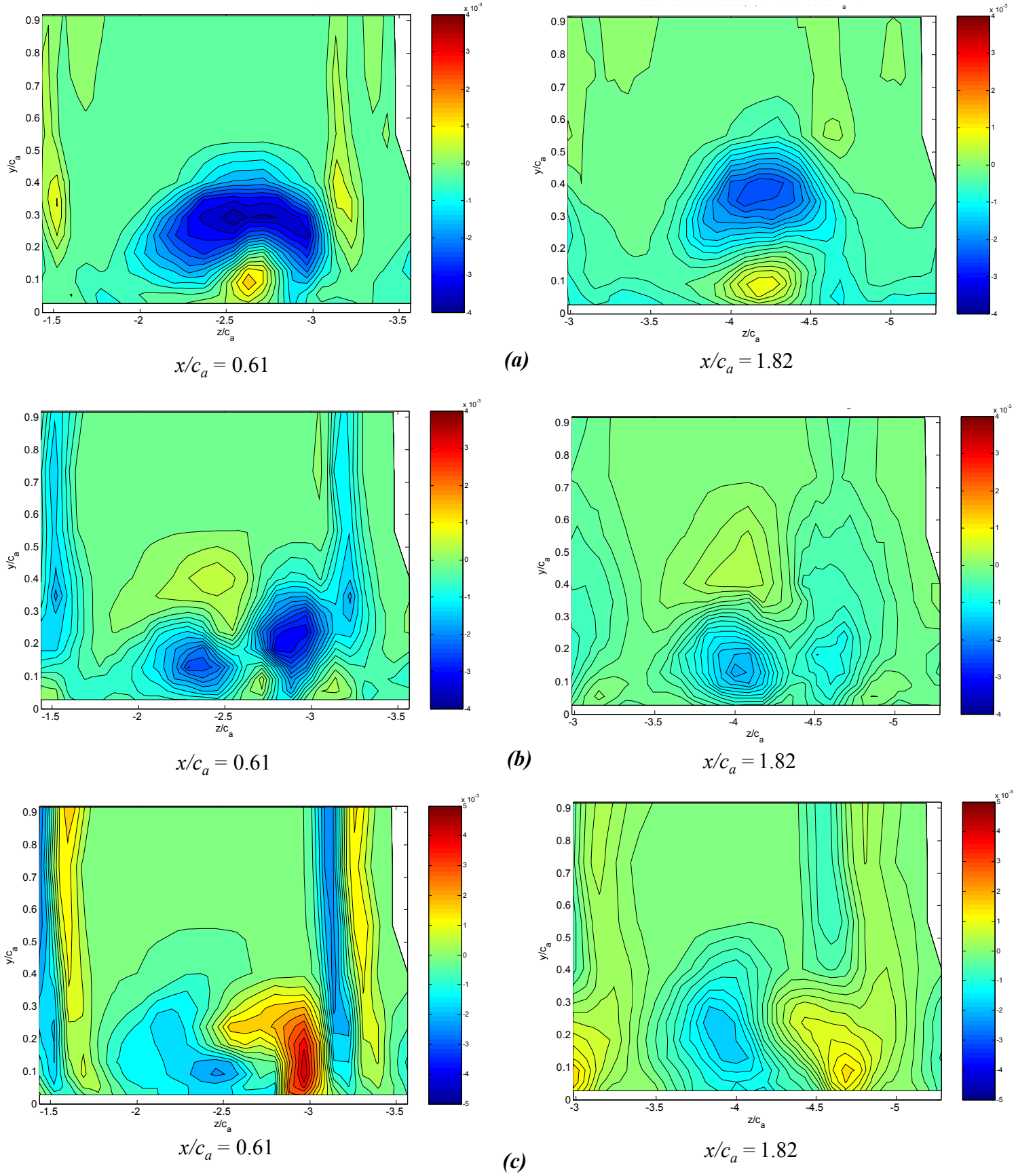

Figure 3-13: Cross-sectional plots of turbulence intensities in the flow-field at $x/c_a = 0.61$ and 1.82: ***(a)*** $\overline{u'v'}/U_\infty^2$, ***(b)*** $\overline{v'w'}/U_\infty^2$, ***(c)*** $\overline{u'w'}/U_\infty^2$

(a)

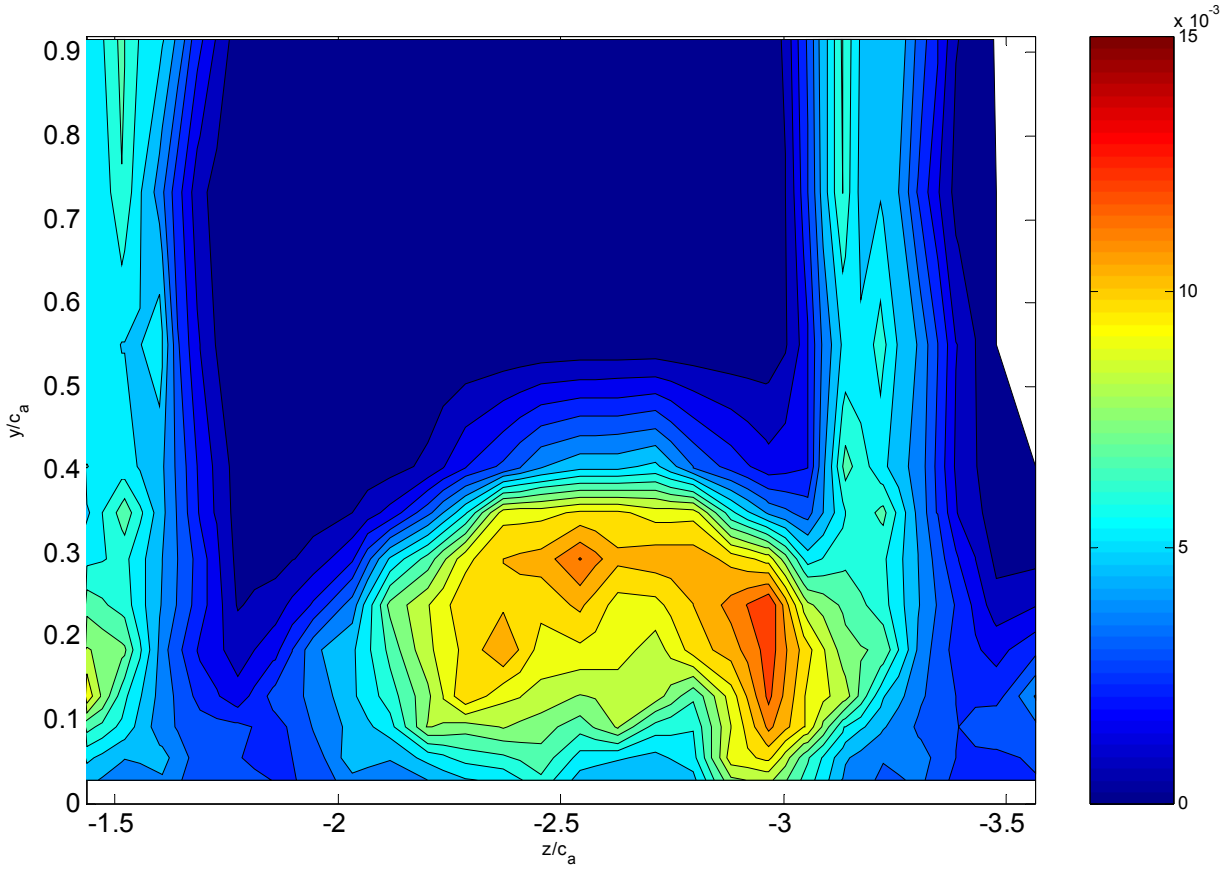

(b)

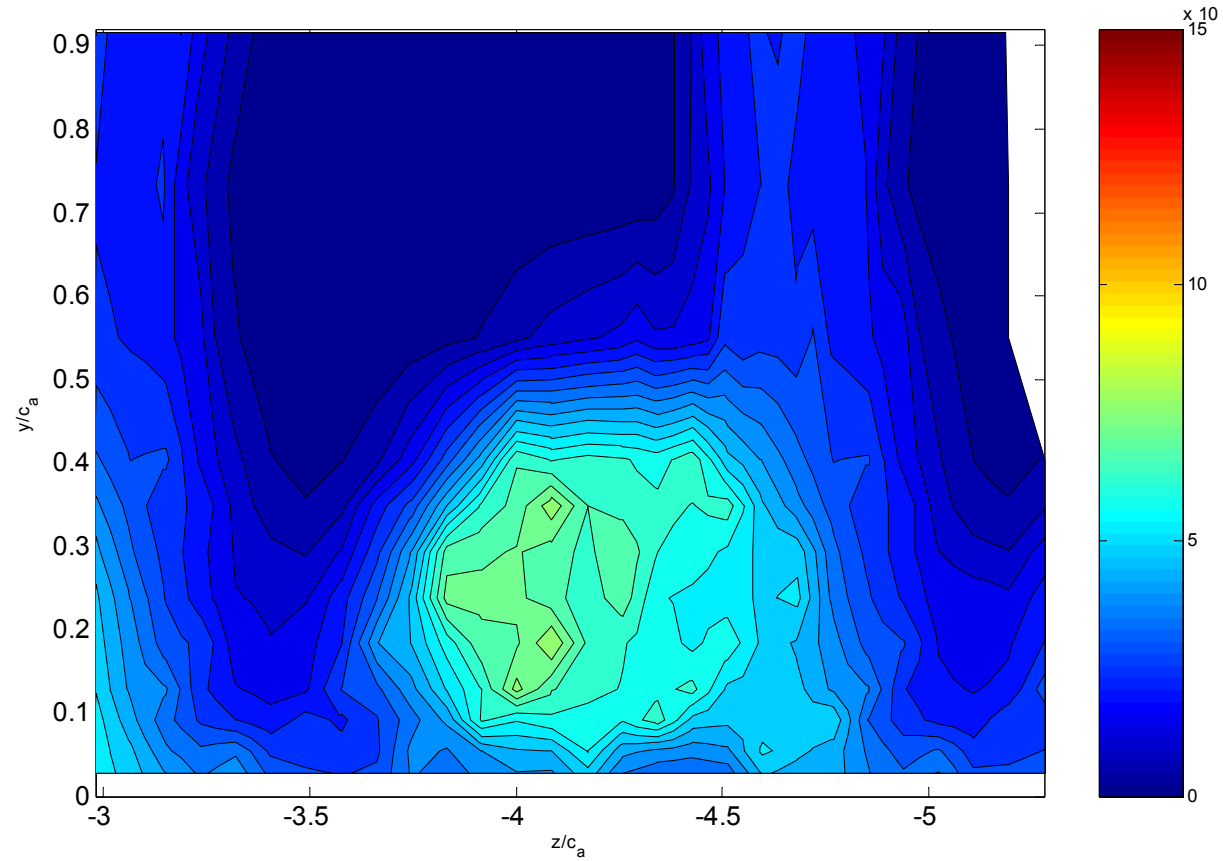

Figure 3-14: Turbulence kinetic energy cross-section, k/U_∞^2: ***(a)*** $x/c_a = 0.61$, ***(b)*** $x/c_a = 1.82$

(a)

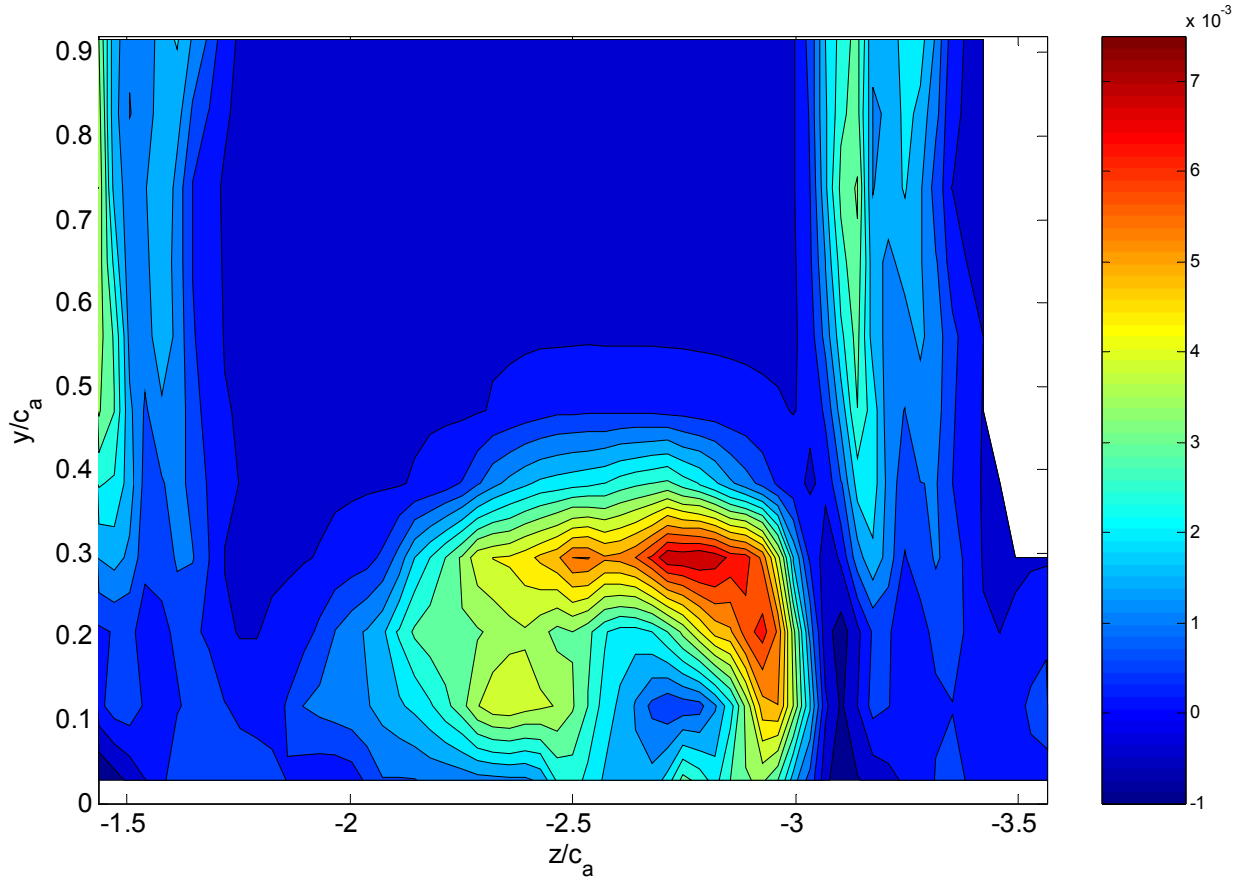

(b)

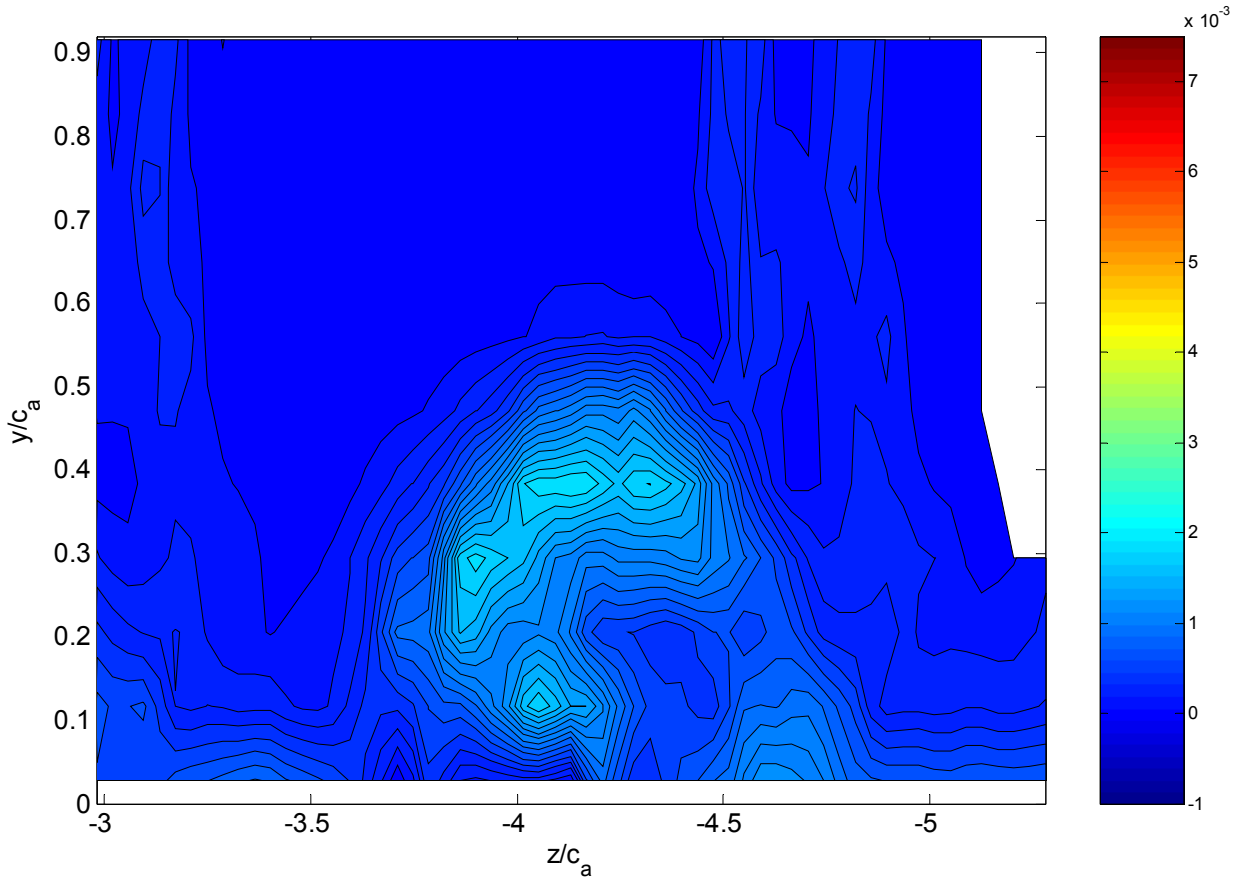

Figure 3-15: Turbulence kinetic energy production, $P_k c_a / U_\infty^3$: ***(a)*** $x/c_a = 0.61$, ***(b)*** $x/c_a = 1.82$.

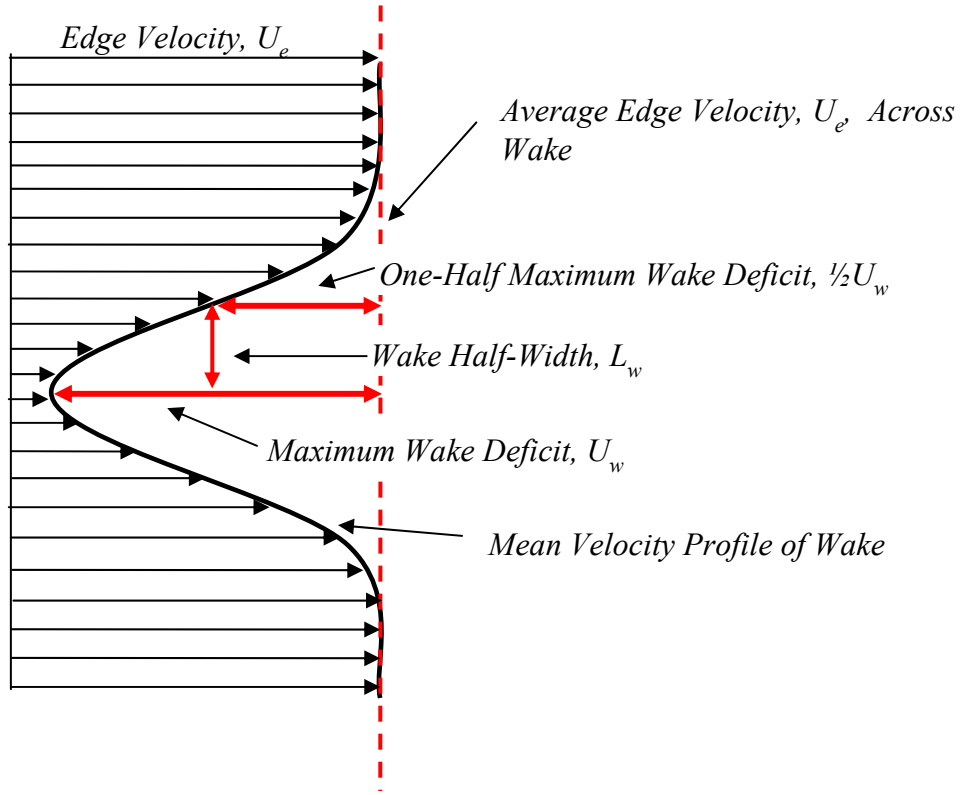

Figure 3-16: Definitions of wake characteristics

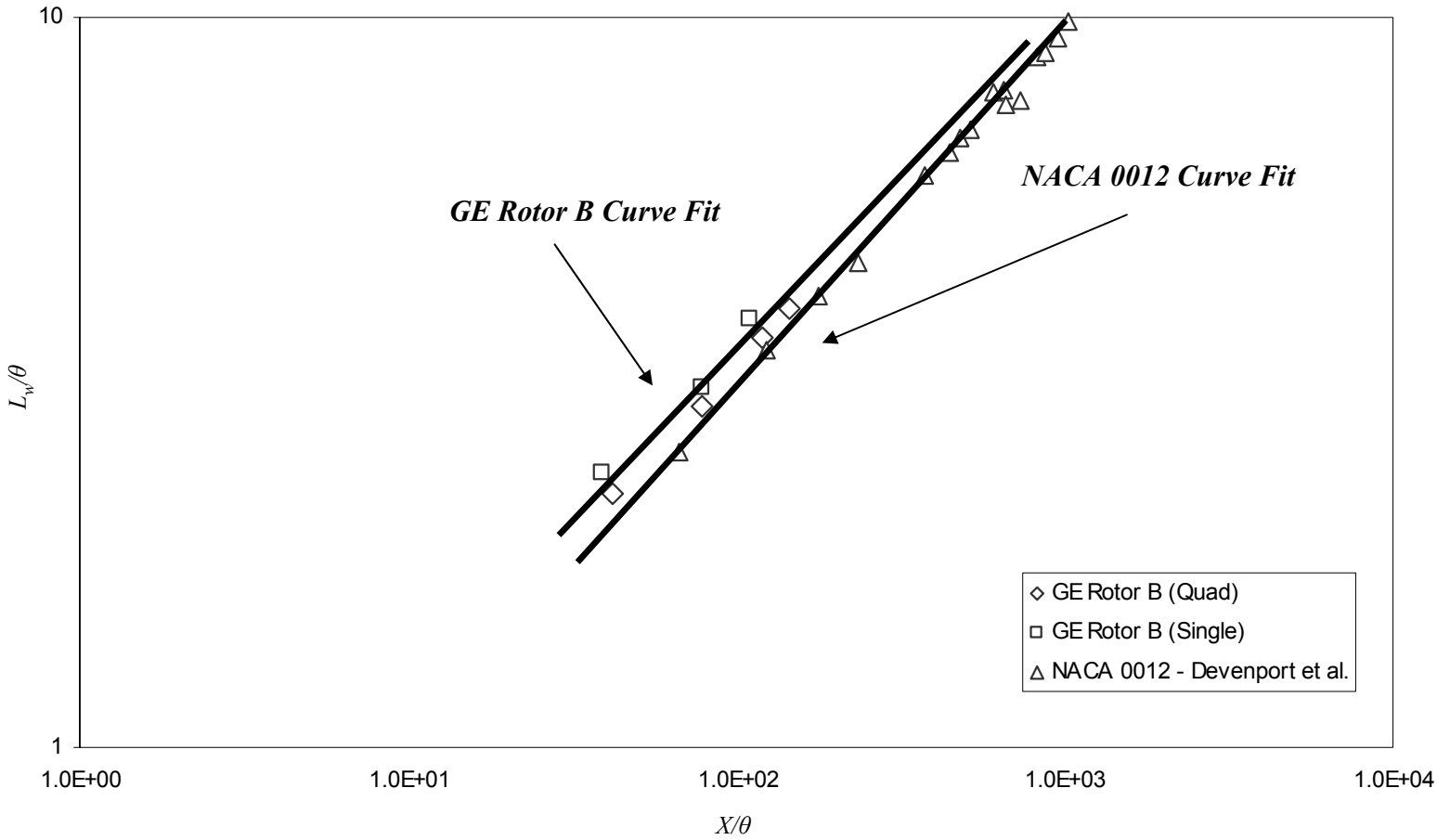

Figure 3-17: Normalized wake half-width of the wake, L_w/θ, as a function of normalized downstream distance, X/θ.

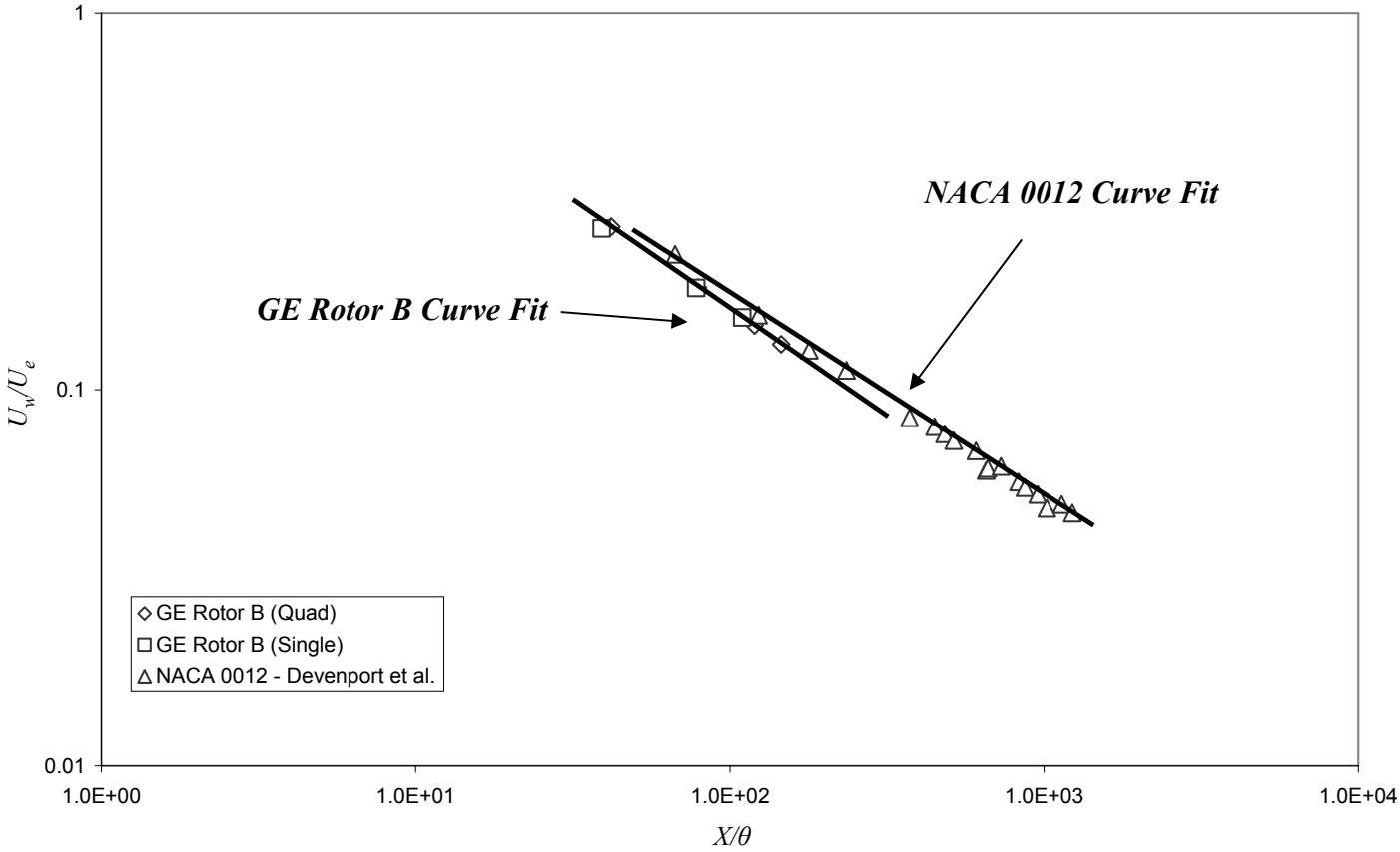

Figure 3-18: Normalized maximum velocity deficit in the wake, U_w/U_e, function of the normalized downstream distance, X/θ.

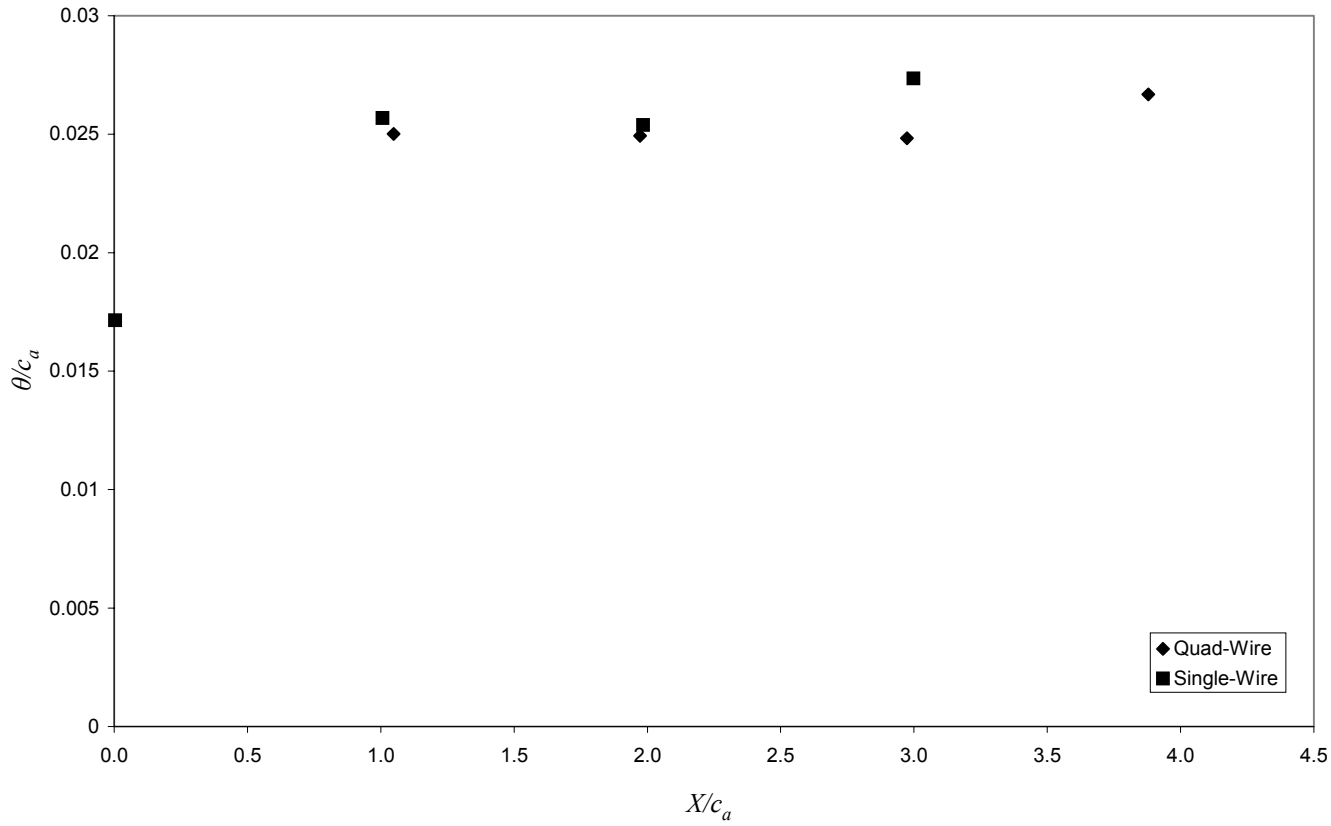

Figure 3-19: Normalized momentum thickness, θ/c_a, as a function of normalized distance downstream, X/c_a.

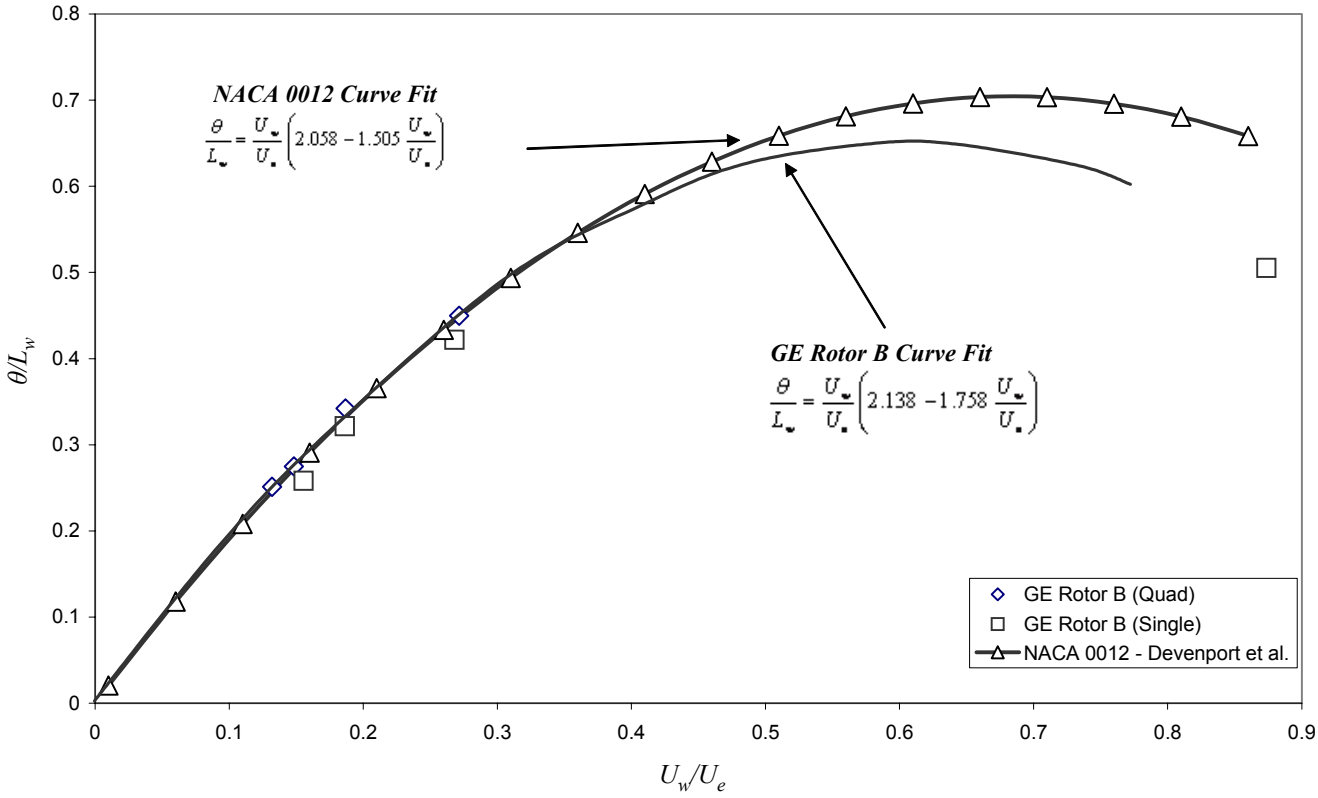

Figure 3-20: Normalized momentum thickness, θ/L_w as a function of normalized velocity deficit of wake, U_w/U_e.

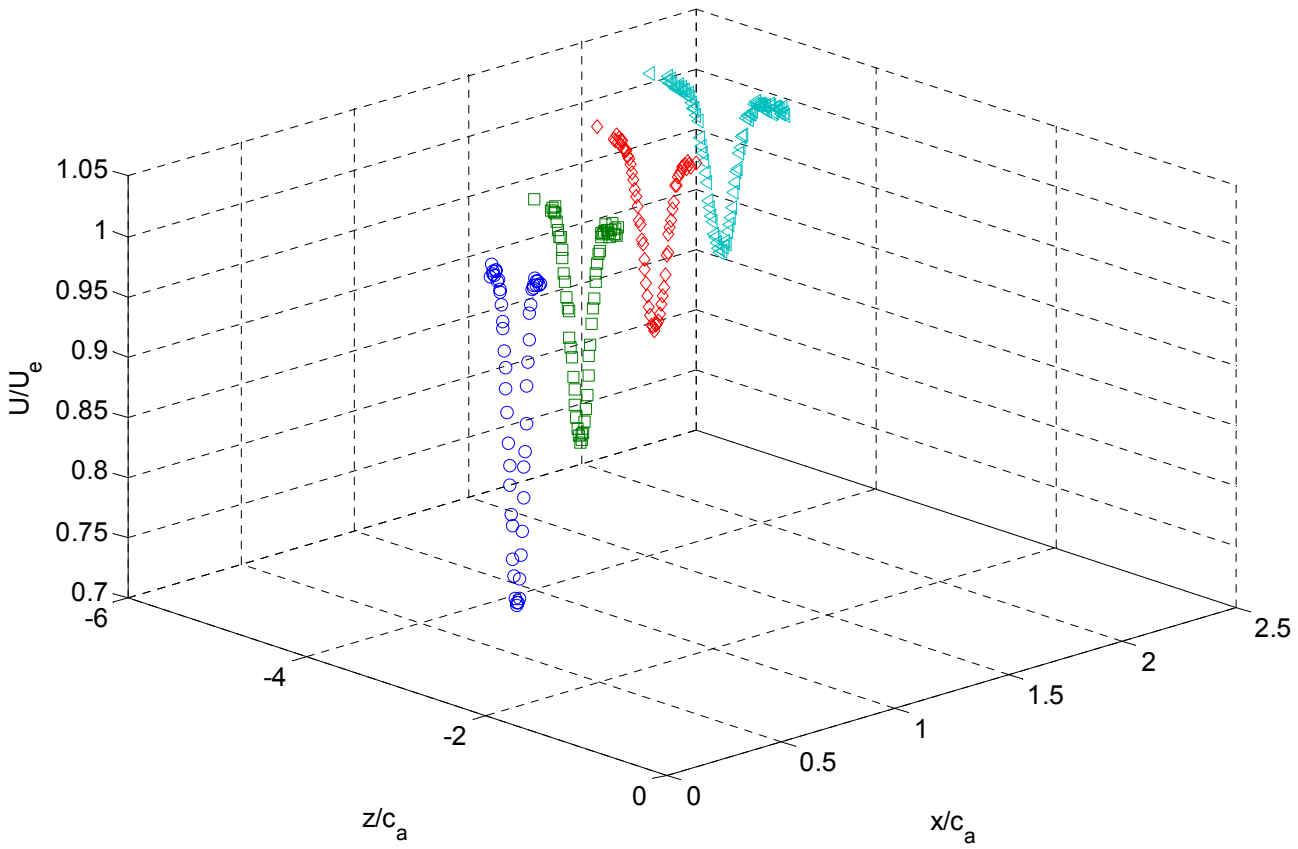

Figure 3-21: Streamwise mean velocity profiles, U/U_e, at the downstream locations of $x/c_a = 0.61$, 1.18, 1.82 and 2.38.

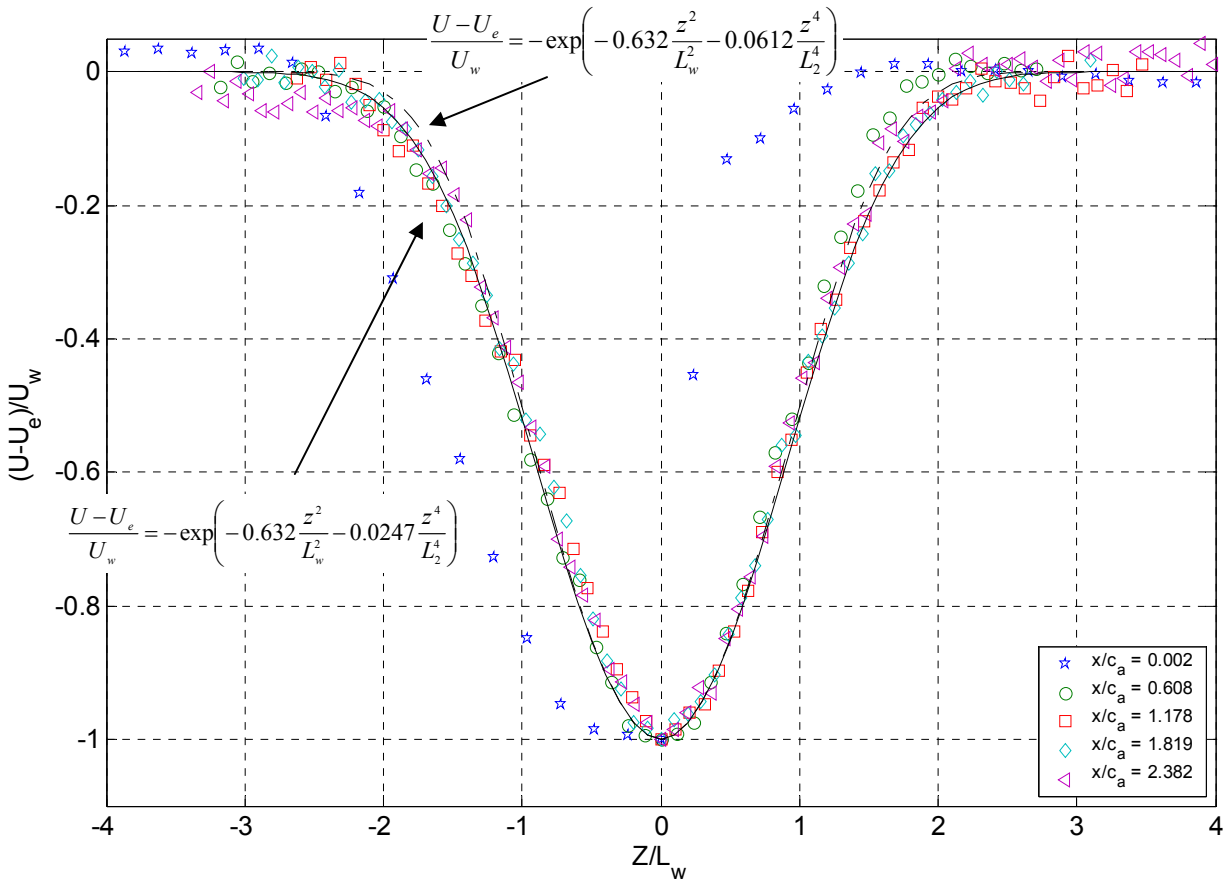

Figure 3-22: Streamwise mean velocity profile, $(U\text{-}U_e)/U_w$:

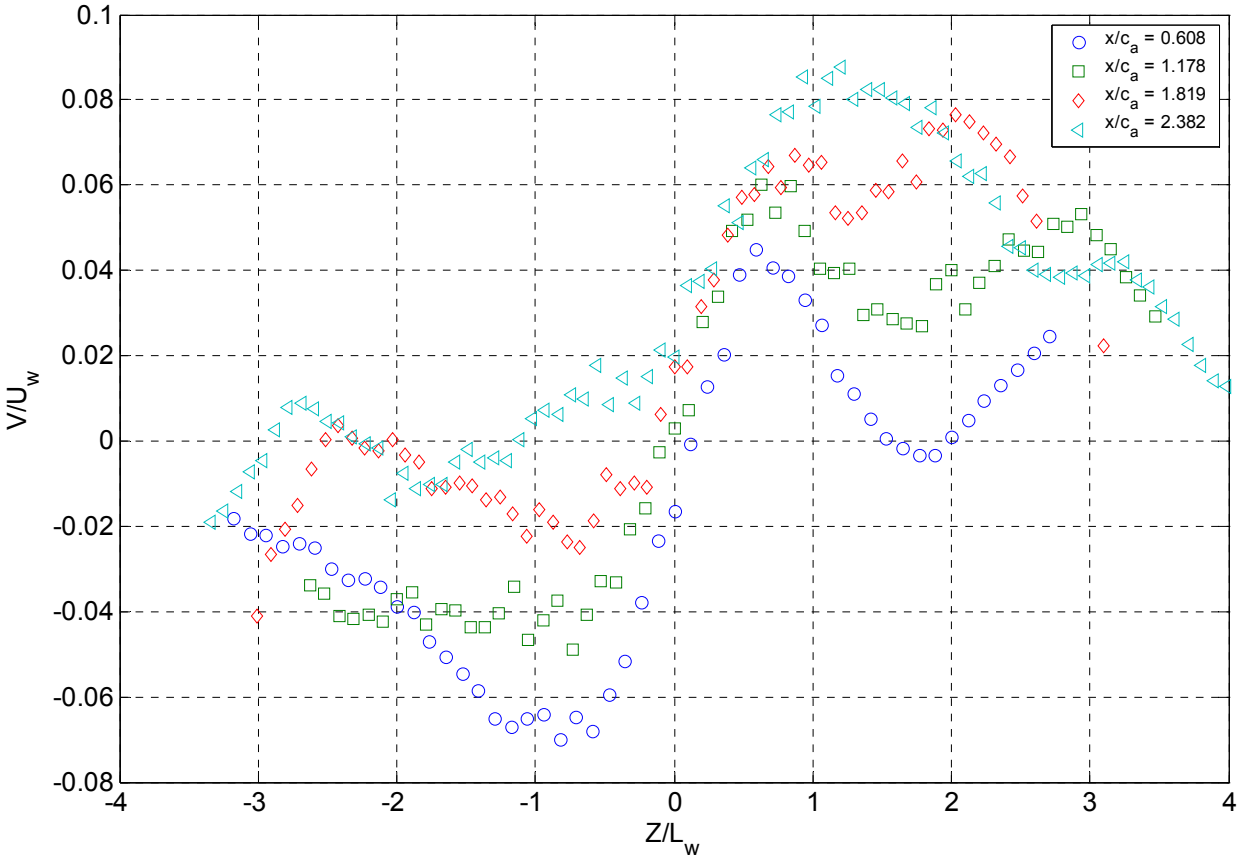

Figure 3-23: Spanwise mean velocity profile, $V/U_{w.}$

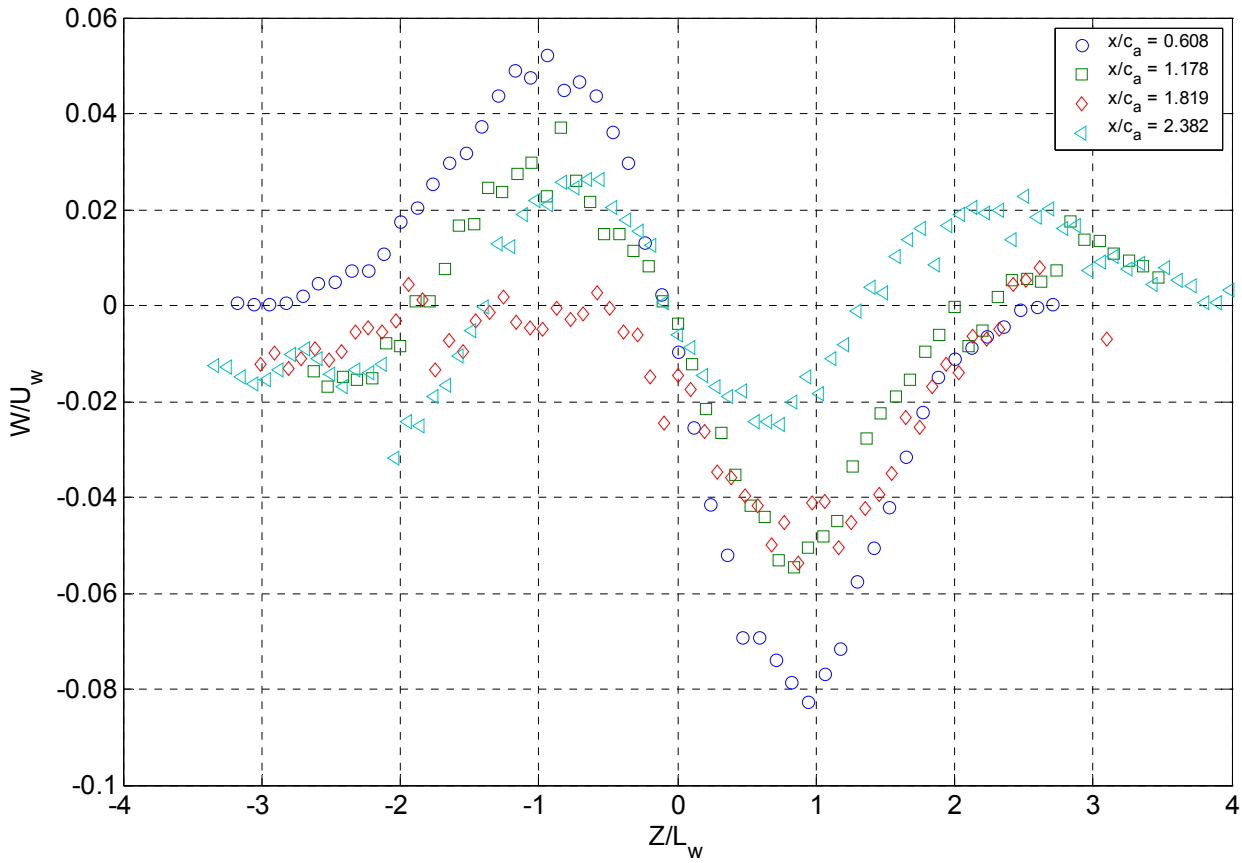

Figure 3-24: Cross wake mean velocity profile, $W/U_{w.}$

(a)

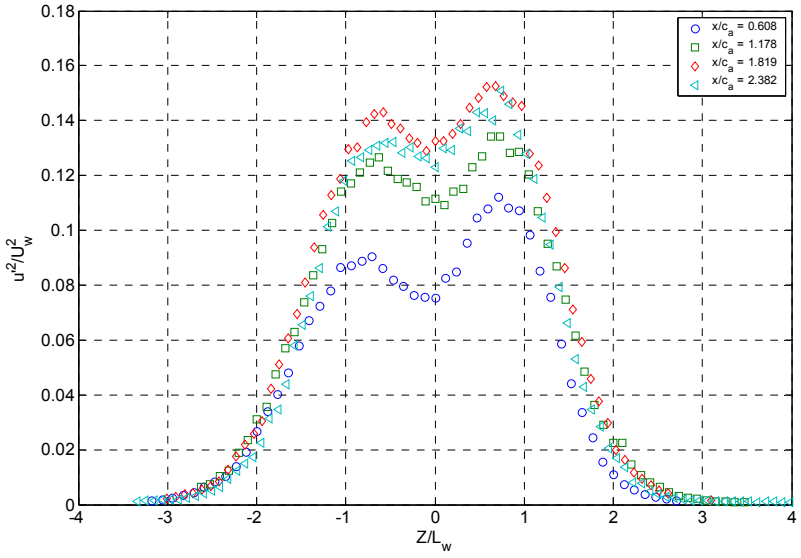

(b)

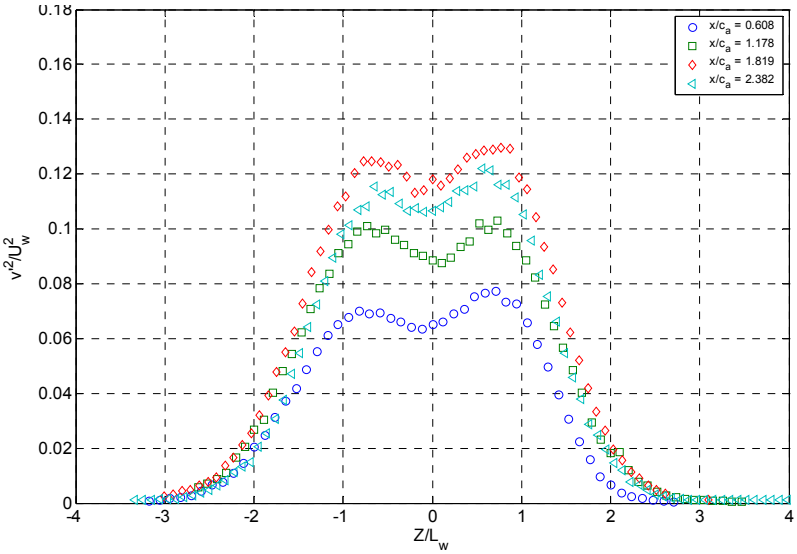

(c)

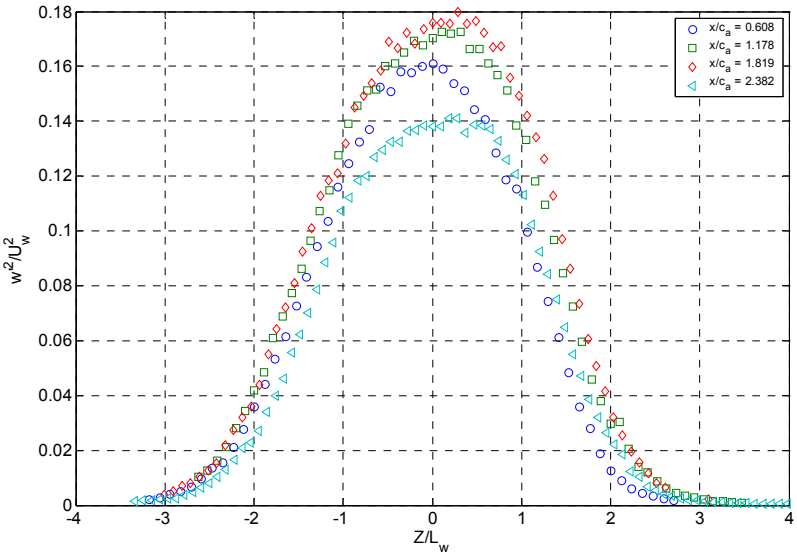

Figure 3-25: Reynolds stress profiles: ***(a)*** streamwise component, $\overline{u'^2/U_w^2}$, ***(b)*** spanwise component, $\overline{v'^2/U_w^2}$, ***(c)*** cross-wake component, $\overline{w'^2/U_w^2}$

(a)

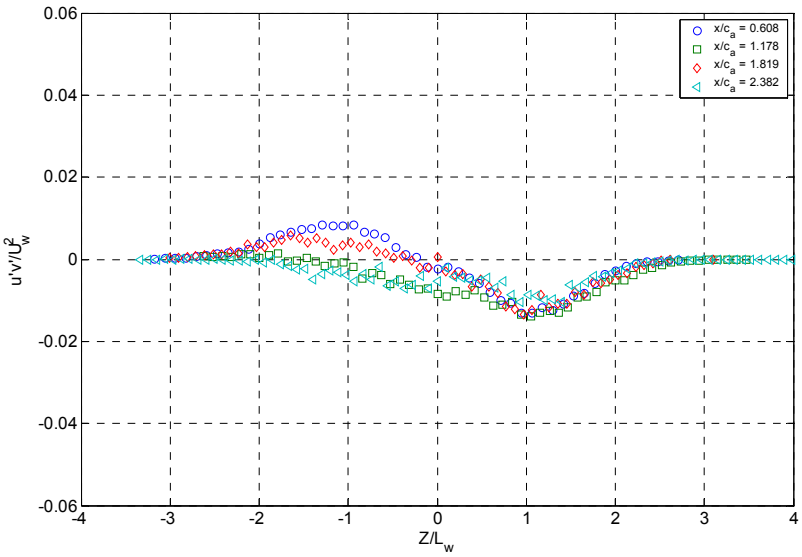

(b)

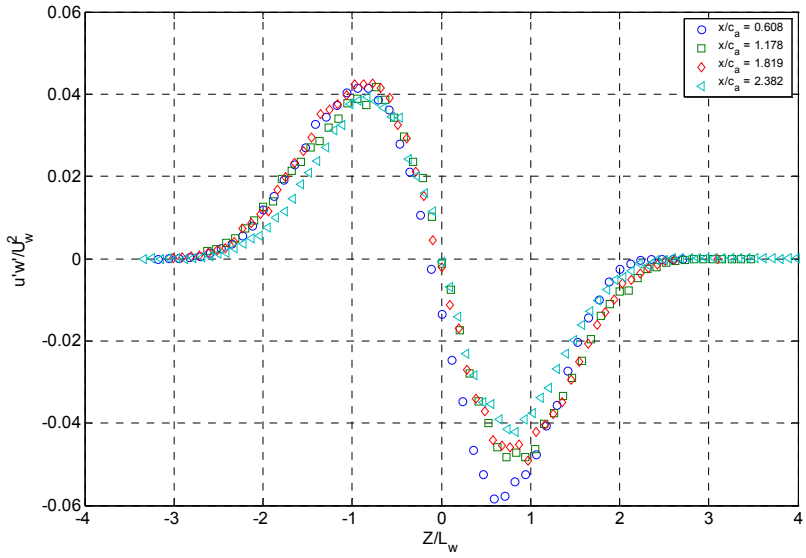

(c)

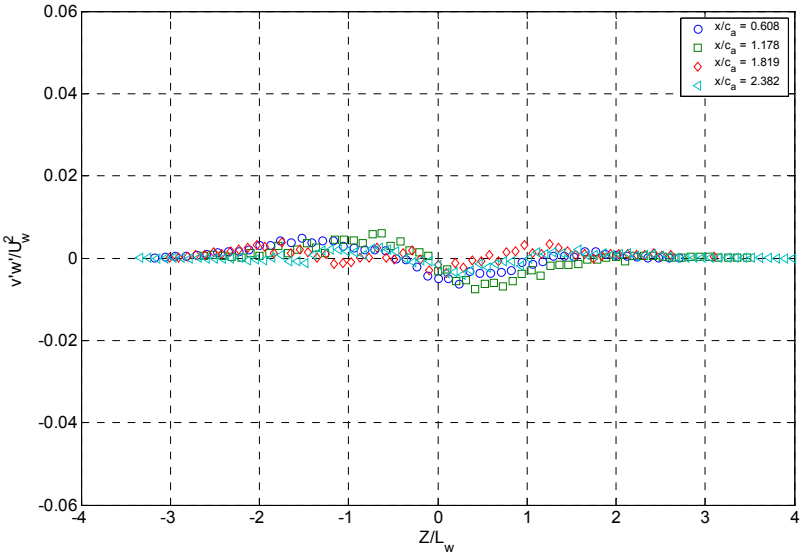

Figure 3-26: Shear Reynolds stress profiles: ***(a)*** $\overline{u'v'/U_w^2}$, ***(b)*** $\overline{u'w'/U_w^2}$, ***(c)*** $\overline{v'w'/U_w^2}$

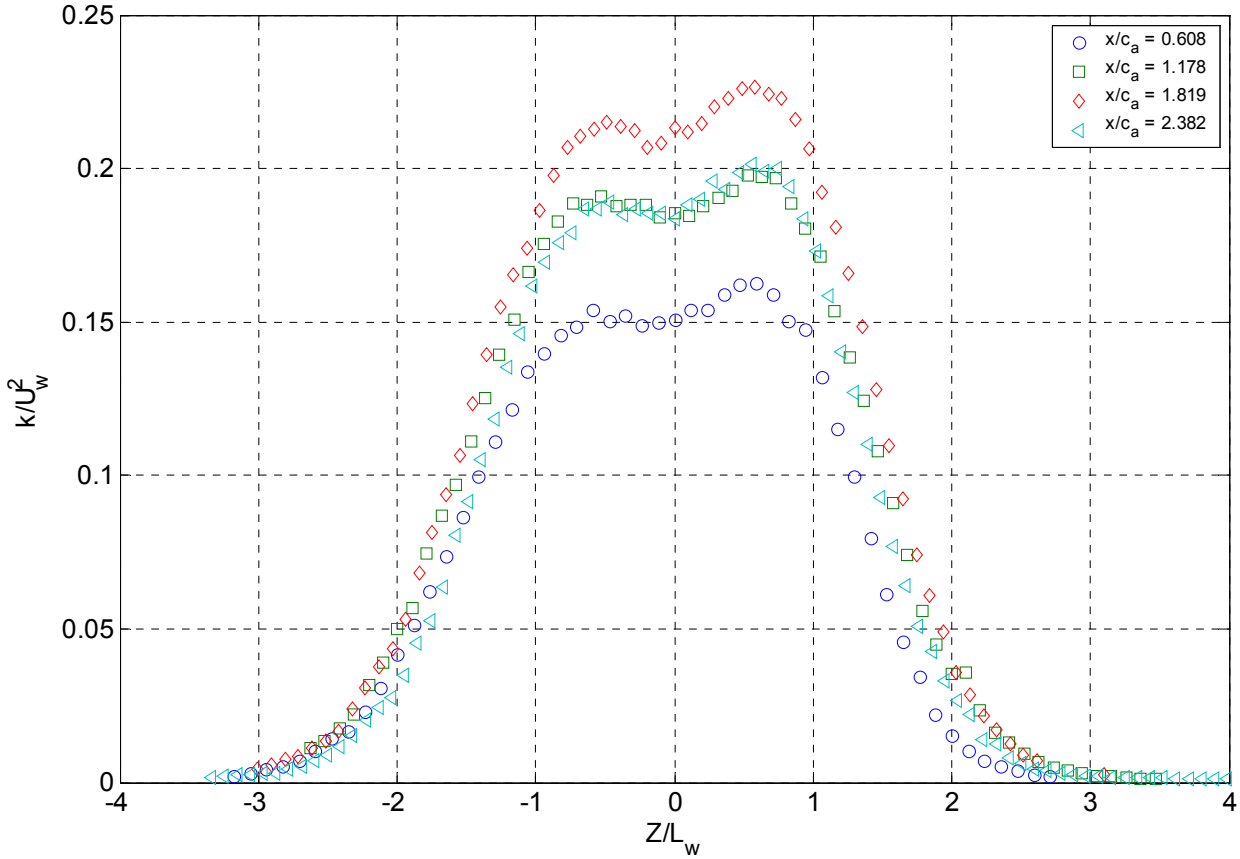

Figure 3-27: Turbulence kinetic energy profile, k/U_w^2.

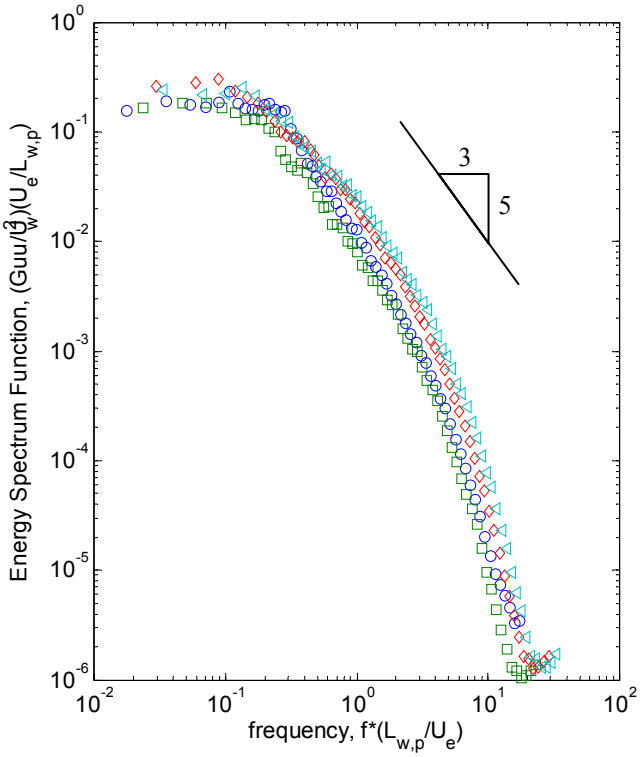

(a)

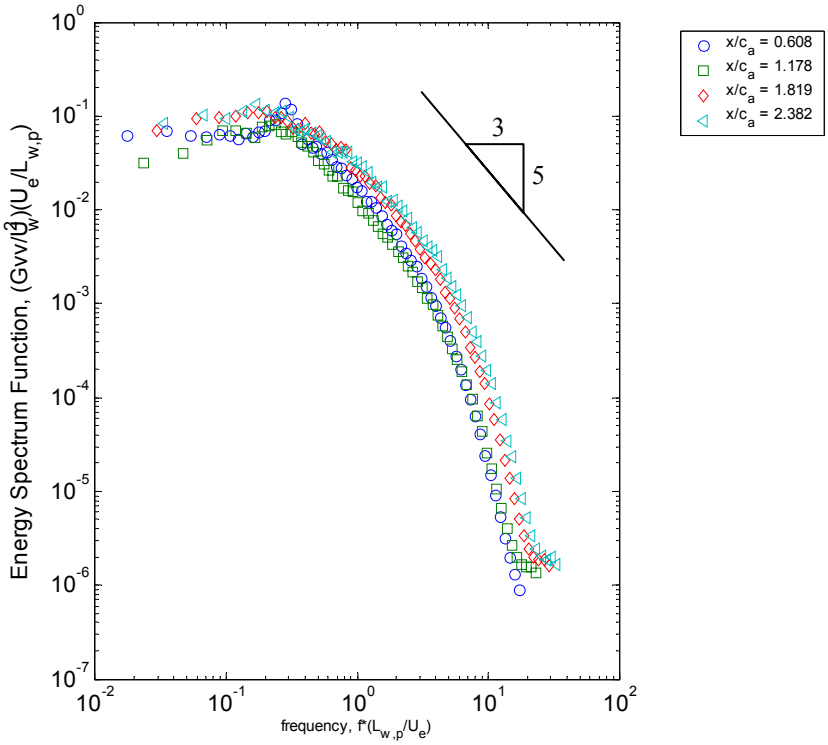

(b)

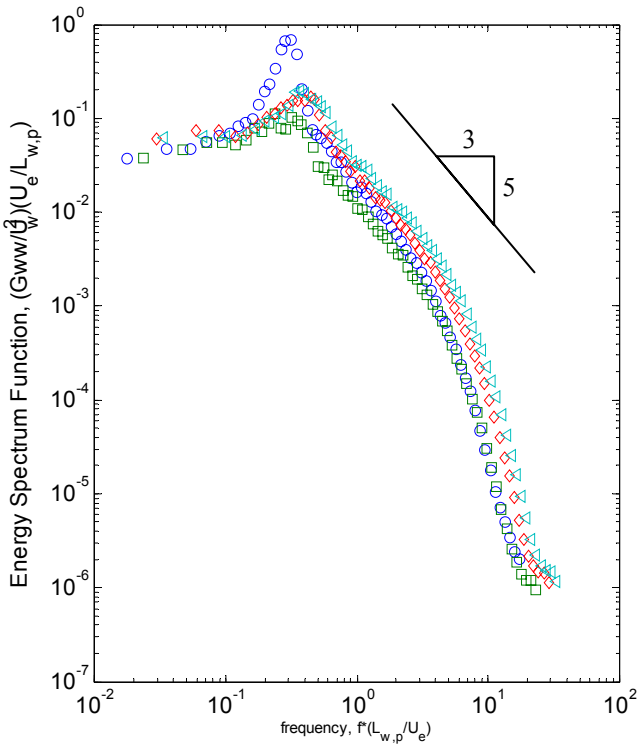

(c)

Figure 3-28: Spectral profiles at the wake center: ***(a)*** $(G_{uu}/U_w^2)(U_e/L_{w,p})$, ***(b)*** $(G_{vv}/U_w^2)(U_e/L_{w,p})$, ***(c)*** $(G_{ww}/U_w^2)(U_e/L_{w,p})$

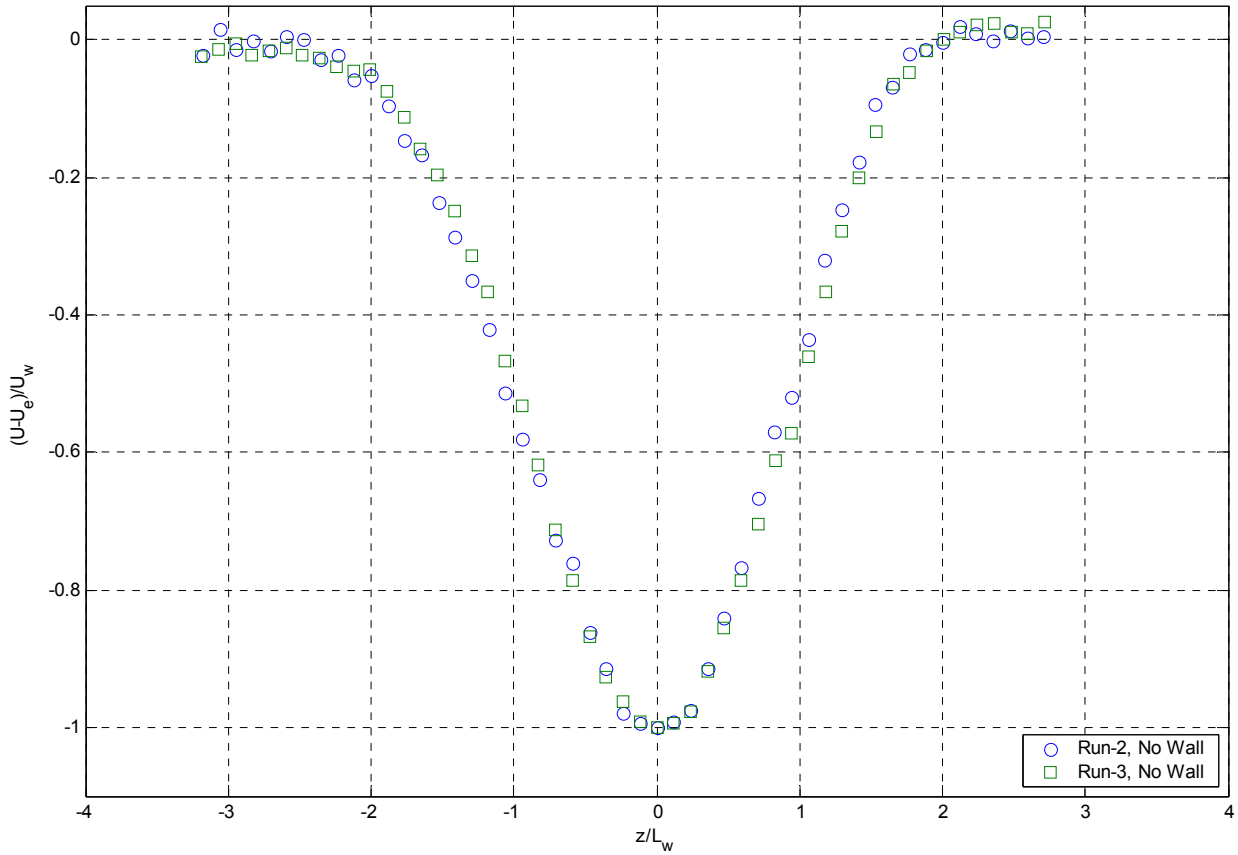

Figure 3-29: Mean velocity profile, $(U\text{-}U_e)/U_w$, comparing two runs performed at x/c_a = 0.61.

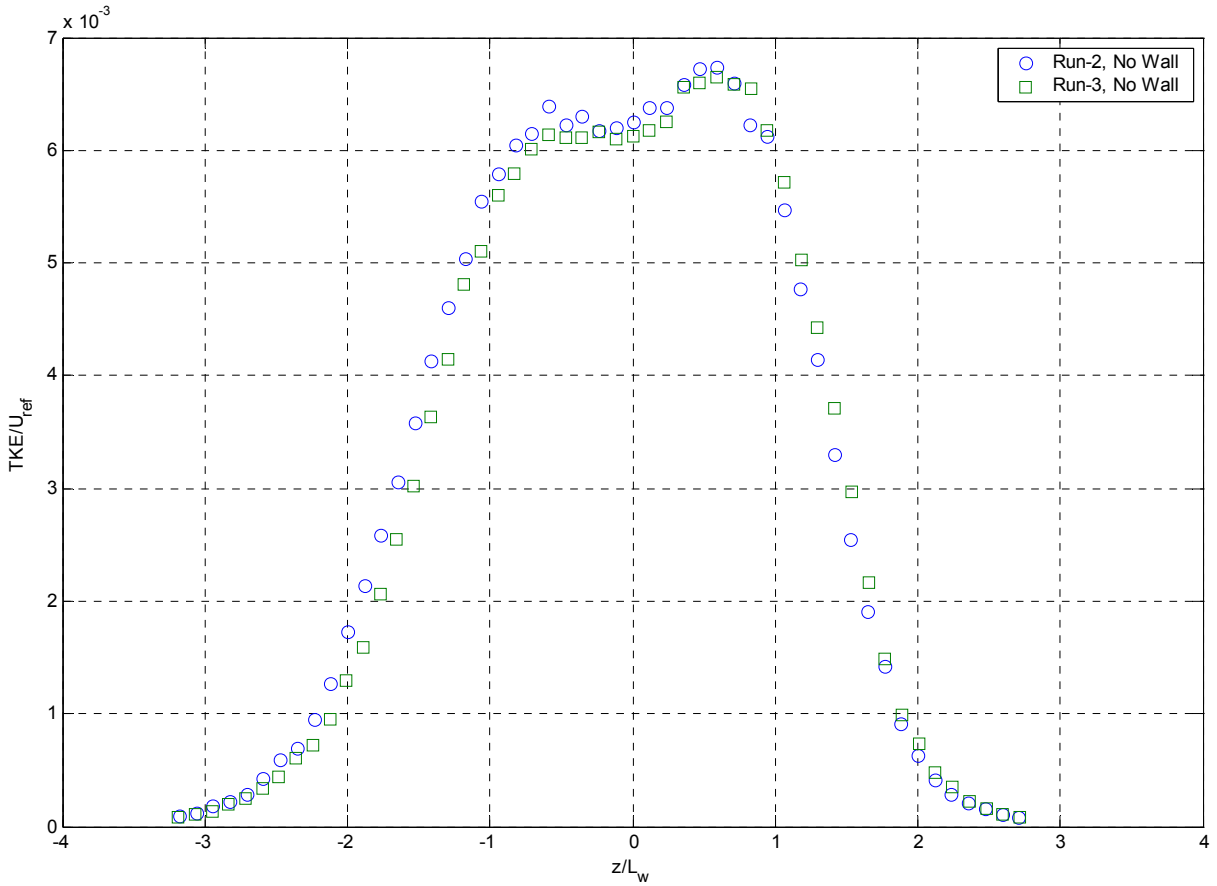

Figure 3-30: Turbulence kinetic energy profile, k/U_w^2, comparing two runs performed at x/c_a = 0.61